Understanding of tribomutation in ferritic/pearlitic steel

Dissertation
zur Erlangung des Grades
des Doktors der Ingenieurwissenschaften
der Naturwissenschaftlich-Technischen Fakultät
der Universität des Saarlandes

Mathias Peter Linz

Saarbrücken
2018

Tag des Kolloquiums:

29. November 2018

Berichterstatter:

Prof. Dr.-Ing. Frank Mücklich

Prof. Dipl.-Ing. Dr. Friedrich Franek

Akademischer Mitarbeiter:

Dr.-Ing. Frank Aubertin

Acknowledgement

The research work on the topic of this Thesis has been partly supported by the Austrian Research Promotion Agency within the COMET-K2 Project “XTribology” (Project-No. and 824187 and 849109 respectively).

Teile dieser Arbeit wurden zuvor in folgenden wissenschaftlichen Arbeiten veröffentlicht:

- Linz, M., Winkelmann, H., Hradil, K., Badisch, E., & Mücklich, F. (2013). Directional development of residual stress and surface fatigue during sliding contact. *Engineering Failure Analysis*, *35*, 678-685.

- Linz, M., Cihak-Bayr, U., Trausmuth, A., Scheriau, S., Künstner, D., & Badisch, E. (2015). EBSD study of early-damaging phenomena in wheel–rail model test. *Wear*, *342*, 13-21.

- Linz, M., Ripoll, M. R., Gachot, C., Pauly, C., Franek, F., & Mücklich, F. (2017). On the competition between plastic deformation and material detachment in ferritic/pearlitic steel under boundary lubrication. *Wear*, *376*, 813-821.

- Linz, M., Rodríguez Ripoll, M., Pauly, C., Bernardi, J., Steiger‐Thirsfeld, A., Franek, F., ... & Gachot, C. (2018). Heterogeneous Strain Distribution and Saturation of Geometrically Necessary Dislocations in a Ferritic–Pearlitic Steel during Lubricated Sliding. *Advanced Engineering Materials*.
  Kurzfassung

Kurzfassung

Durch die unterschiedlichen mechanischen Eigenschaften von ferritischen/pearlitischen Stählen kommt es bei tribologischer Beanspruchung zu komplexen Verformungsvorgängen an der Oberfläche. Um diese verstehen zu können, werden in dieser Arbeit die Ergebnisse unterschiedlicher Analyseverfahren kombiniert. Speziell durch die Kombination von der Phaseninformation aus lichtmikroskopischen Aufnahmen mit der Darstellung der plastischen Verformung mittels Elektronenrückstreubeugung (EBSD) konnte der Anteil der Phasen an der Verformung qualitativ verglichen werden. Die Ergebnisse konnten durch Berechnungen von Spannungs-Dehnungs-Diagrammen der einzelnen Phasen bestätigt werden.
Zudem wurde der Einfluss tribologischer Parameter auf die plastische Verformung untersucht. Dabei konnten unterschiedliche Verschleißverhalten beispielsweise bei unterschiedlichen Viskositäten der Schmierstoffe erklärt werden.
Durch die Analyse der Eigenspannungen bei Schwing-Reib-Versuchen konnte die Richtung des Risswachstums, parallel zur Bewegungsrichtung, durch transversale Zugspannungen erklärt werden.
Abschließend wurden die gewonnenen Erfahrungen genutzt um die Frühschädigung von Schienenwerkstoffen im Rad-Schiene-Kontakt zu untersuchen. Dabei wurden zwei unterschiedliche Verhalten bei einem ferritischen/perlitischen Stahl und einem rein perlitischen Stahl gefunden. Darauf basierend wurde ein Model der Frühschädigung für diese beiden Werkstoffe entwickelt.

Abstract

Ferritic/pearlitic steels show a complex response to tribological stressing due to their different mechanical properties. In this work, different analysis methods are combined in order to achieve a better understanding of such processes. Especially the phase-information by optical microscopy combined with the strain information by electron backscatter diffraction (EBSD) enabled for a qualitative comparison of the plastic response of the two phases. The results are confirmed by calculated stress-strain curves of the phases.
Additionally, the influence of tribological parameters was investigated regarding their impact on strain formation. This allows to understand the correlation of lubricant viscosity, strain formation and wear mechanisms.
Moreover, the crack initiation in oscillation tests was correlated with tensile stresses perpendicular to the direction of movement measured by x-ray diffraction.
Early-damage phenomena in rail materials subjected to wheel-rail-contact were analyzed using the gained experiences. Two different strain responses where found for ferritic/pearlitic and pearlitic steels. Based on these findings, a model was developed explaining the early-damaging mechanisms of the two steels.

Contents

Chapter 1

Introduction

Our daily life comprises manifold tribological phenomena, in which two or more moving surfaces are involved. Prominent examples are the tire/road contact of vehicles, gearboxes in machinery or electrical contacts in cars potentially being subjected to fretting. All these tribological systems may appear simple at a glance but they get more complex at a closer look in particular studying the rubbing interfaces with high-resolution analytical tools. Thus, the attempt to understand the lifetime of contacting materials actually turned from a daily life problem into tribology research.

However, damaging effects in the field of tribology have a huge scope of influencing parameters which several branches of science claim as their field of science. Regarding materials science the focus lies on the changes of the surface as well as on the subsurface material. Thereby, introduced stain and the further development of it to form (sub)surface damages are one mayor factor. Additionally, with the wide range of tribological applications the range of materials used to render these applications possible also extends. As all scientific investigations, the knowledge about a tribological problem can only be as good as the method used. Whereas a smart combination of different methods allows to gain information about the damaging mechanisms in different length scales. Additionally, very specific information such as e.g. imaging by scanning electron microscope (SEM) might be correlated by the residual stresses by XRD. Thus, the XRD data might help to understand the results seen by SEM. In addition, TEM can additionally show effects in length scale of dislocations and thus provide a deeper insight into the strain formation.

Sub-surface plastic deformation and defect accumulation in sliding contacts is governed by dislocation activity, crack initiation as well as propagation, and is related to material wear (Rigney et al., 1986; Rigney/Divakar/Kuo, 1992; Rigney, 1998). The strain evolution depends on the applied contact stresses, which are determined by the geometrical and mechanical properties of the contacting bodies (e.g. Young's modulus, Poisson's ratio and yield strength) and the contact characteristics (e.g. sliding speed, lubrication regime). As soon as contact stresses in the sub-surface zone locally exceed the yield strength of the material, plastic deformation will occur (Moshkovich et al., 2010). The resulting localized

sub-surface plastic strains have been reported to build up a thin surface layer with a thickness in the micrometer range, characterized by the presence of nanocrystalline grains with increased hardness compared to the underlying bulk material (Walzhofer et al., 2014). Upon increasing the number of sliding cycles, crack initiation and growth take place, accelerating material damage, followed by analogous mechanisms as those reported for the shakedown theorems of bulk materials (Williams, 2005a). A characteristic of tribological contacts is that damage accumulation in the sub-surface zones usually appears in the form of surface delamination (Korres/Feser/Dienwiebel, 2012). Sub-surface plastic deformation has been widely investigated under dry contact conditions, especially for copper and its alloys (Tarasov/Lychagin/Chumaevskii, 2013) (Meshi et al., 2011). Recently, those materials have also been studied under lubricated conditions (Moshkovich et al., 2010; Moshkovich et al., 2011). In all cases, a thin layer of grain refined/lamellar shaped material is observed, characterized by high hardness, similar to those observed in severe plastically deformed (SPD) bulk copper (Moshkovich et al., 2010; Tarasov/Lychagin/Chumaevskii, 2013). SPD microstructures created by sliding friction can undergo significant grain refinement with average grain sizes down to a few nanometers with a correlated increase of the yield strength, as recently shown for copper (Wang et al., 2003b). The results reported in literature so far are mostly concerned with single phase materials. The number of studies devoted to the analysis of sub-surface strain development on multi-phase materials is rather uncommon, despite their enormous impact for engineering applications. Mahato et al. (Mahato et al., 2011) studied the strain formation by sliding friction in an as-cast near eutectic aluminum-silicon alloy. They observed regions of mild wear with silicon matrix decohesion and grain refinement in the vicinity of the silicon particles. In the severe wear zone, grain refinement was more pronounced and accompanied by micro cracks and fragmentation of silicon particles. Mingard et al. (Mingard/Gee, 2007; Gee/ Mingard/Roebuck, 2009) studied surface strain development of wear tracks in hard metal (tungsten carbide in cobalt matrix). The work focuses on strain development inside both phases with an emphasis on strain distribution within the matrix using misorientation and pattern quality determined by electron backscatter diffraction microscopy (EBSD).

Ferrite-pearlite steels, used in a wide range of applications, are under investigation since the 18th century (Allain/Bouaziz, 2008). Among these applications, ferrite-pearlite steels are also used for tribologically stressed construction-parts such as rails or oil rigs. Nevertheless, the tribological response of such systems is not well understood yet. Especially, the presence of the two crystallographic phases with different mechanical properties makes it even more complex. Since the yield strength of one phase is reached before the other, one phase will yield earlier than the other. However, the weaker phase will not strain in the same way as if it would be a single phase material. Due to the presence of the second phase, the mechanical incompatibility will also influence the amount of strain introduced to the material. Moreover, The evolution and deviation of strain in the

material influences the initiation and propagation of cracks. Therefore, a detailed information about the strain evolution is crucial for the understanding of damaging effects in tribological contacts such as e.g. railway materials.

Wear and rolling contact fatigue (RCF) in wheel-rail contact is a main topic in scientific as well as economic studies related to improve the lifetime of rails. The requirements on the rail material are growing with increasing train speeds and higher axle loads. In order to screen different rail materials, various test methods can be found in literature. Apart from the costly track tests there are test rigs providing real-size wheels as well as classic laboratory triobological test-rigs. Especially investigations related to the wear of rails (Pombo et al., 2010; Pombo et al., 2011) can be performed by classic tribological test-rigs. For instance, Tyfour et al. (Tyfour/Beynon/Kapoor, 1995) studied rolling contact wear by rolling two discs made of the rail and the wheel material against each other. Besides wear, rolling contact fatigue (RCF) is a growing damage phenomenon (Zerbst/Mädler/Hintze, 2005). The RCF is influenced by various conditions of the rail as for instance grain sizes, hardness and stored internal strains (Zerbst/Mädler/Hintze, 2005; Beynon/Garnham/Sawley, 1996; Stock/Pippan, 2011; Lee/Polycarpou, 2005; Robles Hernández et al., 2007; Donzella et al., 2005).

In addition to the deviation of strain in the material, the resulting residual stresses are also of importance as they also directly influence the direction of crack initiation. Considering crack failure, one might also take into account the accumulation of cracks and the resulting breaking out of surface material. Thus, the crack formation can also cause wear. As mentioned before, the subsurface damages in tribological systems depend on a multitude of parameters. Each of them having a specific influence on the material response. Especially, the normal load and the lubrication conditions play an important role on the wear of the surface material. While the normal load mostly influences the magnitude of subsurface stresses, the lubrication can also change the deviation of the stresses inside the material.

Today's analysis methods allow further insights into the effects of material changes due to external stresses. Thus, more and more bricks of the whole picture of the material mutation due to tribological stresses can be uncovered. This work will strive to answer the following questions regarding tribomutation, especially by using synergetic effects by combining different analysis methods.:

- How does the strain in the material evolve with increasing numbers of cycles, especially for the case of low material loss due to wear?
- How do the to phases of the ferrite-pearlite steel participate on the strain evolution?
- How will the inhomogeneous material properties between two phases influence each other?

- What is the difference between tribological contacts lubricated with higher as well as low viscosity oil concerning the strain evolution? Furthermore, can the macroscopic wear effects be correlated and be explained by the strain evolution?
- Bidirectional sliding contacts are known to show different wear mechanisms than unidirectional sliding contacts. How can the wear effects in bidirectional sliding be explained?
- Can the methods be applied to an actual application? Such as: how does the microstructure influence the strain evolution of a railway track and how does it influence its wear during operation?

In this work, mainly EBSD will be used and depending on the information needed, the EBSD results will be combined by XRD, TEM as well as optical microscopy. TEM as a high-resolution analytical tool is used for investigating the strain related effects such as dislocation pile-ups of specific regions, which were previously selected by EBSD measurements of the same region. Even though lacking in terms of resolution, light optical microscopy is still one of the preferred methods for a proper distinction between ferritic and pearlitic regions. Thus, combining the phase information by light optical microscopy with the local strain information by EBSD, it is possible to distinguish the strain evolution for both phases.

Chapter 2

Theory and state of the art

This chapter offers a brief introduction into the used methods. Most of the well established and frequently applied methods will not be discussed in detail here but EBSD should be presented also from the theoretical side as this technique served as "workhorse" within this thesis. In addition, a deeper scientific background will be given especially related to tribology, the influence of material properties on friction and wear and finally the correlation between plastic deformation, strain formation as well as fatigue.

2.1 Tribology

Ever since the first time humans used tools, tribological properties were always of importance for improving or just extending the lifetime of parts used in a wide range of applications. In the 15th century Leonardo da Vinci already studied the relation between normal force, contact area and friction (Palaci, 2007). In 1699 Guillaume Amontons announced the two relations, nowadays known as the Amontons' laws (Gao et al., 2004):

1. the frictional force is proportional to the normal force
2. the friction coefficient is independent of the nominal contact area

Furthermore, Charles Augustin de Coulomb added two further frictional laws (Popov, 2009):

1. for a given set of contacting materials, there is a maximum for the static friction
2. the static friction coefficient exceeds the sliding friction coefficient

In 1966 Peter Jost published a report emphasizing the cost of wear, friction and corrosion to the economy thereby establishing tribology as the related term (Jost, 1966). The report drew the attention to this new field of research. Later, tribology became a separate area of research in the year 1968 due to definition by the OECD as

"the progressive loss of material from the operating surface of a body occurring as a result of relative motion at its surface" (Lansdown/L, 1986)

The quotation keeps the option open, that the contacting medium is not mandatory an other solid body. Since friction caused by fluids or gases can also cause friction. Typically, wear is understood as a mechanical effect but additionally, chemical aspects are also of importance (e.g. corrosion). Furthermore, wear usually is first related to abrasive loss of material. But adhesion and surface fatigue can also cause a loss of material. In the case of surface fatigue, cracks occur at stress intensities at or close to the surface growing into the material or to the surface and thus detaching debris from the body (pitting) (Czichos/Habig, 2003). Cyclic stresses can also lead to a lamellae like deformation and debris formation (ratchetting) (Johnson, 1995). Adhesive wear is likely to occur when the contacting bodies are of the same sort of material or at high sliding speeds (galling) (Tallian, 1972). Even in lubricated contacts, adhesive wear might occur when the lubrication film is broken and the bodies come in direct contact (scuffing) (Williams, 2005b). Repeated contacting loads may also create subsurface stresses. After an initial plastic deformation the introduced stresses can be reduced due to the increased contact area, thus deforming the material only elastically (Williams/Dyson/Kapoor, 2005; Williams, 2005a). The friction coefficient also depends on the reactivity of the two materials in contact. More reactive material in contact may lead to a higher coefficient of friction and a rougher wear scar (Miyoshi/Buckley, 1979).

Based on the work of Heinrich Hertz, in which he described the situation of two contacting bodies in contact (Hertz, 1881), the importance of introduced stresses became more and more important for a fundamental understanding of contact situations. For example, even the theory of Hertz is just valid for perfect rigid bodies and without plastic deformation.

Investigating tribological contacts, the materials of the bodies in contact are usually first to be considered. The elastic and plastic behaviour is essential for the development of stresses in the contact zone. The deformation (elastic and plastic) leads to an increased area of contact and thus, a lower contact pressure. Furthermore, stiff materials with a higher Young's modulus have a behaviour, closer to the predicted theory by Hertz.

Talking about the materials of the bodies, you also have to consider the medium in-between the bodies. Lubricants not only lower the friction between the bodies: adhesives in the lubricant can have chemical characteristics on the surfaces or provide crack closure (Kumar/Curtin, 2007). Also the transfer of the stresses is influenced by the thickness of the lubricant layer. If the pressure in the lubricant (e.g. oil) is high enough to carry the load, both surfaces are separated by a layer of lubricant (hydrodynamic contact). Thus, the thickness of the lubrication layer has to be thicker than the sum of roughnesses of both bodies.

Even if the contact is performed in air on clean surfaces, it might show a different

behaviour under high vacuum conditions, since the contents of the gas can also influence the chemical and physical behaviour of the materials or present lubrication (e.g. oxidation of the wear track). Another important factor related to the area of contact is the shape of the two contacting bodies. In technical applications, several body geometries are used and combined in tribological contacts with each combination having its own contact behaviour regarding the stresses in the materials e.g. ring on ring or ball on ring. But not only the macroscopic geometry has an influence on the material behaviour. The roughness influences the contact behaviour on the microstructural level. In this context, smooth surfaces are not always an advantage. The valleys between the peaks caused by the roughness might work as reservoirs for lubricants thus resulting in lower friction during the lifetime of a machine element for example. Furthermore, the ratio between the roughness of the two bodies is of importance. For a lower roughness (<5 nm for solids) and especially for materials of the same chemistry (e.g. two steel bodies) adhesion forces between the surfaces are also not negligible anymore (Czichos/Habig, 2003). Even roughness can cause an interlocking between the bodies and thus a higher friction. Mainly two roughness values are used to describe technical surfaces (Stachowiak/Batchelor, 2013; Czichos/Habig, 2003):

$$R_a = \frac{1}{n}\sum_{i=1}^{n}|y_i| \tag{2.1}$$

$$R_q = \sqrt{\frac{1}{n}\sum_{i=1}^{n}y_i^2} \tag{2.2}$$

Apart from a macroscopic view on materials and their influence on the frictional response, it is decisive to shed more light onto the surfaces in direct contact, interfaces or evolving tribochemical reaction layers. According to that, different layers are typical for technical contact situations:

- internal (gradient) layers caused by microstructural changes at the surface
- functional coatings
- contamination layers
- adsorption layers
- oxidation layers

Not only the materials and contacting geometries, but also the frictional kinematics and ambient conditions such as relative humidity can have a huge impact on the tribological. Thus, parameters like speed, load, duration, temperature, type of movement (rolling, sliding, indenting, etc.) and load distribution significantly affect experimental results.

Sliding and/or rolling contacts cause a change of the surface conditions. Several effects are known to affect surfaces in contact :

- adhesion and shearing
- plastic deformation
- grooving
- elastic deformation

The acting stress/strain forces are typically applied by a rolling and/or sliding movement of the two bodies. The quantitative value for the friction is the frictional force (F_R). F_R is the necessary force to keep the movement stable. For a comparison between different contact situations, the friction coefficient (f) is used (2.3) to standardize the contact by setting F_R into relation to the normal force F_N.

$$f = F_R/F_N \tag{2.3}$$

Even though many values for the coefficient of friction can be found for different material pairings (e.g. in data sheets), the friction coefficient is a system-specific parameter, which is influenced by several factors. Chemical changes at the interface of two contacting bodies may result in boundary layers and thus reducing the coefficient of friction over the lifetime. These chemical effects are not only caused by frictional heat, but also due to the formation of fresh material due to wearing off from the contact surface (Mori/ Wilfredo, 1989). The phenomena of wear are described and compared by Rigney et al. (**?**, ; Heilmann et al., 1983b; Rigney, 1997) and discussed concerning the influence of parameters affecting sliding wear. A special phenomenon is the delamination of flake-like material. The related theory was first described in the seventies (Fleming/Suh, 1977; Suh, 1977; Hirth/Rigney, 1976) especially by Suh (Suh, 1977). The theory describes the correlation between flake-like wear debris and lamellar structures as well as subsurface crack formation. The crack initiation starts by dislocation pile-ups and following voids underneath the surface. By crack propagation to the surface, long and thin sheets separate from the bulk material.

Such effects of plastic deformation are not only phenomena of solid structural parts, also contact surfaces are exposed to plastic deformation and fatigue. In those cases, cracks may occur at the surface or close to it. Joining cracks form scales of the material, which separate from the material and probably put down on other contact regions creating stress concentrations during contact loading.

Plastic deformation is known appear in both cases for sliding as well as rolling conditions. Even combinations of sliding/rolling are well studied. Since parts undergo a deformation when in contact of a counterpart, not all regions in the contact are supposed

to pure rolling contact. For example a rolling of at least one convex counterpart builds zones of slip and thus, sliding. In case of a ball rolling in a bearing, areas at the center of the contact undergo a forward sliding while areas at the edge of the contact zone undergo backward sliding. Thus, the stresses in the contact region are of high importance for an understanding of the deformation of tribological contacts.

In 1882 Hertz [Hertz] defined the contact geometries for two meeting bodies (ball and plane). Hertz defined the size of the circular contact area by the radius

$$a = \left(\frac{3 \cdot P \cdot R}{4 \cdot E^*} \right)^{1/3} \tag{2.4}$$

$E*$ is the respective Young's modulus for the contact, which is related to the Young's moduli and Poisson ratios of the two bodies in contact (E_1 and E_2 as well as ν_1 and ν_2) (Popov, 2009):

$$E^* = \frac{1 - \nu_1^2}{E_1} + \frac{1 - \nu_2^2}{E_2} \tag{2.5}$$

the pressure in the contact is defined as a function of the radius from the center of the contact to the edge of the contact zone ($0 \leq r \leq a$) by

$$P_r = \frac{3P}{2\pi a^2} \left(1 - \frac{r^2}{a^2} \right)^{1/2} \tag{2.6}$$

The depth of the indentation h can be calculated according to

$$h = \frac{a^2}{R} = \left(\frac{9 \cdot P^2 (1 - \nu^2)^2}{4 \cdot R \cdot E^2} \right)^{1/3} \tag{2.7}$$

One has to keep in mind, that due to elastic deformation, geometric values of the contact differ between loaded contacts and unloaded ones, because the material undergoes an elastic deformation during the indentation, which is reversed after unloading. In practice, most parts are made of steel, which show maximal stresses in a depth of $z = 0.49a$ according to the Poisson ratio of steel of $\nu = 0.3$ (Popov, 2009). Due to the high stresses and related maximum Hertzian pressure (e.g. (2.8) for a spherical indenter) beneath the indenting object, the highest plastic deformation can also be found around the depth of the highest stresses:

$$P_{max} = \frac{3P}{2\pi a^2} \tag{2.8}$$

Tensile stresses, which are highest at the edge of the contact zone, can lead to fatigue in this region (Linz, 2010). For a cylinder in contact with a plane the contact geometry is no more axial symmetric but symmetric to the center line of the contact.

The maximum shear stress for the contact cylinder against plane is shifted into the material to a depth of $z = 0.78a$ (Williams, 2005a). For real contacts, the small asperities

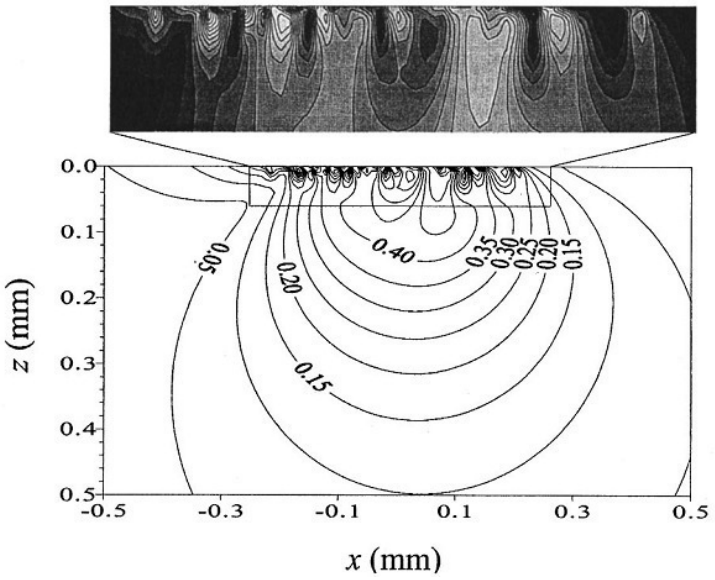

Figure 2.1: Von Mises stress under a point contact with rough surface and subjected to surface traction (contact moves from left to right); image taken from (Liu/Wang, 2002)

in the contact are the origin of smaller stress fields superimposed to the macroscopic stress fields (see figure 2.1 (Liu/Wang, 2002)). Therefore, the material can show a different response to the tribological loading of the macroscopic regions within the first micrometers underneath the surface.

Furthermore, the bulk-material underneath the contact-area gets modified by the indentation effects. For a rigid indentation, the plastically deformed zone can be estimated by estimating a radial symmetric stress/strain (Harvey et al., 1993).

$$c = \sqrt{\frac{3P}{2\pi\sigma_0}} \tag{2.9}$$

with P being the indentation force and σ_0 the yield stress. The latter also applies in cases of cyclic contacts and cyclic lateral scratches (Prasad et al., 2006). Additionally, in sliding contacts the frictionally induced shear (Rigney, 1998) is superimposed to the statically calculated strains.

Besides contacting solids, a lubricant might be present at the interface. For a characterization of the lubrication characteristics, the ratio (λ) between the minimum film thickness (h_0) and the surface roughness of the contacting bodies A and B $\sigma_{A/B}$ is used (Tallian, 1972; Stachowiak/Batchelor, 2013):

$$\lambda = \frac{h_0}{(\sigma_A^2 + \sigma_B^2)^{0.5}} \tag{2.10}$$

With the minimum film thickness calculated according to Hamrock and Dowson (Hamrock/Dowson, 1977; Hamrock/Dowson, 1981; Stachowiak/Batchelor, 2013) being:

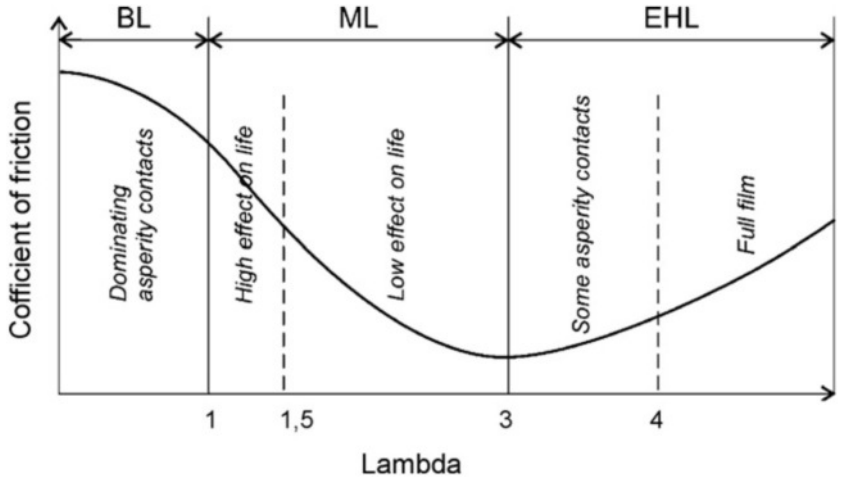

Figure 2.2: Different lubrication regimes, defined by lambda ratio; image taken from (Kalin/Velkavrh/Vizintin, 2009).

$$\frac{h_0}{R'} = 3.63 \left(\frac{U\rho_0}{E'R'}\right)^{0.68} (\alpha E')^{0.49} \left(\frac{W}{E'R'^2}\right)^{-0.073} \left(1 - e^{-0.68k}\right) \tag{2.11}$$

With U being the surface velocity in m, ρ_0 the viscosity at normal atmospheric pressure of the lubricant in Pas, E' and R' the reduced Young's modulus in Pas and the reduced radius, respectively. Furthermore, α, W, k representing the pressure-viscosity coefficient in m^2/N, the normal load in N and the elliptic parameter (1 for point contacts).

For values of $\lambda < 1$, the surface is known to undergo smearing or deformation accompanied by wear (see figure 2.2). For values of $1 < \lambda < 1.5$, the surface might be damaged by glazing (flattening of surface roughness by plastic deformation of asperities) or spalling. In case of even higher values for λ, only minor glazing is expected. Nevertheless, the damaging is not affecting operation. A complete separation of the contacting bodies is given for $\lambda > 4$.

2.1.1 Sliding

In the case of sliding, objects in contact show a relative movement to each other without a rotation (ω) of one of the objects. Due to the acting load, the materials are deformed and the laws of the Hertzian contact are also valid for sliding contacts. But the stationary stresses interfere with the stresses introduced by the tangential acting force (F_T) by the movement. The superimposed stresses at the contacting surfaces can be calculated by (for a spherical indenter and a contact zone independent of F_T) (Popov, 2009)

$$p_{(r)} = \frac{3\mu P}{2\pi a^3}\sqrt{a^2 - r^2} \tag{2.12}$$

The stresses during the sliding contact are decreased (tend to higher compression) in the front edge of the contact zone and increased (tend to higher tension) in the following contact zone edge. But the sliding also affects the depth of the highest stresses in the material. For friction coefficients of $\mu \geq 0.3$, the highest stresses shift to the surface. The corresponding normal stress is given by equation (2.13).

$$\sigma_{max} = P_{max} \left(\frac{1 - 2\nu}{3} + \frac{4 + \nu}{8} \cdot \mu\pi \right) \tag{2.13}$$

Furthermore, the indentation introduces an area of slip at the edge of the contact zone (where tensile stresses occur). The radius $r_{stick/slip}$ of the zone of sticking of the surfaces to each other can be calculated by

$$r_{stick/slip} = a \left(1 - \frac{F_T}{\mu \cdot P} \right)^{1/3} \tag{2.14}$$

The zone of sliding behavior is then defined for $a \geq r \geq c$. Equation (2.14) shows, that the radius $r_{stick/slip}$ is also a function of F_T. This means, that $r_{stick/slip}$ is fluctuating during a cyclic sliding contact for $F_{T|min} \leq F_T \leq F_{T|max}$.

The introduced strain gradients at the sliding interface lead to a plastic response of the material. In deformed materials, substructures develop by formation of low energy dislocation structures (Rigney, 1998; Rigney/Divakar/Kuo, 1992). The so formed layer usually contains deformed layers of the origin material but may also undergo mechanical mixing (Rigney et al., 1986) or chemical reaction with the counterpart or the environment (Rigney, 1988). The microstructure typically consists of grains in the size range of 10-50 nm with high-angle grain boundaries (HAGBs) (Ganapathi/Rigney, 1990). Hardness is also crucial for the mechanical behaviour of contacting bodies. It also has to be considered, that the initial hardness might not be the actual hardness during the lifetime. The surfaces in contact can undergo softening or hardening and also the build up of a new interface microstructure can lead to different hardness values (Rigney, 2000). Rice et al. (Rice/ Wayne/Nowotny, 1983) proved that switching the materials in pin-on-disk testing (disk material A and pin material B to disk material B and pin material A) also shows a different wear behaviour.

2.1.2 Rolling

When adding a rotary component to the translation of at least one of the contacting partners the sliding contact converts into a rolling contact. But most of the technical rolling contacts also have a sliding component (slip). Slip (s) especially occurs when the rolling body is accelerated (positive/negative). The slip is defined by the relation of the relative moving speed (ν) of the rolling component relative to the opposite body and the

rotary speed (ν_ω) at the contact (Popov, 2009).

$$s = 1 - \frac{\nu_\omega}{\nu} \tag{2.15}$$

with ν_ω being depending of the deformation (ϵ_x) in the contact in moving direction.

$$\nu_\omega = \frac{1}{1 + \epsilon_x} \tag{2.16}$$

The stresses in the rolling contact are similar to the sliding contact and can be seen as a superposition of sliding (2.17) introduced stresses (2.18) and stiction stresses.

$$\sigma_{slide(x)} = \sigma_1 \left(1 - \frac{x^2}{r_{slide}^2}\right)^{1/2} \tag{2.17}$$

$$\sigma_{stiction(x)} = -\sigma_2 \left(1 - \frac{(x-d)^2}{r_{stiction}^2}\right)^{1/2} \tag{2.18}$$

With corresponding radii of the different contact zones:

$$\frac{r_{stiction}}{r_{slide}} = \left(1 - \frac{F_x}{\mu \cdot F_N}\right)^{1/2} \tag{2.19}$$

The stresses σ_1 and σ_2 are related to the introduced pressure by

$$\sigma_1 = \mu \cdot P_0 \tag{2.20}$$

$$\sigma_2 = \frac{r_{stiction} \cdot \sigma_1}{r_{slide}} \tag{2.21}$$

2.2 Material properties and their influence on friction and wear

Materials can be classified concerning a wide range of properties. Due to this, a huge variation of applications were realized during the history of human technology. But even steels as one large group of prominent materials can show different values in their typical properties such as yield strength, melting temperature etc. Furthermore, residual stresses are of high importance for damage analysis in steels. Since damages usually get introduced by stresses in the material, the acting stresses are superimposed with the residual stresses in the material. For understanding the damage behaviour of cyclic tribological contacts, the material properties and the change of these properties over the lifetime are of importance.

Wear can have two main origins: material is lost from the metal surface (e.g. abrasion)

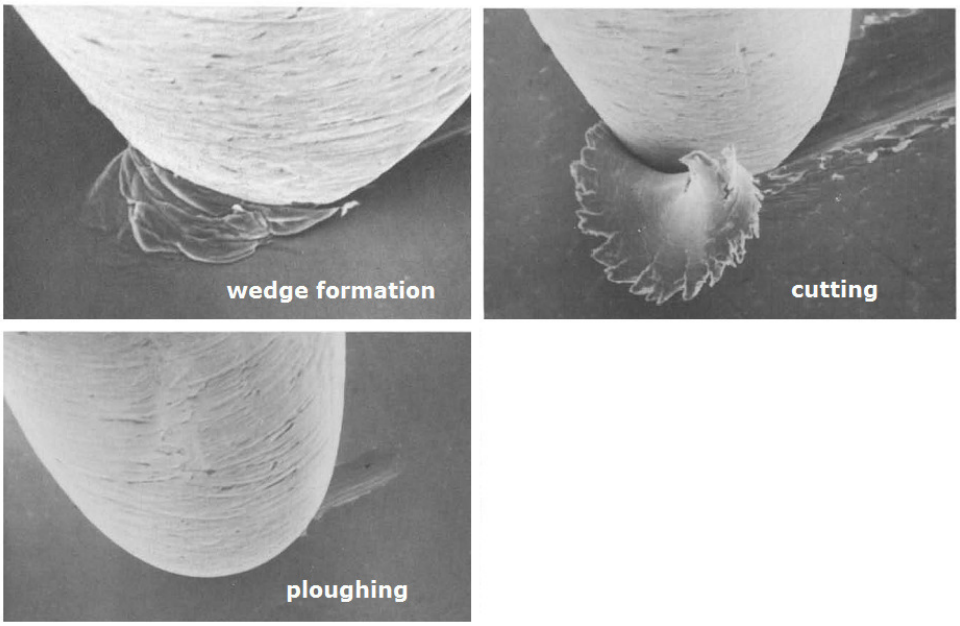

Figure 2.3: SEM images showing the mechanism of wedge formation (steel pin against unlubricated stainless steel), cutting (unlubricated brass by steel pin), and ploughing and ridge formation (steel pin against unlubricated brass); image taken from (Hokkirigawa/ Kato, 1988)

or the metal surface was plastically deformed and material got transformed to the side of the wear track. Around 1950, equations for calculating the lost volume where established (Holm in 1946 (Holm, 1946) and Archard in 1953 (Archard, 1953)). Since only a few influencing parameters are considered, these models are a simplification of wear effects (Rigney, 1988). Beside the models for calculating the worn volume, Hokkirigawa and Kato described three different models (see figure 2.3) for the behaviour of a material subjected to a harder sliding counterpart. Moreover, changes of the contact condition during the lifetime are not considered e.g. asperities might work as small sub-contacts, thus introducing plastic deformation (Johnson, 1987). Additionally, it has to be considered, that sliding wear is usually a directional effect and therefore it was shown there is a need of investigating transverse and longitudinal directions. Especially changes of the characteristics of the microstructure are of interest for a comparison between longitudinal and transversal direction (e.g. texturing).

Usually, when monitoring a sliding system, there is a start (run-in phase) and a steady state phase. During run-in, the system is neither showing a constant friction coefficient nor a constant wear rate. Here, tests might not be reproducible. But after a longer testing time, the tribological parameters become constant (Rigney, 1997). Moreover, for ductile materials subjected to sliding contacts, a small region close to the contacting surface is usually affected by severe plastic deformation. Especially during the run-in period, this might lead to further changes in the surface roughness, hardness, grain size and texturing effects (Prasad/Michael/Christenson, 2003; Prasad et al., 2006).

Tribological contacts are in most of the cases cyclically loaded. Consecutive sliding asperities between the contacting bodies further induce small changes in the material microstructure at each cycle. In some cases, this damage leads to an initiation of cracks similar as in more general fatigue applications. Crack networks introduced by sliding are usually of smaller size than those introduced by rolling. Unlike in conventional fatigue, fatigue in tribological contacts is not known to have an endurance limit below which no damage develops. Additionally, fatigue in frictional contacts does not show a low-cycle or high-cycle fatigue regime (Bayer, 2004). A general damage relation, which depends on load and number of cycles, is given by (Lundberg/Palmgren, 1947)

$$N_1 \cdot P_1^n = N_2 \cdot P_2^n \tag{2.22}$$

With the respective cycles N_1 for load P_1 and N_2 for load P_2 as well as the constant $n = 3$ for point contacts and $n = {}^{10}/_{3}$ for line contacts.

2.2.1 Plastic deformation

The different crystalline structures of metals show anisotropic mechanical behaviour on the scale of the crystal size in different directions. There exist several directions related to the Bravais lattice, where deforming of the crystal is preferred compared to others. Taking a closer look at different crystal structures, it can be seen that the packaging of atoms is different along different directions. Thus, planes of highest atomic packaging exist with a greater distance to the atoms parallel to the slip planes. Within the slip plane, dislocations can be moved by lower shear stresses than in the other planes. Slip planes of the same direction are grouped as a slip system (see figure 2.4).

Wheeler and Buckley (Wheeler/Buckley, 1975) showed the start of texturing where the slip plane normals had been tilted about 10° towards the sliding direction. Tests on Al and Ti by Farhat (Farhat, 2001) have shown, that the texturing effect also affects the run-in. According to the results of Farhat, the grain orientation changes with aligning the slip-plane normal to the surface. In addition to that, the friction coefficient also depends on the orientation of the material underneath the contact. Ti alloys as sliding materials for example with a basal texturing ((0001) plane parallel to the contacting surface) show no decreasing friction coefficient and thus no run-in period in comparison to a perpendicular alignment between the basal plane and the contacting surface (Prasad et al., 2006). This texturing impact on sliding is also known for stainless steels (Reza Bateni et al., 2005). Nevertheless, depending on the magnitude of the acting stresses, not all experiments might show the tendency for texturing or grain rotation (Heilmann et al., 1983a).

The mobility of the dislocations has a direct influence on the material properties. Plasticity of the material mainly originates from sliding of edge dislocations dominantly along the slip systems or cross slipping of screw dislocations in the lattice. At higher

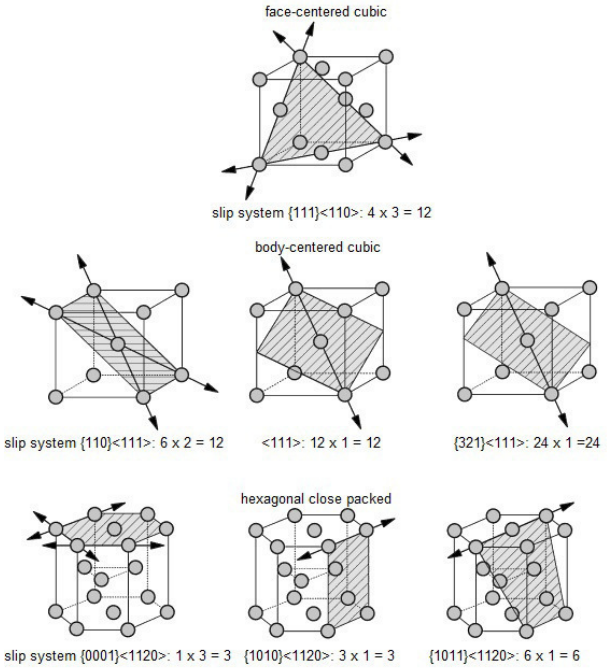

Figure 2.4: Slip systems in cubic and hexagonal crystalline structure; image taken from (Bergmann, 2008)

temperatures, edge dislocations may also climb along the lattice and normal to the slip plane. Dislocation sources such as Frank-Read sources generate new dislocations thus further supporting plasticity. The generation of new dislocations does not only facilitate plasticity but also leads to a hardening of the material since by increasing the dislocation density, the probability of piling-up at obstacles e.g. grain boundaries or in general impeding dislocations on the same slip plane rises. Some obstacles (e.g. inclusions with crystalline structure similar to the origin-grain of the dislocation) or dislocations on orthogonal slip planes can be finally cut by dislocations. Since moving a dislocation through an obstacle usually requires more energy than moving them on slip planes, the material is subsequently hardened by this process (Gottstein, 2007). Known as ageing, atoms can settle down at the dislocation line by diffusion (Suresh, 1998). These accumulations called Cottrell-Clouds also keep the dislocations attracted. Besides a hardening effect, the material also gets brittle. However, dislocations can also lead to a softening of the respective material. The previously mentioned cross slip of screw dislocations or climbing of edge dislocations can lead to a softening of the material. Furthermore, two opposing edge dislocations on the same slip plane can join each other and both dislocations can thus be erased. This effect is additionally supported by the attraction of the strains in the lattice generated by the two opposing edge dislocations (Bergmann, 2008). At the smallest level the atoms are ordered in the grains by a crystallographic order building symmetric planes of preferred slip. Since slip is an important factor of the plastic behavior, the orientation and the number of slip planes have a direct effect especially on

the fatigue initiation (Suresh, 1998). The cyclic stress by sliding contacts can introduce new or move the present dislocations to join together as new (sub-)grains even in initial single crystal materials (Prasad et al., 2006). Apart from the formed grains, nanocrystalline layers might develop if the cyclic stresses reach sufficient magnitudes (Rigney, 2000; Rigney et al., 2003; Prasad/Michael/Christenson, 2003; Rigney, 1998; Perret et al., 2010). At the larger level, the structure of the grains also influences the fatigue of solids. The boundary works as a barrier for gliding dislocations in the material. Piling-up at the boundary, dislocations introduce local plasticity, in which cracks may appear. Depending on the intersection, dislocations can also be absorbed in the grain boundary. Smaller grain sizes imply higher grain boundary density and thus more grain boundaries, which have to be passed by the crack on its way through the material. As far as the orientation of grain boundaries as obstacles are concerned, two basic scenarios for the crack propagation are possible (Kumar/Curtin, 2007):

1. kink angle: the crack faces the boundary and propagates in the next grain with a tilt but starting from the same line of the crack front at the boundary. The influence on crack pinning is low.

2. twist angle: the crack propagation in the next grain is aiming at the same direction as in the former grain but the plane is twisted at the interface. The influence on crack pinning is high.

Stacked grains may also force the crack to split into two separate cracks propagating at two different crack planes in the respective grain. The presence of second phases in the microstructure is also known to influence the crack propagation in several ways. The crack might pass through the inclusion (particle cracking) or make its way around it (interface debonding) depending on the microstructural configuration of both phases and the interface constellation (Linz et al., 2016). But one has to consider, that also crack propagation may introduce second phases along the crack path (Holzapfel et al., 2007).

2.2.2 Plastic deformation of dual phase steels

The mechanical properties and thus, the plastic deformation of steel consisting of more than one phase strongly depend on the fraction of each material and its single properties. However, the interaction of the two different phases and its mismatch during deformation is also of importance (Ankem et al., 2006). Apart from modeling for rolled microstructures (Bouaziz/Le Corre, 2003), particular models were developed to calculate the mechanical properties of a ferritic/pearlitic steel, based on the fraction of the individual phases and its properties. By mean field approaches and numerical simulations for ferrite-pearlite steels (Terada et al., 2004; Peng/Fan/Zeng, 2001), Allain et al. (Allain/Bouaziz, 2008) developed a microstructure based modeling for the mechanical behavior of ferrite-pearlite

steels. The model of the group continues the previous work by including size parameters such as pearlite island size and the interlamellar spacing.

2.2.3 Residual stresses

Residual stresses are mostly related to the thermo-mechanical treatment of the material. The primary influence on the residual stresses is done by the heat treatment as an important contribution to the manufacturing process of a wide range of machine parts. During the tribological testing, the samples undergo a change in the residual stresses in the contact region. Depending on the development of these stresses, the material might tend to crack. The influence of the tribological testing is somehow similar to a cold working of the material. Cold working of steel typically creates compressive stresses in a region close to the surface. With increasing stresses in the material, the probability of fracture gets higher until the material fails by cracking. Calculations by Dang Van (Dang Van/Maitournam/Van, 1993) show, that for the case of rolling and sliding, a steady state of plastic shear strain with related residual stresses is reached even after the first cycle. Hardening a steel has a high influence on the residual stresses in the material, these can be both positive and negative for the later application. Nowadays, several hardening processes are established in the industry. One common hardening process is quenching and tempering (Bargel/Schulze, 2008). Some steels transfer into a metastable martensite phase when they undergo rapid cooling. This cooling can be performed by quenching the heated (furnace, induction, flame) part into e.g. water, oil, salt-bath or liquid nitrogen or even different combinations i.e. first quenching in water and a following quenching in oil.

The crystalline structure of the martensite phase is less dense packed than the rest of the material. By that, the martensite phase possesses a larger volume. In general, hardening produces compressive stresses in the surface area (Merkel/Thomas, 2008; Roos/Maile, 2011; Yin/A, 2011; Senthilkumar et al., 2011) whereas tensile stresses can occur in the core of the parts but also the opposite may occur especially for core hardened samples when the thermally induced volume change dominates the phase transformation related volume change (Totten/Inoue/Howes, 2011). The previously applied compressive stresses reduce the resulting stress when tribological contacts lead to tensile stresses in the material. Reducing the resulting tensile stresses is a very important aim of the manufacturing process to avoid fatigue in the surface area. Thus, depending on the heat treatment, a tempering might be crucial for the performance of the material.

After heat treating the material, parts are usually exposed to a couple of surface treatments. Both for taking off the waste layers formed during the heat treatment and for generating a application mandatory surface finish, grinding will be applied in most of the technical cases. This also has an influence on the residual stresses in the material as e.g. heat treatment introduced compressive stresses are reduced due to the applied tensile

stresses by the grinding medium (Grum, 2001).

As mentioned earlier, residual stresses in the material play an important role in introducing fatigue damage into the material. In the work of Kuo and Cohen (Kuo/Cohen, 1983) it is shown, that samples fatigued by tensile/compression testing show a three stage behaviour for low-cycle fatigue:

1. increase of compressive stresses at the beginning of the testing
2. decrease of compressive stresses to a final level
3. no increase or decrease of stresses until failure

2.2.4 Phase changes

The phase change of steels to strain-induced martensite is a widely found phenomenon (Hsu/Ahn/Rigney, 1980; Zhengyi/Jian/Yuzhi, 1990). Several cases of tribological stressed samples reveal a white-etching layer underneath the wear surface. The microstructure of the so called friction martensite (Zhengyi/Jian/Yuzhi, 1990) cannot be resolved in an optical microscope. The layer shows a nanocrystalline microstructure with average sizes of $\approx$ 30 nm. Electron diffraction analysis showed both α- and γ-phase. The layer is resistant to tempering up to 500°C. No carbides were found (Zhengyi/Jian/Yuzhi, 1990) in the white-etching layer. However, in other studies, carbides were found in such zones (Walzhofer et al., 2014; Linz et al., 2016). Zhengyi et al assume that this might be explained by the white-etching layer being saturated of carbon. The white etching effect occurs due to the high corrosion resistance of nanocrystallized microstructures. Zhengyi et al. describe the formation of friction martensite by two superimposed mechanisms:

- acting stresses fragment the grains, which align in the shear direction
- heat (introduced by friction and deformation) activates the formation of austenite. Due to the small size of the area of higher temperature compared to the compound an rapid cooling occurs transfering the austenitic regions into martensite.

2.2.5 Hardness

The hardness of the material or more specific the relation of the hardness of the materials in contact is usually the first mentioned material property influencing wear. Considering the hardness as a wear influencing parameter one has to keep in mind, that the value of hardness is not a fixed parameter in the tribological system. Thus, the hardness might show gradients over the contact diameter, sample depth and lifetime (e.g. by microstructural changes; see chapter 2.2.6) and might be influenced by set-up parameters such as temperature, contact speed and environment (Rigney, 1994; Dufrane/Glaeser,

1976). Furthermore, by changing hardness, the yield strength of the affected material also changes according to the Tabor relation:

$$p \approx 3Y_0 \tag{2.23}$$

for Brinell testing (for Vickers testing 8 % have to be added to the representative strain) (Tabor, 1996). Nevertheless, Vickers indentations have the advantage of more clearly defined boundaries and the indentation size effect is smaller compared to a spherical indentation (Tabor, 1970). Comparisons of different material pairings in pin-on-disk testing showed a separation between severe and mild wear according to the relation between the hardness of the disk (H_d) and the hardness of the pin (H_p). For H_d/H_p greater than 1, mild wear and for H_d/H_p ratios lower than 1, severe damage was found (Akagak/Rigney, 1991; Rigney, 1997).

2.2.6 Loss, change and transfer of material

Beside the measured wear volume, the wear debris are also characteristic for the type of wear. The released particles from the contact may change in size, and chemical composition (Rigney, 1981; Heilmann et al., 1983b), since the wear phenomena may also change during the testing. Beside the loss of material, transfer material might be added to the opposite contact partners already at the beginning of the sliding contact (Rigney, 1997; Rigney, 2000). This is known not only for unlubricated but also for lubricated systems. The material transfer is usually an adhesion supported effect and can be influenced by using different material pairings. If the bulk material does not provide good tribological properties, surface treatment (Gachot et al., 2017) or coatings (Hintermann, 1984) might be an option. Moreover, the material pairing could change during the lifetime of the contact (Sexton/Fischer, 1984). In fact, not only the solid contacting bodies can affect the formation of layers but also the environmental components (atmosphere, lubricant etc.). In this case, the lubricant can be protective against a reactive atmosphere or deliver the reactive components by itself. Due to the change (chemical, crystallographic) of the material in the contact area, the wear particles also change in their characteristics as described before. Thus, the material in the contact region undergoes a constant mixing similar to mechanical alloying (Rigney et al., 1984; Rigney, 2000) with nanocrystalline grain sizes (Ganapathi et al., 1990; Ganapathi/Rigney, 1990). The hardness of the new formed material might be harder or softer than the bulk material and thus influence the sliding, the wear debris and the wear volume (Rupert/Schuh, 2010) (Rigney, 1994). The formation of layers of different material is also affecting the crack propagation. Typically, flake-like debris are found due to material spall-off by delamination of the formed layer (Suh, 1977; Fleming/Suh, 1977; Alpas/Hu/Zhang, 1993). The formation and segmentation of wear debris can also be seen in a positive way since the material is not lost at all

but the volume is still available in the contact, either as protective transfer layer or as solid lubricant (Singer, 1996) Moreover, this leads to a re-thinking of the wear definition of lost volume and alternative descriptions of wear (Godet, 1984; Godet, 1990; Singer, 1996).

2.2.7 Temperature

Another factor of damaging the counterparts is the influence of the temperature. It is well known, that frictional contacts raise the temperature at the contacting surfaces. This effect is even more complex when considering the distribution of the asperities and the related distribution of temperature increase on the asperity level (Lai/Cheng/Cheng H S, 1985; Kuhlmann-Wilsdorf, 1985; Kuhlmann-Wilsdorf, 1987). This even leads to elevated temperatures at low speeds (Kalin, 2004). As mentioned before, temperature changes can also influence the microstructure.

2.3 Fatigue

One out of many definitions for fatigue is made by (Hoeppner, 1997):

> *"the process of progressive localized permanent structural change occurring in a material subjected to conditions that produce fluctuating stresses and strains at some point or points and that may culminate in crack or complete fracture after a sufficient number or fluctuations"*

In tribological contacts, fatigue is likely to evolve at stress concentrations at the surface such as roughness peaks or particles between the contacting surfaces. Even particles with an abrasive origin of the substrate material can cause such stress concentrations (Dwyer-Joyce, 2005). Oxidation of the surface may further support the propagation of cracks due to contamination of the crack surface (Vuorinen, 2008). A fatigue related crack only grows under cyclic stress, tensile stress and plastic strain conditions. Compressive stresses can only result in fatigue, when they also cause tensile stresses (Morris/Chung/Chung, 1997). Fatigue cracks are usually initiated through cyclic plastic deformation based on microstructural changes (Christ, 1997) when local stresses and plastic strain are concentrated by nearby voids, inclusions, twin boundaries, grain boundaries, stronger second phases and notches (Gross/Lampman, 1997). The progress of fatigue can be divided into five phases: (Morris/Chung/Chung, 1997):

1. change of microstructure (e.g. plastic deformation)
2. forming of small cracks
3. development of dominating cracks by joining microscopic flaws

4. propagation of these favoured cracks

5. failing of the part by complete fracture

Surface damage starts with an introduced micro-crack. These cracks can be initiated at the surface or at tensile maxima under the surface (e.g. inclusions). The tension inside the material is caused by stresses (e.g. Hertzian stresses (Hertz, 1881)) due to the loading contact of two bodies. In the first state, only microscopic cracks are introduced. These cracks grow to larger macroscopic cracks and connect with each other or the surface, which leads to a specimen failure (Alfredsson, 1998; Schijve, 2004). Cracks introduced at the surface arise mostly after topographic peaks in rolling direction (Ringsberg, 2000). From there they grow backwards at a shallow angle and stop mostly after 10 µm to 30 µm. Some of them grow deeper into the material causing spalling damage. Surface quality, residual stress, environment, constant or variable amplitude are essential effects for crack initiation and growth. The crack initiation is mainly caused by the movement of dislocations thus leading to plastic deformation.

2.3.1 Material deformation and crack initiation

The deformation of the material encountered by a cyclic load starts with a hardening effect in the single crystals (or inside single grains). More dislocations are pumped into the material. When a primary glide system is present, dislocations begin to glide on the primary slip planes until they pile up at the surfaces (building slip marks) or at grain interfaces until they get trapped in the material (e.g. dislocation dipoles). The dislocations piling up at grain boundaries cannot pass through the interface to the other grains (except if the crystal structure is very similar oriented to the pristine grain). However, these dislocation pile ups can work as dislocation sources in neighboured grains (Wiese, 2010). The movement of the dislocations is also impeded by the high dislocation density ($>10^{11}\mathrm{m}^{-2}$) while they form up into a vein-like structure, which can also interact with interfaces such as grain boundaries or inclusions. The pile-up of dislocations (with same sign) at grain boundaries even builds a stress concentration, which might work as a nucleation for cracks. In addition to this hardening effect (Petch, 1953), cyclic load can also rearrange the dislocations in a softening manner. With an increasing number of cycles, the dislocation veins can be broken then forming so-called persistent slip bands (PSB). Those PSBs consist of walls with higher dislocation densities ($\approx 10^{9}\mathrm{m}^{-2}$).

The cyclic load initiates a movement of the material along those PSBs. While shearing material forth and back, irregularities cause a state where the movement becomes irreversible. Therefore, flaws develop, which agglomerate to larger defects representing a potential start of a crack. The volume of these defects is transferred to the surface, building extrusion and intrusion marks at the interface where the PSB approaches the surface

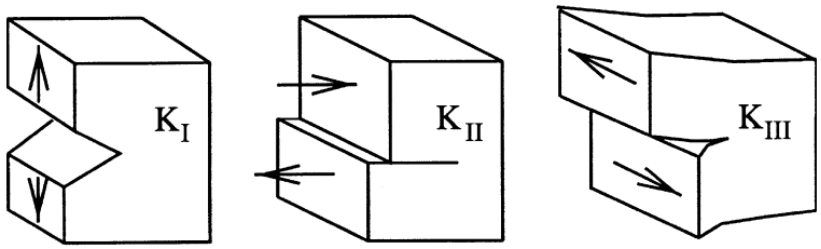

Figure 2.5: Schematic illustration of mode I (K_i) or tensile opening (left), mode II ($K_I I$) or in-plane shear opening (middle) and mode III ($K_I II$) or anti-plane shear opening (right); image taken from (Pan/Sheppard, 2003)

(Roesler/Harders/Martin, 2007) or other interfaces. The bulging of the material at the end of the PSBs facing the surface provides local stress concentrations. Thus, cracks can develop at the surface contact of the PSB and grow into the material e.g. along the soft PSB. A similar effect can occur if the PSB hits a high-angle grain boundary instead of the surface. Therefore, the stresses produced by the shearing of the material can even cause a crack at the boundary between the grains. Inclusions and pores even create more interfaces for PSBs to interact and especially stress concentrations (notch effect) for crack nucleation. For that reason, impurities such as inclusions and pores downgrade the fatigue behaviour of the material. The crucial factor for the material to crack is the locally acting strain.

A crack initiated and propagating in a certain direction maybe derived by three general types of force constellations (see figure 2.5) (Roesler/Harders/Martin, 2007). Mixtures of the modes are also possible.

- mode I: tensile crack opening
- mode II: crack opening by in-plane shearing
- mode III: crack opening by anti-plane shearing

Depending on the mode, different configurations of dislocations appear in front of the crack tip (propagating through a single crystal). In case of mode I cracking, edge dislocations move in two slip planes in a certain angle to the crack plane, while the dislocations slip plane for mode II (edge dislocations) and mode III (screw dislocations) cracking is located in the crack plane. TEM images showing mode I, II and III cracks in different metals are presented in (Ohr, 1985).

2.3.2 Fatigue effects by tribological contacts

Heilmann et al. (Heilmann et al., 1983a) investigated the subsurface structure formation in copper subjected to sliding contacts. Even for low durations of sliding contacts, introduced plastic strain and large lattice-rotations were found. The rotation-axis is described by

Heilmann et al. (Heilmann et al., 1983a) as "normal to the sliding direction and parallel to the sliding interface".

2.4 Methodology and its application to tribology

Approaching material phenomena in tribology, a well selected combination of characterization methods is mandatory. In the past, several analysis techniques became focused at when analyzing fatigue problems aiming at different aspects of cyclic damaging.

2.4.1 Hardness measurements

Conducting hardness measurements with smaller loads (so called micro hardness) the elastic energy is not sufficient for crack propagation and thereby, the hardness relates to a true measure of the plastic properties (Tabor, 1996). Nevertheless, higher hardness values are expected for smaller loads since the sample preparation hardens the surface and thus, smaller indentations are more influenced by effects from regions closer to the surface (Tabor, 1970). For materials containing several phases, the size of the indentation and thereby the load should be sufficient to penetrate a sufficient amount of grains for a representative measurement. That also applies for polycrystalline materials consisting of large grains. The relation between hardness and the indentation geometry is further described by the indentation size effect (Durst et al., 2006).

2.4.2 X-ray diffraction

Diffraction of x-rays is a well established method analyzing the crystallographic information in material science.

The information gained by x-ray diffraction (XRD) is in dependence on the absorption A of the radiation in depth d, which itself depends on the angle of incidence ω_{in} and the angle of diffraction θ according to

$$A(d) = 1 - e^{\mu_{abs} \cdot d(\frac{1}{sin\omega_{in}} + \frac{1}{sin(2\theta - \omega_{in})})} \tag{2.24}$$

with the material dependence by the coefficient of absorption μ_{abs} (Spieß et al., 2009). Or vice versa the intensity of diffracted x-rays related to the original intensity entering the sample as a function of depth d (Macherauch/Zoch, 2011):

$$\frac{I_z}{I_0} = e^{(-\frac{2\mu_{abs}d}{cos\phi})} \tag{2.25}$$

In 1921 W. L. Bragg established the relation for which circumstances x-rays are getting diffracted at a crystal lattice show constructive interference:

$$2Dsin\theta = n\lambda \tag{2.26}$$

According to this, the interference is only constructive when the angle is set to meet the equation (2.26) with D being the lattice spacing and λ the wavelength or multiples of λ. Also of importance for material analysis is the shape of the diffraction peak over the diffraction angle. Especially the full width at half maximum (FWHM) is of importance concerning material properties like the dislocation density or domain (grains, sub-grains,...) sizes. It was also shown (Kuo/Cohen, 1983) that the FWHM-values undergo a three stage development in low-cycle fatigue, which is nearly changing at the same cycle values as the stresses:

1. increase at the beginning of the testing
2. a continuous level is reached
3. a further increase until failure

residual stress measurements Residual stresses are stresses in a body without any external acting forces or temperature gradients and are categorized in three orders according to the range of the stress influence, which usually are combined in technically used materials (Macherauch/Zoch, 2011):

- residual stresses of first order: homogeneous distribution of the residual stresses over several crystallographic domains (e.g. grains). For a stable body, the forces on an imaginary plane through the body are in equilibrium as are the momentums on the axes.
- residual stresses of second order: homogeneous distributions of the residual stresses in the range of the size of crystallographic domains. The force/momentum equilibrium is only valid for a specific amount of crystallographic domains e.g. several grains.
- residual stresses of third order: inhomogeneities of residual stresses even for small crystallographic areas on atomic scale. The equilibrium is usually given for a small area such as e.g. a single grain.

Further categorizations are listed in (Spieß et al., 2009). If several phases are present in an material, it also has to be considered how the stresses distribute on the single phase when applying external stresses. This is mainly influenced by the relation of the respective Young's moduli E_i of the phases (Spieß et al., 2009).

The measurement of residual stresses in crystalline materials by XRD is based on the assumption that the deformation changes the lattice spacing D of the crystal by

the rules of Hooke's law. The difference of the measured D to a reference value D_0 from a "stress-free" state is defined as the residual stress in the material. Therefore, the residual stress measured by XRD is in general residual stress of third order. Having a polycrystalline material, several grains fulfill the Bragg condition and contribute to the constructive interference of the radiation. A rotation of a crystal around ϕ would still result in a crystal contributing in the constructive interference. Despite the information is gained from the nano-meter scale, the beam of X-rays is not focused to such a small scale. Hence, the information is gathered over the width of the beam with respect to the distribution of intensity (Macherauch/Zoch, 2011). Depending on the relation of the width of the X-ray spot and the size of the crystallographic domains, the information is collected over a number of domains and thus, a superposition of information from several crystallographic orientations by the domains (Macherauch/Zoch, 2011). As we have seen before, the information gathered is a surface close value (depending on the sample material and the X-ray beam characteristics). Thus, the assumption can be drawn, that the strain and stresses normal to the surface should be small thus neglectable, leaving a state of plane stress parallel to the sample surface (Macherauch/Zoch, 2011). Also known is the relation of stresses in the two directions parallel to sample surfaces subjected to stress. Therefore, lateral stresses show a dependence of stresses in their normal direction (lateral) with the opposite characteristic. For example, compressive stresses in one direction cause tensile behaviour normal to this plane (Spieß et al., 2009).

2.4.3 EBSD basics

Since EBSD is the key method of this work, the technique is described in more detail compared to other methods. The method of using backscattered electrons for materials analysis becomes more popular, especially due to the availability of commercial devices. Today, it is considered a standard tool in scientific areas such as geology (Randle, 2008; Prior et al., 1999). One advantage of EBSD is the range of information about a crystallographic sample (Randle, 2009) in particular microstructures (Lee/Rollett/Rohrer, 2007; Humphreys/Bate, 2007; Humphreys, 2004; Xu et al., 2007; Humphreys, 1999; Swalla/Neu/McDowell, 2004; Black/Higginson, 1999), texture (Petrov et al., 2007; Dingley/Randle, 1992; Bachmann/Hielscher/Schaeben, 2011; Zaafarani et al., 2006), grain or phase boundary characteristics (Humphreys et al., 1999; Prasad/Michael/Christenson, 2003; Humphreys, 2001; Cai/Bellon, 2012; Humphreys/Bate, 2006), phase identification (Klimek/Pietrzyk, 2004; Chen/Thomson, 2010; Zaefferer/Romano/Friedel, 2008; Wilson/Madison/Spanos, 2001), and introduced strain analysis (Calcagnotto et al., 2010; Kamaya/Wilkinson/Titchmarsh, 2005; Brewer et al., 2006; Brewer/Field/Merriman, 2009; Perret et al., 2010; Mingard/Gee, 2007; Kamaya, 2011; Gee/Mingard/Roebuck, 2009; Swalla/Neu, 2006; Man et al., 2010; Wright/Nowell/Field, 2011).

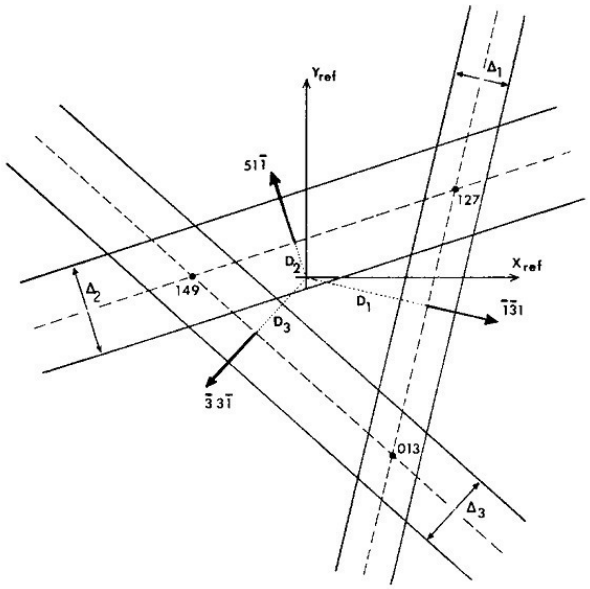

Figure 2.6: Example of a Kikuchi pattern of a crystal (schematic); image taken from (Heilmann et al., 1982)

With the steady increase of computer performance, the method of electron backscatter diffraction gained more importance due to faster data processing. In this context, the first commercial device entered the market in 1986 (Dingley, 1984; Dingley, 1987; Dingley, 2004). Backscattered electrons with the origin of the e-beam can be used to obtain a material specific contrast. Electrons are typically backscattered out of a depth up to 50 nm underneath the surface (e.g. $\approx$ 40 nm for Si or $\approx$ 10 nm for Ni). But beside the value of the intensity due to the electrons leaving the crystal at a defined spot, the direction of these electrons also depends on the diffraction according to the Bragg condition related to the atomic lattice planes of the crystal. The electrons are backscattered in a Kossel cone with the cone beeing symmetrical to the lattice plane. Hitting the phosphorous screen the electrons cause a glowing at the impact areas of the phosphorous screen. Thus, the so called Kikuchi lines form at intersections of the Kossel cones and the phosphorous screen. The diffraction pattern at the phosphorous screen is then detected by a CCD camera filming the screen (Dingley/Randle, 1992). For that reason, the pattern captured by the CCD camera is in dependence of the crystal structure. Thereby, the phosphorous screen shows a pattern of various lines, the so called Kikuchi lines (see figure 2.6), according to the lattice diffraction planes in the crystal. A correlation of the Kikuchi lines to the related atomic lattice is shown in (von Heimendahl/von Heimendahl, 1980) for a cubic system. The spacing Δ of line n is determined by

$$\Delta_n = \frac{\lambda L}{a}\sqrt{h^2 + k^2 + l^2} \tag{2.27}$$

the camera constants λ (wavelength) and L (camera length) is a constant for all the

lines as well as the lattice parameter a. Furthermore, the ratio Δ_1/Δ_2 of two spacings is independent of the constants (λ, L, a). Additionally, the angle between the Kikuchi lines is independent of λ, L, a and determined for a cubic system by

$$cos\alpha = \frac{h_1h_2 + k_1k_2 + l_1l_2}{\sqrt{h_1^2 + k_1^2 + l_1^2}\sqrt{h_2^2 + k_2^2 + l_2^2}} \tag{2.28}$$

Knowing the angle between the Kikuchi lines and the spacing, it is possible to calculate the crystal orientation to the surface when the Bravais lattice is known. Computer automated analysis of the pattern can be performed (Heilmann et al., 1982) and the orientation can be drawn for each point scanned by the electron beam. Thus, an automated mapping of the orientations of the crystalline structure to the surface can be obtained (Humphreys, 2001; Wrights/Zhao/Adamsf, 1991; Wright/Adams, 1991; Wright/Adams, 1992). Moreover, the Kikuchi pattern is also representative for the crystallographic classification and thus, the phase of the diffracting material (Baba-Kishi/Dingley, 1989) especially when combined with energy-dispersive X-ray spectroscopy (EDS) (Dingley, 2004). Hence, determination of the volume fraction of the contained phases is possible (Wilson/Madison/ Spanos, 2001). Furthermore, the distance between the band edges of the Kikuchi patterns can be used for high-resolution measurements of the lattice spacing by implying the Bragg equation ((Krieger Lassen, 1998)). For ideal quality of the diffraction pattern, the phosphorous screen has to be placed precisely as coplanar to the surface. Moreover, the pixels of the camera can be grouped together to work as "super pixels". This leads to an improvement in the camera sensitivity and by that in the pattern collection speed (Randle, 2009).

Resolution As far as spatial resolution is concerned, several factors have to be considered: the electron source, material (e.g. atomic number), beam acceleration voltage, beam current and specimen alignment. For brass, best spatial resolutions are located in the range of 25 nm (tungsten filament SEM) or 9 nm (field Emission Gun Scanning Electron Microscopy (FEGSEM)) (Humphreys, 2001). The angle between the specimen and the electron beam is important since the irradiation of electrons in an angle widens the irradiation spot to an elliptic shape. The resolution for an field emission source and an aluminum sample is less than 100 nm (Humphreys/Brough, 1999) or e.g. for the previously mentioned brass, the spatial resolution is 75 nm (tungsten filament SEM) or 27 nm (FEGSEM) in normal direction to the tilt axis (Humphreys, 2001). For effective data processing, the scanning step size should be in consideration of an effective resolution (N_S) by these influences giving an effective resolution of

$$N_S = \frac{(D_A - \Lambda_A)(D_P - \Lambda_P)}{D_A D_P} \tag{2.29}$$

with the mean grain size in parallel (D_A) as well as (D_P) perpendicular to the tilt

axis and the effective spatial resolutions Λ_A and Λ_P (for 70° tilted samples: $\Lambda_P \sim 3\Lambda_A$). With a volume fraction (F_V) of a second non-indexed phase present in the sample which patterns are not indexed, N_S has to be multiplied by $1/(1-F_V)$ (Humphreys et al., 1999). For a proper determination of grain sizes by EBSD, a minimum of ~ 200 grains have to be taken into consideration with ~ 10 measured spots per grain (Randle, 2009). Furthermore, grain sizes measured by EBSD might turn out bigger than by SEM since EBSD typically separates between high-angle grain boundaries ($> 15°$) and low-angle grain boundaries (LAGBs). When including the low-angle boundaries, the value becomes more similar to the values determined by SEM (Humphreys, 2001). Optimum resolutions are obtained for intermediate probe currents and field emission sources (Humphreys/Brough, 1999). Besides lateral resolutions, the angular precision of approximately 0.1° was determined experimentally by El-Dasher et al. (El-Dasher/Adams/a.D Rollett, 2003).

Pattern quality While the beam spread in the sample is increased by higher acceleration voltages, the quality of the pattern decreases for lower acceleration voltages by the decreased efficiency of the phosphorous screen (Humphreys, 2001). Furthermore, the quality of the pattern depends on the quality of the crystallographic structure. Thus, images with poor pattern quality might be areas of high defect density or close to the grain boundary. Assuming that recrystallized regions contain less defects such as dislocations, automated methods for determination of recrystallized fraction have been developed (Black/Higginson, 1999; Dingley, 2004). Moreover, the pattern quality is used as a tool to estimate the plastic strain stored in the material (Wilkinson/Dingley, 1991) with respect to other pattern quality influencing parameters (Humphreys, 2001; Randle, 2009) such as grain boundaries, surface topography, second phases, beam conditions, sample preparation and camera settings (Wright/Nowell/Field, 2011).

Plastic strain Intragrain orientation changes can be interpreted as misorientations caused by introduced plastic strain (Raabe et al., 2002). Since the orientation per scanned pixel is one of the main information gathered by the EBSD method, the tool is sensitive for analyzing misorientations and thus, plastic strain (Wright/Nowell/Field, 2011) considering the angular precision (El-Dasher/Adams/a.D Rollett, 2003).

As the crystallographic orientation of the measured spots is the main information gathered by EBSD measurements, it has to be considered that the determination of absolute orientation is influenced by a couple of geometrical factors lowering the accuracy. Nevertheless, the relative orientation between each measured spot is higher. Very small orientation differences are difficult to perform due to "orientation noise" effects (Humphreys/Brough, 1999). This effect can be minimized by using higher acceleration voltages narrowing the Kikuchi bands (Humphreys, 2001). Crystals with low symmetry such as monoclinic or triclinic minerals might lead to problems with the automatic pattern analysis

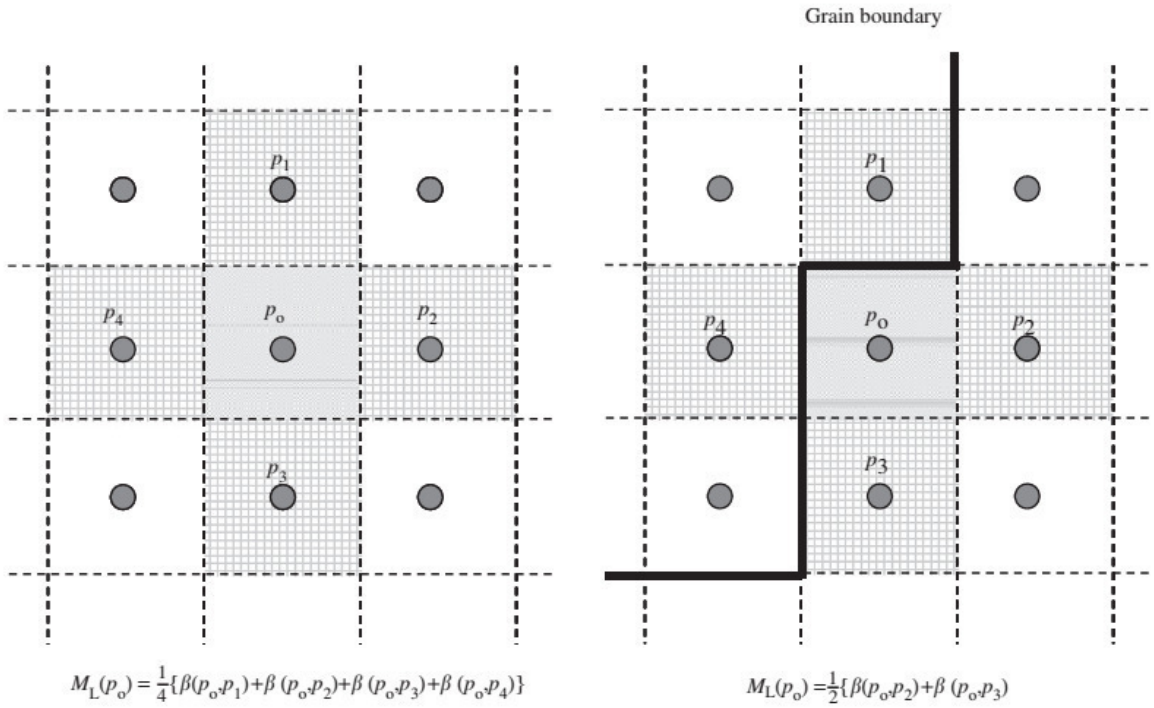

Figure 2.7: Pixel configuration for determination of misorientation for pixel p_0 and with special respect to grain boundaries (right); image taken from (Kamaya, 2009b)

since the recognition routine might be mislead by pseudo-symmetry (Prior et al., 1999). The differences between the crystallographic orientations of grains interfaced by grain boundaries is usually expressed by angles needed for aligning one of the crystallographic structure to the other (Mackenzie, 1958; Hutchinson et al., 1996).

In this analysis, it is considered, that the change of orientation is due to geometrically necessary dislocations (Adams, 1997) and thus, due to plastic deformation stored by these dislocations. Since the information of the orientation is gained for each pixel in the EBSD mapping, the measurement of orientation information by EBSD might be used for evaluation of plastic deformation in materials. One approach is to compare the orientation of a pixel with its neighbouring pixels. A simple way to calculate the misorientation for on element of a EBSD mapping can be performed with equation (2.30) (Kamaya, 2009b)

$$M_{L(p_0)} = \frac{1}{4}\sum_{i=1}^{4}\beta(p_0, p_i) \tag{2.30}$$

Figure 2.7 shows the geometric relation for equation (2.30) with $\beta(p_0, p_i)$ being the misorientation between p_0 and one of the neighbouring pixels (p_1, p_2, p_3, p_4) and with respect to a possible grain boundary separating p_1 and p_4 as pixels of the neighbour grain due to higher misorientation between p_1 and p_4 regarding to p_0.

The so called kernel average misorientation (KAM) method is used for very local gradients of orientation. Depending on the range of neighbouring pixels (kernel) the

Table 2.1: Comparison of different methods for imaging misorientation (Wright/Nowell/Field, 2011; Lehockey/Lin/Lepik, 2000)

GOS	is calculated for a	grain	as the	average	of	all points in grain	and each point in grain
GAM		grain		average		all points in grain	each neighbour point
KOS		center point of kernel		average		all points in kernel	each point in kernel
KANM		center point of kernel		average		all points in kernel	each neighbour point
KACM (a)		center point of kernel		average		center point of kernel	each point in kernel
KACM (b)		center point of kernel		average		center point of kernel	each point on kernel perimeter
IMD		grain		deviation		each point in a grain	grains average misorientation

implied distance and thus, the sensitivity can be set. Apart from the KAM method, which is sensitive to short gradient ranges, it is possible to investigate the deviation of orientations over the entire grain (Kamaya/Wilkinson/Titchmarsh, 2005; Brewer et al., 2006). The main difference to the KAM method is the use of an orientation as the reference orientation to which the deviation of misorientations in a grain is analyzed. This reference orientation is defined for each analyzed grain. Thus, the latter methods are suitable for studying of orientation gradients over the whole grain. The difference between (Kamaya/Wilkinson/Titchmarsh, 2005) and (Brewer et al., 2006) is the definition of the kernel as the reference for the analysis. While (Brewer et al., 2006) use the pixel with the lowest kernel average misorientation (defined by KAM) as reference orientation, the grain average orientation could be also used (Kamaya/Wilkinson/Titchmarsh, 2005). In addition to that, these methods can be used as a tool for analyzing plastic deformation due to the analyzed intergranular misorientation (Brewer/Field/Merriman, 2009).

Figure 2.8 illustrates the difference of the two misorientation mappings kernel average misorientation and integrated misorientation map according to the IPF map and the grain boundary mapping. The "KAM effect", which is affected by local orientation gradients, can be clearly identified. The integrated misorientation map shows larger areas of misorientation.

Further variants of misorientation imaging methods are the grain orientation spread (GOS) (Barton/Dawson, 2001; Wright/Nowell/Field, 2011), grain average misorientation (GAM) (Wright/Nowell/Field, 2011), integrated angular misorientation density (IMD) (Lehockey/Lin/Lepik, 2000) or also called average intra-grain misorientation (Swalla/Neu, 2006; Chandrasekaran/Nygårds, 2003) with values based upon the deviation of misorientation in a grain. Table 2.1 shows an overview on the common methods for misorientation visualization. Moreover, one has to be careful performing analysis of plastic strain on materials. The results might depend on the parameters set for conducting the EBSD mapping while the stress situation might not be comparable to others (Brewer/Field/Merriman, 2009).

When conducting an analysis based on intra-granular misorientation measurements by EBSD, it has to be considered that the misorientations are typically between 0.1° to 2° and therefore typically located in the range of errors associated with geometrical problems

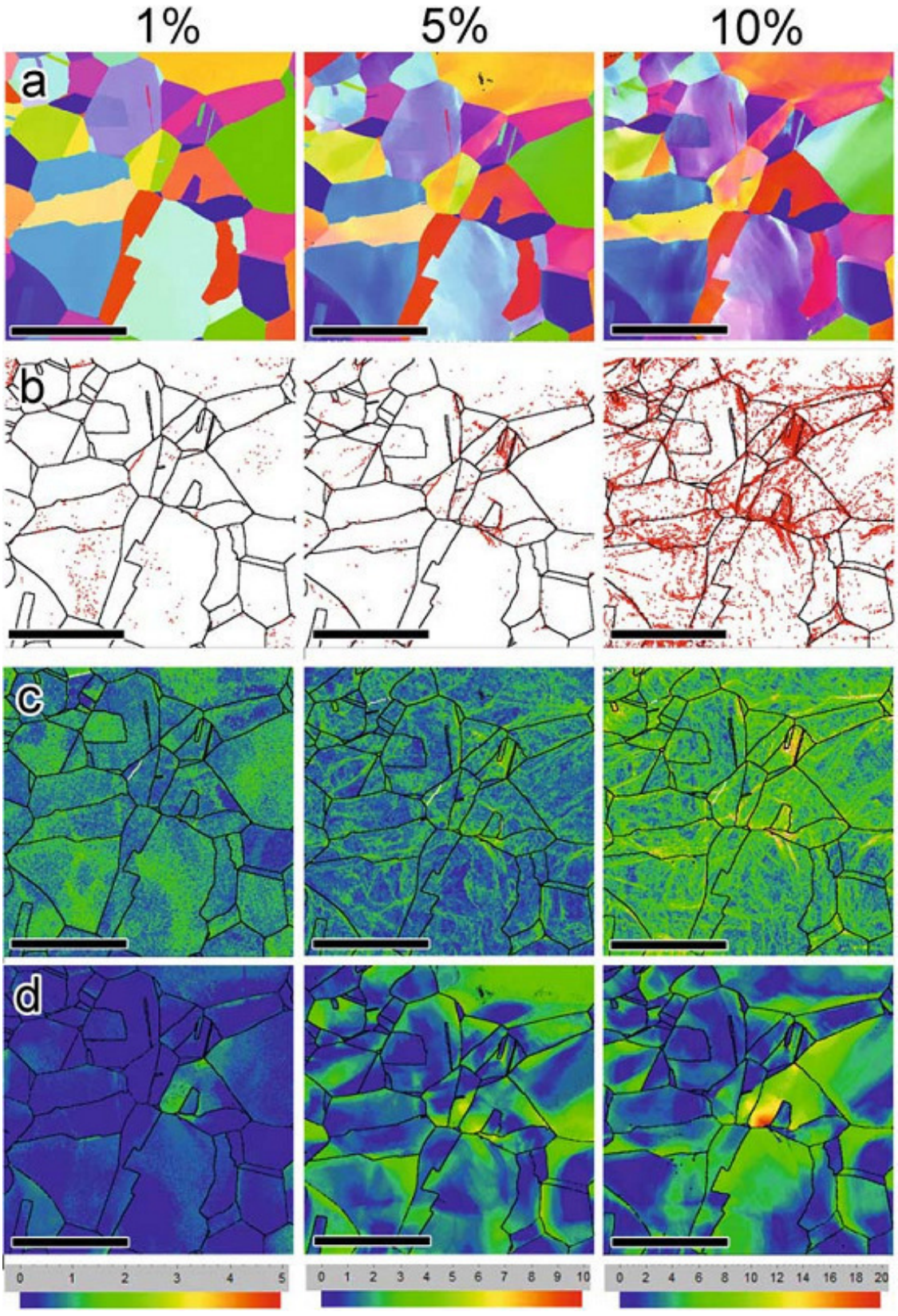

Figure 2.8: Comparison of different imaging techniques (a) IPF, b) grain boundary map, c) average kernel misorientation map, d) integrated misorientation map) based on the same field of view for different degrees of deformation; image taken from (Brewer/Field/ Merriman, 2009).

(Humphreys, 2001; Wilkinson, 2001). Depending on the used analysis method, the deviation in the measured misorientation angles can be in the range of $\approx 0.01°$ (Wilkinson, 2001).

Furthermore, several factors influencing the result of misorientation measurements have to be considered regarding their influence on the measurement (such as material, sample preparation, SEM settings, EBSD detection settings, data processing, step size, grid pattern) (Kamaya, 2009b). Especially kernel based results are affected by the step-size. Even tough adaptations with the kernel ranging over the same kernel size may give similar but not necessarily identical results (Wright/Nowell/Field, 2011). Nevertheless, results obtained with the same step-size should be comparable with small variations in other parameters (Kamaya, 2011). Especially for grain related parameters (GAM, GOS, ROD), the grain tolerance angle also influences the results. The grain tolerance angle is the maximum misorientation between two neighbouring points belonging to the same grain by definition. An increase of this value also increases the maximum misorientation value for the investigated grains e.g. by GAM or GOS imaging techniques. If grains below a certain size are excluded from the calculation (GAM, GOS, ROD), the spread of the misorientation shifts to higher values since the smaller (recrystallized) grains typically include lower misorientations (Wright/Nowell/Field, 2011).

But as mentioned before, this value is not very reproducible for different step-sizes as shown by Kamaya (Kamaya, 2011) with respect to averaged misorientations over the whole scanned picture. Moreover, Kamaya et al. showed, that the crystal deformation (Kamaya/Wilkinson/Titchmarsh, 2005) is a good measure for local strain, detected by EBSD. One year later, the authors introduced the modified crystal deformation (MCD) parameter (see equation (2.31)) (Kamaya/Wilkinson/Titchmarsh, 2006; Kamaya, 2011) where the results are independent of measurement system related parameters (e.g. step size, beam current, focus). Nevertheless, these parameters are still affected by EBSD camera resolution, data processing, electron beam condition and focus. It is also recommended to use large acceleration voltages to improve the accuracy and to deteriorate the spatial resolution and thereby to reduce the standard deviation of the misorientation distribution (Kamaya/Wilkinson/Titchmarsh, 2006).

$$MCD = \exp\left[\frac{\sum_{k=1}^{N_g}(\sum_{i=1}^{n_k} ln(\beta_{(m_k,p_i)})}{\sum_{k=1}^{N_g} n_k}\right] \tag{2.31}$$

As shown in equation (2.31), MCD is calculated by $\beta_{(m_k,p_i)}$ as the misorientation between the central orientations of pixels m and i of grain k, n_k as the number of pixels in grain k (typically the data is filtered keeping only grains above a threshold of minimum pixels for the calculations (e.g. 10 pixels as used in (Kamaya, 2011; Kamaya/Wilkinson/Titchmarsh, 2006)) and N_g being the total number of grains under consideration.

As a final remark on the topic of plastic strain analysis with EBSD it has to be pointed

out that the misorientation is just representative for dislocation densities affecting a orientation change of the crystallographic structure - the so called geometrically necessary dislocations (GND). In addition to these dislocations, "statistically stored" dislocations (SSDs) exist in the material and could have been introduced by straining effects as well. Furthermore, these dislocations also significantly influence plasticity and are therefore not negligible (Alkorta/Martinez-Esnoala/Sevillano, 2006).

Geometrically necessary dislocations (GND) As mentioned before, the plastic deformation causes a change in the orientation of the crystal structure by inducing dislocations in the material. Since the crystal structure is a specifically ordered system, the change of orientation in the crystal come along with a specific set of GNDs (Nye, 1953; Ashby, 1970). Since the EBSD data precisely maps the change of orientation between two points, the GND density can be calculated respectively (El-Dasher/Adams/a.D Rollett, 2003; Calcagnotto et al., 2010). Two approaches for calculating the GND density are shown and compared by Calcagnotto et al. (Calcagnotto et al., 2010): The strain gradient based method by Kubin and Mortensen (Kubin/Mortensen, 2003) and the full dislocation density tensor related method by (Pantleon, 2008; Demir et al., 2009) as well for dislocation densities in cases of high-angle rotational incompatibility (Beausir/Fressengeas, 2013). The work by Calcagnotto showed, that the approach by Kubin and Mortensen (Kubin/Mortensen, 2003) generates similar results as the tensor based methods and both are appropriate for calculating GND densities (ρ_{gnd}). The strain gradient based method uses the relation of the triple KAM misorientation angle versus the Burgers vector b, the step size a and kernel size (neighborhood) n (Konijnenberg/Zaefferer/Raabe, 2015):

$$\rho_{gnd} = \frac{3KAM}{|b| \cdot a \cdot n} \tag{2.32}$$

To exclude effects from (small angle) grain boundaries, pixels over a threshold (typically 2°) will not be considered since they should belong to different subgrains and therfore, the orientation difference is no more intra-granular.

Furthermore, it is recommended to adapt the misorientation threshold to the phase, which is analyzed since they e.g. got higher misorientations in martensite than in ferrite (with 200 nm step-size). Moreover, it has to be kept in mind that the pixel generated by the EBSD data is acquired by a SEM spot which is not a circular but an ellipsoid and therefore, the information might be gathered from different densities on different orientation axes (Kamaya, 2011). The SSDs density is not quantifiable by means of misorientations but an impression of the density might be taken from the pattern quality imaging of the sample (Wright/Nowell/Field, 2011).

Filtering Due to pseudosymmetry in diffraction patterns, pixels might not be indexed correctly and showing very different orientations in comparison to the neighbouring pixels. Furthermore, pixels in areas of high deformation, close to grain boundaries or without a matching pattern recognition could be without index. Incorrectly indexed pixels and pixels without indexing can be fixed during a clean-up process. During this process, these pixels will get the orientation of neighbouring pixels (Randle, 2009). The clean-up could additionally influence measured material parameter such as grain size (Mingard et al., 2009). Humpreys et al. (Humphreys/Bate/Hurley, 2001) and Kamaya (Kamaya, 2010) proposed orientation averaging as well as smoothing filter for EBSD and misorientation based strain measurements. It is shown, that the distribution of local misorientation is more smooth and thus clear as unfiltered imaging. The quantitative value is improved by reducing the average error of local misorientation from approximately 0.15° to less than 0.05° (Kamaya, 2010), respectively.

2.4.4 EBSD in materials science and tribology

Thermodynamics and their impact on microstructure Not all phases can neither be characterized by optical microscopy nor SEM (incl. EDS) due to their similar appearance in both imaging techniques. The separation between bainite and ferrite is hard to perform due to the same chemical contents as well as the same (bcc) structure. Even a separation by Kikuchi pattern comparison is not appropriate. One major difference between their phases is the GND density. De Meyer et al. (Meyer/Kestens/Cooman, 2001) and Petrov et al. (Petrov et al., 2007) have therefore used the pattern quality for a clear separation between the two phases. Later (Zaefferer/Romano/Friedel, 2008) developed a new method, which is based on the KAM gradients which occurring during the bainitic transformation. The results by Zaefferer et al. showed no good separation by pattern quality since it varies too much by secondary effects (surface inclination, focussing conditions). Even though the lateral resolution of EBSD techniques is limited to the spot size, effects with their origin in smaller structures might be investigated. Takahashi et al. (Takahashi/Ponge/Raabe, 2007) have used the EBSD analysis for a better understanding of the inner structure of pearlite and the impact on its mechanical properties. Because of its small lamellae width, cementite lamellae in pearlite cannot be analyzed directly. The work showed, that the zones with higher orientation gradients (especially long range orientation gradients) can be rather found in the pearlitic regions than in the proeutectoid ferrite grains. Orientation changes in pearlite grains reached up to 15° over several micrometer in the same pearlite grain. Moreover, in the regions of high orientation changes, the GND density is expected to be raised by dislocations occurring during the growth of pearlite while the phase transformation takes place. Besides the characterization of the present phase, EBSD might also be used for classification of parent grains of a for-

mer phase. The reconstruction of austenitic grains in martensitic steels are satisfactorily performed (Cayron/Artaud/Briottet, 2006).

Fatigue Plastic deformation is known as the pre-stage of crack initiation and thus, part of the chain of fatigue damage (Suresh, 1998) and is therefore also of interest for investigations by EBSD (Kamaya/Wilkinson/Titchmarsh, 2006; Kamaya, 2009a; Kamaya/Kuroda, 2011). Kamaya and Kuroda quantified the fatigue damage by EBSD measurements. In their work they show a difference of the inclination in the relation between the average misorientation and the MCD for single tensile or cyclic tensile loading. Thus, the EBSD data give information about the stress life of the sample. Furthermore, the stress amplitude and the number of cycles for cyclic tests can also be estimated by the information gained from the average misorientation. Moreover, the regions of higher misorientation in fatigued samples are found rather in clusters while in tensile samples these regions are found more frequently at grain boundaries (Kamaya, 2009a; Kamaya/Kuroda, 2011).

Thermal effects Besides plasticity, the method is also appropriate to investigate thermal effects and their damaging to the material. Kumar and Pollock (Kumar/Pollock, 2011) investigated the damage introduced by a single laser shot in nickel. They used the lattice misorientation to calculate the density of GND for quantifying the depth of the laser induced damage. The results of their work demonstrated, that the material is not affected by laser shots with less than 2 J/cm^2. Moreover, using higher energies, the depth of the affected zone behaved linearly with the laser fluence.

Tribology It is obvious, to use the information from EBSD for a quantitative analysis of the microstructure underneath a wear track since materials subjected to stresses in frictional contacts undergo plastic deformation. Large plastic strains and large rotation angles in generated subsurface cells were achieved after a short duration of sliding (Prasad et al., 2006). Furthermore, a principal rotation axis was determined in copper, which is the transversal axis to the sliding direction and parallel to the sliding interface (Heilmann et al., 1983a). Further tests especially of grain development in originally single crystal samples are also correlated with load and friction measurements. For analysis of small wear tracks with mandatory thorough sample preparation, EBSD measurements at cross-sections are possible by FIB cutting (Prasad et al., 2006; Prasad/Michael/Christenson, 2003). Depending on the quality of the wear track, EBSD analysis is not only possible on cross-sections but also directly at the surface and in the wear track as shown for instance in wear tracks at WC/Co hardmetal surfaces (Mingard/Gee, 2007; Gee/Mingard/Roebuck, 2009). The studies have shown the build-up of plastic strain in the grains until a critical value followed by cracking, fragmentation or removal of grains.

Additionally to elevated misorientation (KAM) and reduced pattern quality, slip planes were found by high-resolution SEM pictures in the areas of plastic deformation. Similar effects can be identified in metals. Prasad et al. (Prasad/Michael/Christenson, 2003) analyzed the deformed zone underneath sliding wear tracks in LIGA (German acronym for Lithographie, Galvanoformung and Abformung). The investigations showed bending of grain columns in the sliding direction with following breakdown of columnar grains with equiaxed formation of a fine grain structure and additional formation of low-angle grain boundaries (Prasad/Michael/Christenson, 2003; Prasad et al., 2006). The plastic deformation and the orientation changes around a hard particle underneath a warm rolled Fe4Al alloy was performed by Konrad et al. (Konrad/Zaefferer/Raabe, 2006) using 3D techniques. Even tough the Laves-phase particle was destroyed during the FIB milling and no EBSD analysis was possible on it, they found steep orientation gradients neighboured with newly formed recovered sub-grains at both sides in transversal direction of the inclusion. Roberts et al. used misorientation values to further understand the deformation in rail steels (Roberts et al., 2013). A railway was examined after service concerning strains by KAM and correlated with results by modelling the plastic deformation. The work revealed that a filtering of the experimental data is required near the rail surface. An increase from 3° average KAM misorientation to 10° was found in the deformed region. By modelling, the changes to pearlite colony shape due to macroscopic shear were considered and confirmed the KAM value increase. Furthermore, the authors showed that the model validates the experimental KAM values, even though the measured values were higher than the modelled ones.

2.4.5 Focused ion beam preparation

Beside the use of focused electrons for materials' analysis, focused ion beams (FIB) may be used for crafting sample surfaces[1] (Phaneuf, 1999; Giannuzzi/Stevie, 1999; Munroe, 2009). However, the ion-beam-surface interaction might become a problem when conducting FIB milling. Several issues were recorded and investigated in the past (Giannuzzi/Stevie, 1999):

- selective sputtering by inhomogeneous sample materials
- damaging by impacting gallium ions
- formation of amorphous layers at the milled surface
- curtaining effects by loss of focus or too large step-sizes or pores/cracks in the sample

Nevertheless, due to its advantages FIB became some kind of "Swiss Army Knife" for material science (Munroe, 2009).

[1] beside the ability to use a FIB as an imaging method, too

2.4.6 Transmission electron microscopy

For imaging structures below the resolution of SEM, the focused electron beam is used in transmission. Thus, reducing the penetrated volume and thereby increasing the resolution. The method is called transmission electron microscopy (TEM). The resolution of this method is able to contrast objects in the range below 50 pm (Sawada et al., 2015). Beside conventional techniques like bright- and dark field imaging, the diffraction of the electrons in crystalline structures can also be used for an information about the crystallographic configuration of specific sample regions.

Another important feature of TEM is the ability to make an estimation about the dislocation density in representative sample regions. Therefore, a defined sample region is examined and the amount of dislocations in this region is counted manually. The relation of the counted dislocations to the examined volume results in the dislocation density. However, the relationship of such local measured values and larger regions is not always valid.

Apart from the analysis itself, the sample preparation is one very important element of a successful TEM measurement. Usually, one chooses between two common methods (Rao/Muraleedharan/Humphreys, 2010):

1. Sandwich preparation (Walzhofer et al., 2014): The sample is cut in very thin slices. The edges, which contain material of interest are "glued" together (sandwich). The gap between the samples is milled by ion milling to further thinning the edges until the edge thickness is thin enough for a transmission of electrons (usually less than 200 nm). The advantage of this method is its rather conventional procedure and the ability to investigate a larger region along the edge of the milled hole. Thus, sample regions of different distances to the edge (usually the former sample surface) can be observed in one preparation. In contrast, the region of interest has to be at least prepared towards becoming the edge material. Additionally, grains of different phases in the material usually show a different response to the milling with a resulting inhomogeneous thickness of the milled sample.

2. Lift-off technique (Giannuzzi/Stevie, 1999): one other very common technique is preparing the lamella by a combination of SEM and FIB. Thereby, the lamella is milled out of the surface region by focused Ga ions, while the procedure is parallely observed by SEM. In general, the lamella is prepared normal towards the surface. However, a parallel preparation is also possible as shown by (Lozano-Perez, 2008). The disadvantage is the necessity to access equipment, much more expensive than necessary for sandwich preparation as well as a limited lamella size of several micrometer edge length (e.g. 10 µm x 15 µm). The advantages of the method are a homogeneous sample thickness as well as the ability to define a specific sample region as the resulting lamella. Also a comparison between FIB milled cross-sections

and conventionally mechanically polished surfaces showed similar pattern qualities (Konrad/Zaefferer/Raabe, 2006).

Chapter 3

Experimental

To answer the given questions related to tribomutation, a set of samples has to be prepared, tribologically tested as well as analyzed in a specific way. This chapter describes the specific configuration of the investigated material and its preparation for the specific test configuration. A description of the tribological testing configurations is also necessary and therefore the test rigs and the setup parameters are also given in this chapter. The chapter is concluded with the explanation of the used characterization methodology as well as the related sample preparation for each analysis method. The sliding tests will serve for answering the rather fundamental questions. For the investigation of a wheel-rail contact, a lab-scale test-rig was used. Thereby, the contact situation is simulated under controlled lab conditions.

3.1 Studied materials

The investigated materials are choosen according to the specific tribological testing. Sliding tests were performed on disc-shaped samples which are best machined out of extruded rods while the rail-wheel tests were performed on real materials from this specific application. All the sample materials have a ferritic/pearlitic microstructure.

3.1.1 Sample material for sliding tests

The investigated material is steel of type 42CrMo4 (1.7225 or AISI 4137 according to datasheet by Deutsche Edelstahlwerke GmbH). The chemical composition of the steel is shown in table 3.1. The raw material was delivered in pieces of extruded and hardened rods (diameters of 40 mm and 100 mm). Sample preparation started by cutting of the rods into disks with following double side face grinding to a final thickness of 10 mm. The samples where then austenitized at 850°C for 1 h. Later the samples were cooled at room temperature. Thus, the steel converts into a ferritic/pearlitic microstructure (Liedtke, 2005). See figure 3.1 for a metallography of the obtained microstructure.

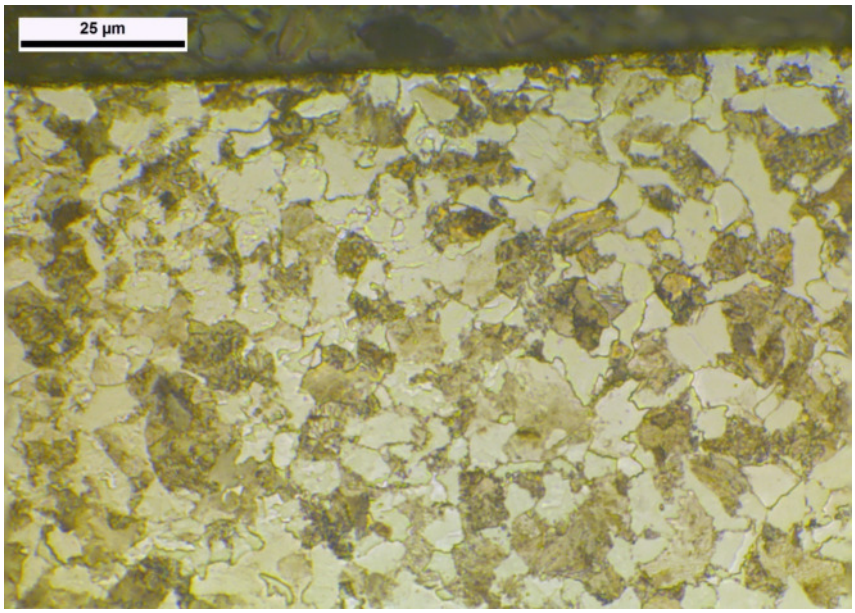

Figure 3.1: Light microscopy image of 42CrMo4 showing the pearlitic (dark) / ferritic (bright) microstructure.

Table 3.1: Chemical contents of 42CrMo4 steels according to data sheet by Saarstahl

C	Si	Mn	Cr	Mo	S
0.42 %	0.25 %	0.75 %	1.10 %	0.22 %	<0.035 %

While the elastic properties (E=202 GPa and ν=0.3 (Nygårds/Gudmundson, 2002)) are independent of the content distribution of pearlite and ferrite, the plastic behaviour is a function of the pearlite content in the steel. Tests of pure ferrite and pure pearlite (1 % pearlite and 99 % pearlite) show a yield strength of ≈ 250 MPa for ferrite (10 µm average grain size) and ≈ 750 MPa for pearlite (Nygårds/Gudmundson, 2002). The mechanical properties of 42CrMo4 steel in stress-relieved condition is determined by Lee and Uhlig (Lee/Uhlig, 1972) as a yield strength of 662 MPa and a tensile stress of 793 MPa. The insignificant influence of minor phases e.g. manganese sulfides on the mechanical properties is discussed elsewhere (Cyril/Fatemi/Cryderman, 2009). Since the pearlite grains consist of ferrite and cementite lamellae, the mechanical properties of single grains themselves are anisotropic. Nevertheless, due to the normalizing process of the steel, no predominant direction of the lamellae growth is expected and thus, macroscopic isotropic mechanical properties. Roughness measurements by confocal profilometry (Nanofocus, μ-surf, 50x) revealed a surface roughness (ISO 4287) of R_q=0.53 (±0.05) µm.

3.1.2 Sample material for wheel-rail testing

For applying the wheel-rail conditions on lab-scale, the R260 steel was used for both, wheel and rail. The wheel diameter was set to 50 mm and a contact curvature of 16 mm,

respectively. However, not the original running surface was used but instead, a flank region with a curvature fitting the scale of the test-rig was used. The rail was cut to smaller dimensions (250 mm length and 40 mm width) in order to fit into the test rig. The pearlitic rail R260 steel exhibits a yield strength of ≈ 590 MPa and a tensile strength of ≈ 980 MPa with a hardness of around 280 HB30. During manufacturing procedure, the rail is rolled at high temperatures to the final shape followed by cooling to room temperature at ambient conditions, which results in a decarburization zone with a pronounced ferritic content near the surface (figure 3.2 shows the surface region of a decarburized rail material as delivered).

Besides, another set of rails was tested with an additional surface finishing milling step removing the surface decarburized zone (figure 3.2) and thus resulting in a smoother surface topography and pure pearlitic microstructure. The experimental studies aim to compare rail material grades as they are used in real application without any adaption to lab tests. Therefore, the surface finish was unmodified within a reasonable effort without polishing. Moreover, the surface of the as delivered sample was still covered with an oxide scale and so the rail surface featured a roughness of R_q=2.43 µm for the as delivered condition and a roughness of R_q=0.54 µm for the surface finished condition.

3.2 Tribological testing

For applying tribomechanic stresses a sliding point contact was chosen on lab scale experiments. The contact geometry is well known and understood and therefore provides good conditions for further analysis on material changes. Tests are performed in oscillating translation as well as rotational mode. Therefore, the altering stress direction can be set in comparison to an cumulative stress direction.

As a comparison, similar material is tested under more application related conditions. Therefore, a test rig was used, which simulates the rolling contact mechanics of a train wheel running on a railway. The geometries are scaled down to a smaller but related to the sliding tests a similar scale.

3.2.1 Sliding tests

For the sliding tests, a ball on disk configuration was used (see figure 3.3). In the following tests, the sample is always the disk material. The test rig allows to perform tests in rotational mode, where the disk is turned underneath the counterpart (ball) as well as in oscillating mode, where the counterpart is moved back and forth in a linear translation. Cemented carbide (94 % tungsten carbide and 6 % Co) was used as counterpart material. The ball diameter measures 10 mm. The counterpart material's hardness (1550 HV), Young's modulus (610 GPa) and compressive strength (5.3 GPa at 25 °C) are provided

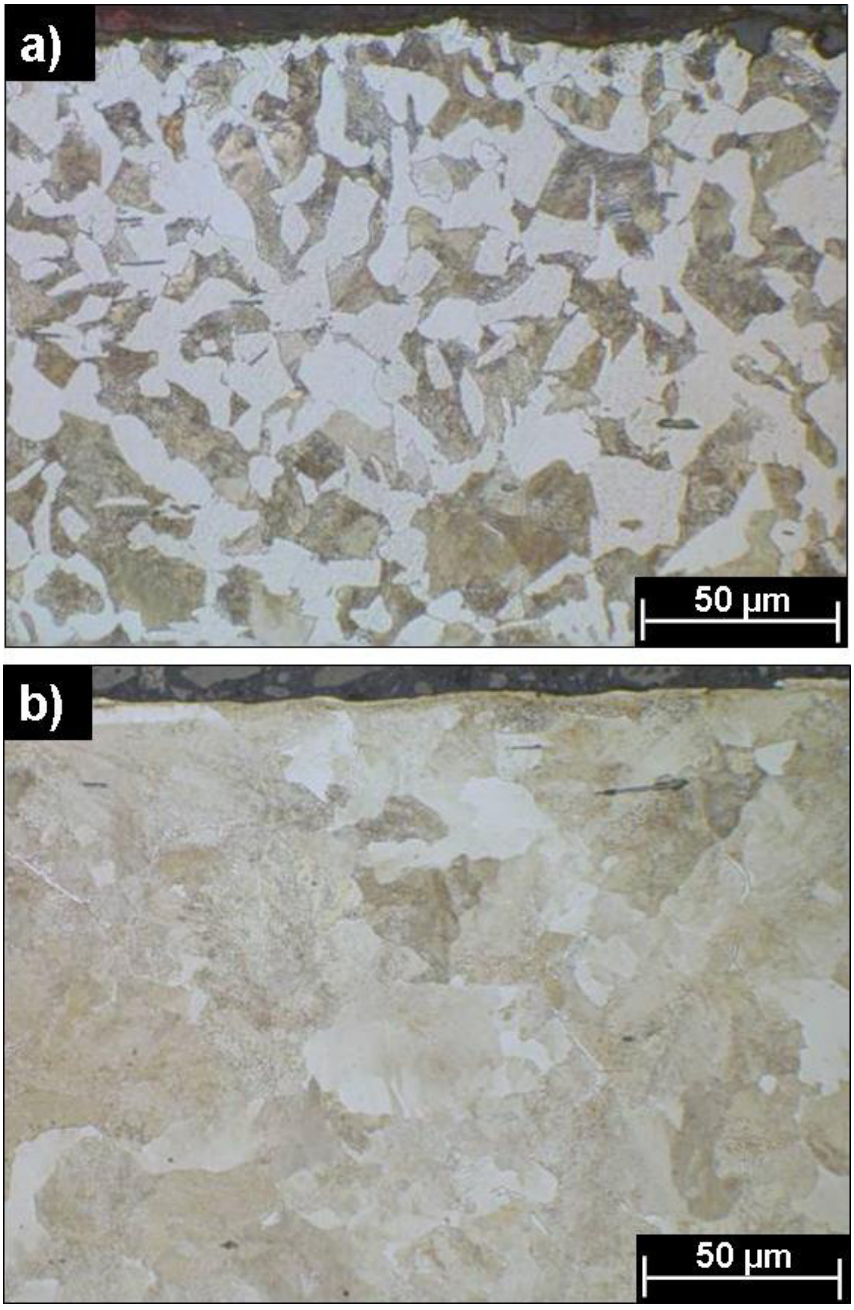

Figure 3.2: Optical microscopy of R260 steel microstructure close to the surface: (a) as delivered in original condition as delivered (AD) and (b) surface finished (SF).

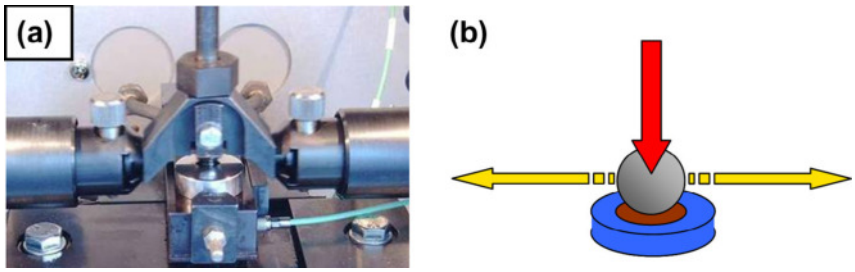

Figure 3.3: a) Test rig for sliding testing in oscillation configuration and b) schematic drawing of the test configuration.

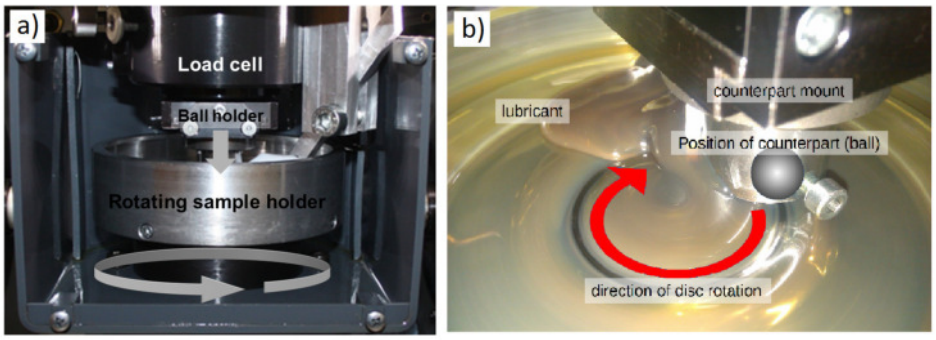

Figure 3.4: a) test rig for sliding testing in rotation configuration; image taken from (Linz et al., 2017), b) view inside the rotating sample holder during sliding testing also showing the flow control of the lubricant back into the contact region by the plough (hidden behind the counterpart mount).

by the supplier. The specific testing device is known as linear oscillation test rig (SRV)[1].

The machine is capable of applying normal loads up to 500 N. For the tests, loads of 20 N, 120 N and 420 N were used. The resulting maximum Hertzian contact pressure is 1.66 GPa for 20 N, as well as 3.02 GPa for 120 N. The corresponding depth of the maximum Hertzian contact pressure is 36 µm for 20 N and 66 µm for 120 N. For the oscillation tests a normal load of 100 N was applied. The maximum oscillation frequency depends on the stroke. The cyclic translation profile is shown in figure 3.5. But for rotational mode, the maximum speed is limited to 2 000 rpm. However, the rotation speed was varied to have a similar contact speed (0.2 m/s) of the ball on the disk. Investigations of oscillation test, where concentrated on the middle of the halves of the wear track since the middle of the whole wear track is plastically pre-deformed by applying the load before the tribo-testing. Also for rotational tests, the start position was marked to avoid analysis of a pre-deformed zone. For performing lubricated tests in oscillation mode, the lubricant is applied to the surface with a pipette. In rotational mode, the disk is submerged in a bath inside a tray. For highly viscous lubricants, a plough is mounted on the wear track for forcing the lubricant back onto the wear track (see figure 3.4). Since the device would heat up due to the running electronics and mechanics as well as a lacking cooling

[1]DIN-51834, ASTM-5706

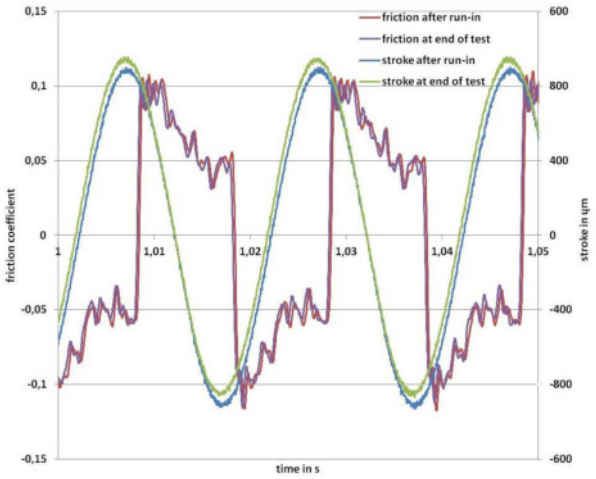

Figure 3.5: Comparison of friction coefficient and stroke after run-in (100 cycles) and at the end of the test (10^5 cycles).

Table 3.2: Viscosity of FVA reference oils for 50 °C according to manufacturer's data sheet

reference oil	viscosity
FVA1	11 mm^2/s
FVA4	260 mm^2/s

function of the test chamber, the sample is pre-heated to 50 °C in a controlled way. Tests had been stopped after the desired number of cycles for post-mortem analysis. A continuation of a previous test after disassembling is not possible due to inaccuracies of the positioning. Since the work concentrates on the plastic deformation, abrasive wear would be disadvantageous since the plastic deformed material would be ground of and thus, the relation of the distance to the original surface would be lost. For prevention of abrasive wear, a lubricant with high viscosity (reference oil FVA4) was chosen for the tests. As a comparison, tests with a lower viscous oil are performed, respectively. The viscosity behaviour of the selected FVA reference oils are shown in table 3.2.

3.2.2 Wheel-rail tests

Following the principle requirements of simplified tribotests of the wheel-rail contact, the investigation was done on a part of a real rail because the damage or the damaging process, respectively, on the rail is the primary focus of investigation. The tribometer was described in detail in a previous work (Trausmuth et al., 2014). The repeated unidirectional movement of the test sample in the tribometer reproduces the wheel-rail contact. The testing parameters used in this study are summarized in table 3.3.

Table 3.3: Summary of testing parameter used in lab-scale wheel-rail test rig.

rail material	R260 as delivered R260 surface finished
wheel material	R260 machined
lubrication in contact	technically dry
normal load	4 000 N
velocity	0.15 m/s
rolling distance / cycle	215 mm
test cycles	0, 100 and 4 000

3.3 Analysis

Due to the different tribological testing procedures and the related parameters and sample geometries, the analysis was adapted to each configuration. Therefore, the specific parameters for characterization and the necessary sample preparation are given in this section.

3.3.1 EBSD sample preparation and analysis

Cross-sections were cut and prepared following the recommendations for EBSD sample preparation by Struers A/S (Struers, 2009). Since variations in preparation and analysis parameters can have a significant influence on the misorientation measurements, the preparation was done using an automated grinding/polishing machine and the parameters were kept constant. EBSD measurements were performed using a field emission gun in a FIB/SEM workstation (FEI Helios NanoLab 600) equipped with an EDAX Hikari EBSD camera. The acceleration voltage was set to 20 kV with an electron current of 22 nA. Since the small cementite lamellae are too thin to be detected using EBSD (Takahashi/ Ponge/Raabe, 2007), the scanning parameters were optimized for the ferrite grains and crystallographic orientation mapping was carried out with a step size of 100 nm. For the sake of comparison, all EBSD analyses were done with the same hardware setup, using the same scanning parameters (e.g. acceleration voltage, working distance, beam current) and the same EBSD analyses settings (e.g. camera resolution) (Randle, 2009).

The EBSD data was analyzed using standard tools for EBSD (Orientation Imaging Microscopy (OIM™) Data Analysis by EDAX Inc.) data processing. The orientation threshold for HAGBs was set to angles greater than 15°. For the EBSD plots, LAGBs were divided into two groups for a better visualization: the first one ranges from 2° to 5° (rather close to misorientations) and the second one from 5° to 15° (closer to the formation of HAGBs). Moreover, pattern quality images were taken to distinguish between ferrite and

pearlite grains. The grain file was extracted, containing a list of all grains, segmented as stated above, and their characteristics, such as average pattern quality, average confidence index and grain size.

From several methods available to calculate misorientations for an EBSD data set, kernel average misorientation (KAM) was chosen. A KAM value is generated for each single EBSD data point, serving as the center of the kernel for the related misorientation. The resulting KAM values can be affected by the range (order) of the neighbourhood and whether all or only perimeter data points are considered. As a data-point-based method, KAM plots intragranular misorientations but the mapping is highly sensitive to localized misorientation gradients. Thus, low constant orientation gradients are hard to visualize. A steady variation in misorientation over an entire grain would only be shown as a slightly increased KAM value in the mapping.

The work of Calcagnotto et al. (Calcagnotto et al., 2010) and Konijnenberg et al. (Konijnenberg/Zaefferer/Raabe, 2015) showed a linear relationship between the misorientation angle and, both, the KAM values and the GND density (ρ_{GND}) for screw dislocations (equation 2.32). Thus, 2D KAM plots allow for the visualization of localized misorientation as well as GND densities whereas 1D plots of average GND densities provide quantitative and statistical information. A limitation is that statistically stored dislocation (SSD) densities are not measureable by EBSD as reported by Shigesato and Rauch (Shigesato/Rauch, 2007). As in (Calcagnotto et al., 2010), a step size of 100 nm and the 2nd order neighbourhood was used. As recommended by (Calcagnotto et al., 2010), values larger than 2° are not considered for the calculation since they represent LAGBs or even HAGBs and are quantified in separate analyses. Similar to the work of Calcagnotto et al. (Calcagnotto et al., 2010) only the main slip directions are considered for simplicity: Ferrite is a bcc lattice structure of iron and only its main slip planes in {110} and main slip directions in <111> are taken into account, resulting in 12 main slip systems. With a lattice spacing a in ferrite of 0.28665 nm, according to the ICDD/PDF-4 2012 database from the International Centre for Diffraction Data (2013), the length of the Burgers vector with the highest probability in ferrite (a/2 [111]) (Hornbogen, 2012) is 0,24825 nm.

3.3.2 TEM sample preparation and analysis

For validation of the EBSD results, three lamellae were selected for TEM investigations (see figure 3.7). Lamella c was prepared out of the bulk material serving as a reference sample. The two other lamellae were prepared out of cross-sections previously scanned using EBSD for a better selection of the area of interest (lamella a perpendicular to the cross-section and lamella having a slightly shallow angle (10°) to the tribologically tested surface). TEM is a well-established technique for structural characterization of metals

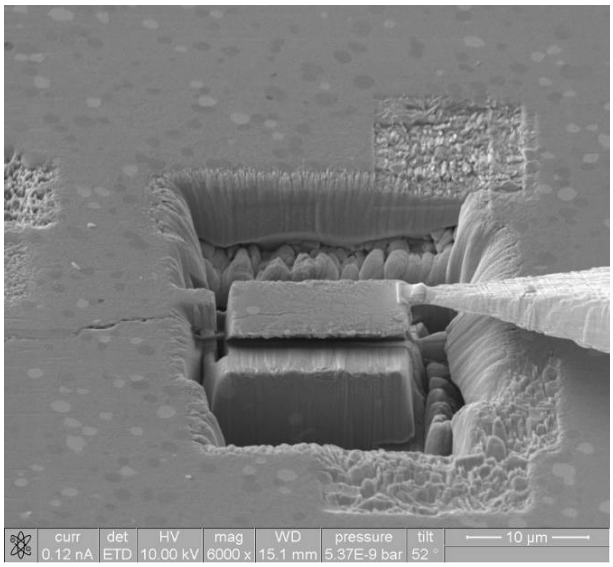

Figure 3.6: Progress of TEM lamella preparation, parallel to the cross-section surface. Here shown for a HSS steel (Linz et al., 2018).

with high spatial resolution. Information can be obtained either in TEM mode or by scanning a fine electron probe across the sample and collecting the signal of diffracted or undiffracted electrons in scanning transmission mode (STEM).

Transmission Kikuchi Diffraction (TKD) was applied to the cross-section lamella (a) in a scanning electron microscope (SEM) equipped with an EBSD camera. Electrons that are scattered on their path through the sample get diffracted at lattice planes close to the exit surface, form a Kikuchi pattern on a phosphorous screen and are imaged by the EBSD camera. TKD samples do not require a large 70° angle sample tilt, as typical in standard EBSD. This enables orientation maps with higher spatial resolution (Trimby, 2012; Trimby et al., 2014). The lamella position was selected based on the results of EBSD images, taken previously of the same cross-section. The lamella orientation was chosen to be parallel and with minor milling from the original cross-section (see figure 3.6). The microstructural features of the lamella were characterized by a FEI Tecnai F20 analytical field emission TEM equipped with a high angle annular dark field detector (HAADF) for STEM investigations. TKD was performed by a FEI Quanta 200 field emission SEM equipped with an EDAX DigiView III camera, operated at 25 kV. The sample was tilted by 5° and located at a small working distance of 5 mm. Electron transparent lamellae for TEM and TKD investigations were produced by a FEI Quanta 200 3D dual beam focused ion beam facility.

3.3.3 Separation of ferritic-pearlitic phases using EBSD

The separation between the two phases was performed using the pattern quality or the confidence index (CI) of the individual grains. Hereby, the cementite lamellae are expected

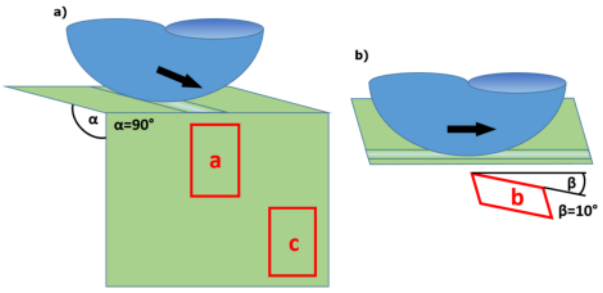

Figure 3.7: Schematic drawing showing the regions and orientations of TEM lamellae extraction.

to distort the lattice parameters and reduce either the confidence index or the pattern quality (Peranio et al., 2010; Iza-Mendia/Gutiérrez, 2013).

For a quantitative comparison of the EBSD plots, masks were generated to hide either the ferrite or the pearlite grains. It is thus possible to filter the image according to one of the present phases in order to visualize separately the individual contributions to microstructure deformation for a specific crystallographic structure.

To do so, the light microscopy cross-sections were overetched for higher contrast between the darker pearlite and the smooth and bright ferrite grains (as visualized by optical microscopy). The picture was set to gray scale, the shading removed, and segmented into darker pearlite regions, turning to pure black, and brighter ferrite regions, becoming pure white. Since the segmentation is not perfect, subsequent dilatation and erosion were performed on the segmented image. This is necessary, since there are small bright ferritic regions inside pearlite grains and dark spots in the bright ferrite grains due to sample preparation artifacts. Detailed values for each step of the process are not mentioned here, since those depend on the individual etching configuration, microscopic set-up as well as camera preferences and settings. The masks were then generated by making either the black or white transparent, overlaying the EBSD visualizations.

A similar technique was performed on the basis of TEM images. However, here the masking was done manually based on the appearance of the cementite lamellae that can be easily recognized in the TEM image. The masked pearlite regions where then set as an overlay on the EBSD plots of the same region. However, the milling process undergone by the lamella for the TEM preparation needs to be taken into consideration (from the surface, up to about 100 nm were removed).

3.3.4 Mechanical properties

Hardness measurements were performed using an FM-700 device[2] in order to correlate the microstructure with the mechanical properties. The evolution of hardness in the stressed region versus the number of cycles was measured at 30 µm distance from the surface. Since

[2]FUTURE-TECH CORP, Kawasaki, Japan

this is insufficient for valid hardness measurements in the cross-section, due to proximity to the edge, a plane parallel to the tribo-surface was indented. This means that the surface containing the wear tracks was ground and polished down to 30 µm where the hardness measurements were performed from the top surface. Additionally, the hardness versus the distance to surface (wear track) in a transversal cross-section was plotted for a sample with 10^5 cycles. For a comparison of the constituent phases of the materials concerning their participation on plastic deformation and straining, stress/strain curves were calculated according to Allain and Bouaziz (Allain/Bouaziz, 2008). Allain and Bouaziz calculated the stress-strain relationship for ferrite as a function of its grain size d:

$$\sigma_{ferrite}(\varepsilon_{ferrite}) = \sigma_0^{ferrite} + \frac{\alpha M \mu \sqrt{b}}{\sqrt{d}} \sqrt{\frac{1 - exp(-f M \varepsilon_{ferrite})}{f}} \tag{3.1}$$

with $\sigma_0^{ferrite}$ as the lattice friction depending temperature and the chemical composition. α as a constant describes the order of unity, M the mean Taylor factor, µ the shear modulus of the ferrite, the Burgers vector b for a perfect dislocation and an adjustable parameter for the relation of the intensity of dynamic recovery processes. In contrast, the stress-strain relationship for pearlite is calculated based on the interlamellar spacing s:

$$\sigma_{pearlite}(\epsilon_{pearlite}) = \sigma_0^{pearlite} + \frac{M \mu b}{s} + \frac{K}{g}(1 - exp\frac{-g\epsilon_{pearlite}}{2} \tag{3.2}$$

with $\sigma_0^{pearlite}$ beeing the critical stresss due to the lattice friction in the ferrite lamella in pearlite and K and g are two empirical constants.

3.3.5 XRD measurements

The residual stresses where measured by using the $\sin^2\psi$ method (Hauk, 1997) for different angles (ψ) with respect to the surface normal. For each wear track, the measurement was performed in two different directions, being normal towards each other (φ=0° and φ=90°): parallel to the sliding direction (S1, φ=0°) and perpendicular to the sliding direction (S2, φ=90°). The measurements were performed using an Incoatec microfocus X-ray tube and a Cu anode on a Bruker (AXS) GADDS instrument. For reaching an almost parallel beam geometry, a Montel mirror providing Cu($K_{\alpha 1/2}$) radiation was used. Depending on ψ, the penetration depth of the X-rays varies between 4.2 and 1.9 µm (suggesting 95 % absorption). The given values are thus averaged values of this depth range. Due to the topography of the wear track and its limited width, the X-ray beam size was restricted to 300 µm. Additionally, a 2D Vantec 2000 detector was used for collecting the diffracted beams. The distance sample to detector was set to 23 mm.

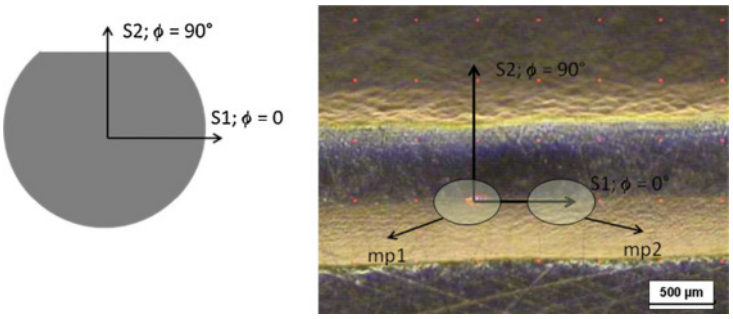

Figure 3.8: Schematic drawing of the sample shape with the orientation relations to the wear track. The two ellipses in the right picture mark the two measurements spots, also showing the relation of beam width to wear track width.

3.3.6 Definition of area of interest for wheel-rail testing by simulation of the contact situation

The geometry of the lab scale wheel-rail configuration provides a contact situation representing the real contact situation but the dimensions are reduced (Linz et al., 2015). The contact pressure in the middle of the sample is 760 MPa which is in the same range as stresses in the real system (Donzella et al., 2005). Simulations revealed that the elastic stresses reach a critical level in the region where cracks (head checks) are usually found during longer operation (Linz et al., 2015; Trausmuth et al., 2014). The highest von Mises stress without slip is found beneath the surface in a depth of ≈ 38 µm (Linz et al., 2015). For the current early-damage investigations these information were used to determine the most interesting position for EBSD analysis on longitudinal sections through this region.

3.3.7 Microstructural characterization

To characterize wear mechanisms, the worn surface was investigated by SEM. Moreover, etched (Nital 1 %) cross-sections were observed by SEM (ZEISS Supra 40VP) after a defined number of cycles. The investigation was performed on longitudinal sections in rolling direction in the region of highest plastic deformation determined by FEM simulations (Linz et al., 2015). For visualization of the crystallographic structure of the worn regions, EBSD was performed (FEI Helios 600). The preparation of the cross-section was done according to the guidelines for ferrous metals by STRUERS A/S (Struers, 2009). The scan covered a sample area of (200×200) µm and ranges from the loaded rail surface to a depth of 200 µm within the bulk. The scanning area was chosen to cover an appropriate region with an adequate resolution and significant amount of grains. Thus, a step-size of 200 nm was chosen to analyze sub-grain effects such as misorientation and LAGB quantification. The latter was necessary to establish a better visualization of sub-grain phenomena in the plots due to high plastic deformation at this stage. Since the cementite lamellae are too thin for an sufficient analysis by EBSD (Takahashi/Ponge/

Raabe, 2007), the scanning was performed on the ferrite phase only. A later separation between the ferrite grains and the pearlite grains by the pattern quality according to the work of Peranio et al. (Peranio et al., 2010) turned out to be not successful since the plastic deformation affects these parameters more than the presence of the cementite phase (Linz et al., 2014). For a quantitative investigation of the early-damage regime, plots of samples after 100 cycles were compared to the unloaded reference. For the purpose of comparison, the near surface zone was also investigated after 4 000 cycles in order to evaluate damage development.

For a quantification of the plastic deformation, LAGB density and misorientation deviation were analyzed. For the latter, the KAM was used. Thereby the orientation difference of the centre point of a kernel was compared either (i) to all the measured points in the kernel or (ii) to the points at the perimeter of the kernel with the size n (neighbourhood). For the data presented here, a kernel including all measured points of the 2nd neighbourhood showed best results for a good visualization of the local strain in the plots. Since the surface-line might not be clearly visible in the EBSD plots, regions not comprising of sample material were coloured in black.

3.3.8 Hardness measurements

The hardness of the material is usually measured by indenting a hard counterpart (ball vor Brinell-testing and a pyramid for Vickers-testing (Bargel/Schulze, 2008)) into the material. Nevertheless, the hardness value is a size dependent value (indentation size effect (Nino et al., 2010)). Typically, smaller indentation loads result in higher hardness values (Maharaj/Bhushan, 2014). Tests on polycrystalline copper by Chaudhri (Chaudhri, 1998) showed a depth range of the hardened material underneath a vickers indentation to be 1.5 times the range on the surface. While the distance from the middle of a vickers indentation to neighbouring indents should be 2.5 times the diameter (d) on the surface, the material should be ground $1.5 \times 2.5 \times d$ for reaching an adequate plane for new hardness measurements. For each measurement configuration, an optimal measurement load has to be determined first. For the hardness measurements, a set of ten measurements was performed for getting an idea of the standard deviation and thus the spread of the values. Figure 3.9 shows the mean standard deviation for each measurement load. Hereby, the measurement load should be as low as possible, since a lower load produces a lower indentation and therefore measurements closer to the cross-section edge (wear track surface) are possible. Based on figure 3.9 HV0.05 was chosen for an optimal measurement load since an increase to HV0.1 would not decrease the standard deviation significantly but the necessary distance to the sample edge would increase in a pronounced way.

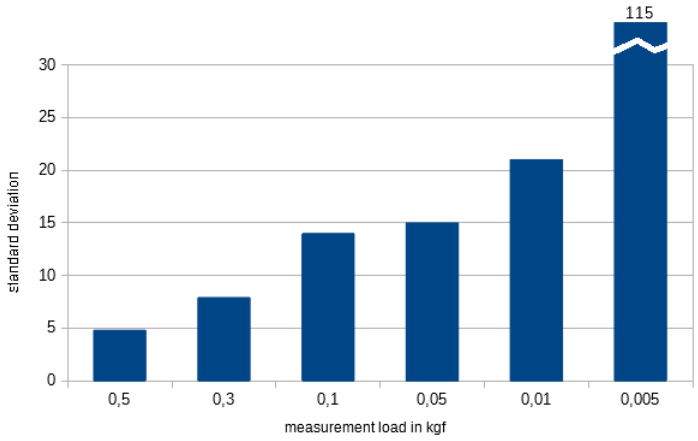

Figure 3.9: standard deviation for different measurement loads using vickers hardness indentations in ferritic/pearlitic steel.

Chapter 4

Results

The results are divided into the results by unidirectional sliding, bidirectional sliding and finally the wheel-rail tests as a rolling test configuration. The analysis of the unidirectional sliding tests will be the basis for a later discussion and shall basically answer to the questions of how the strain evolves in a sliding contact and the influence of the two present phases as well as the influence of the lubrication. One important aspect will be the relation between the strain measured by EBSD as well as the mechanical properties of each phase of the steel. Specific regions were investigated by TEM when a higher resolution was needed. A special emphasis is put on the question related to the mechanical behavior of the individual phases according to the strain incompatibilities. In this case, the higher resolution given by TEM is mandatory. As far as the wear mechanisms in bidirectional sliding are concerned, the samples were investigated according to their residual stresses since the strain evolution as a non-directional measure showed no sliding direction related differences. For the analysis of the wheel-rail contact, strain measurements are again the main method to understand the wear mechanisms. Moreover, the strain values will be linked to measured hardness values thus providing an idea for the degree of cold working due to the rolling mechanism.

4.1 Unidirectional Motion - Rotation

For the unidirectional sliding tests, a wide range of microscopic techniques was used. Special focus was put on a combination of information gained by different techniques. The combination was performed by overlapping images of optical microscopy, EBSD, TEM as well as TKD. Especially the separation between ferritic and pearlitic regions is challenging using orientation imaging techniques (EBSD, TKD) only. Therefore, this information is given by optical microscopy for EBSD as well as by TEM for a phase identification in the TKD plots. The phase identification is mandatory to obtain a qualitative separation between the phases and thus the strain evolution in the two different phases. The quantitative strain related parameters are compared with calculated von Mises stresses and

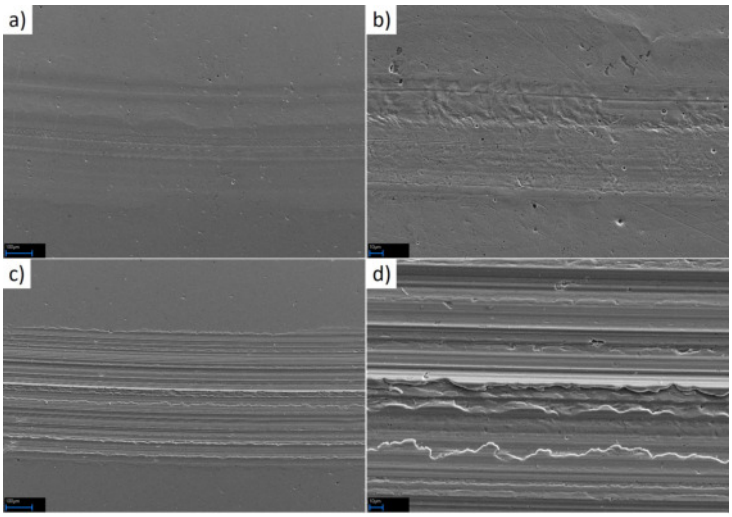

Figure 4.1: SEM imaging the surface topography of an unidirectional wear track (20 N normal load, FVA4 lubrication) a) after 200 cycles with b) showing the center of a) in higher magnification, and c) and d) after 200 000 cycles, respectively.

stress-strain curves calculated for the two present initial phases as well as for the grain refined ferrite thus allowing a deeper discussion of the mechanical influence of the present phases. Furthermore, the strain related parameters are compared for different normal loads and lubrication conditions. Therefore, a variety of different contact conditions was tested and serves as a basis for a lubrication and normal load related discussion of strain evolution. Figure 4.1 gives an impression of the resulting surface topography for the tested variety of contact conditions in unidirectional sliding.

4.1.1 Microstructure and strain evolution

One fundamental question of strain evolution in tribology is the strain evolution for higher numbers of cycles when the lubrication conditions prevent a loss of material. Such conditions are achieved for highly viscous lubricants and low sliding speeds. Therefore, the FVA4 lubricant. Because of that, no wear due to material loss occurred and the strained regions will undergo further strain evolution with increasing number of cycles. EBSD micrographs (figure 4.2 to 4.4) show microstructural evolution with increasing number of cycles. Up to and including 10^3 cycles, the grain morphology in the zone underneath the contact region does not show any remarkable difference compared to the bulk material (see figure 4.3 and 4.4). Beyond this point, the progressive formation of smaller grains is revealed at logarithmic intervals. The grain boundary plot (figure 4.3) at 10^4 cycles shows smaller grains in a zone comprising the sample surface down to approximately 70 μm. The EBSD plots (figure 4.3, 4.4) reveal an even higher density of small grains at 10^5 cycles. In figure 4.3 and 4.4, this finer-grained layer extends up to approximately 100 μm below the surface. Besides the refined grains, undeformed larger grains with sizes similar to those

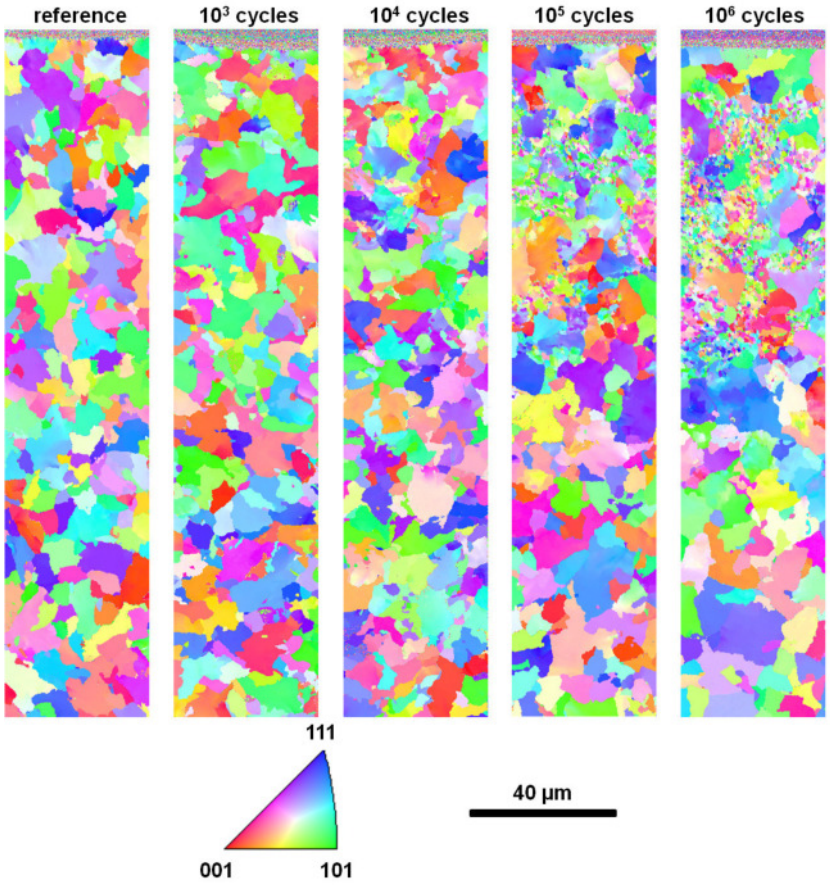

Figure 4.2: Inverse pole figure maps of the pristine reference state, after 10^3, 10^4, 10^5 and finally 10^6 cycles recorded by EBSD. The color coding is according to the standard orientation triangle highlighting the crystallographic orientation of the individual grains.

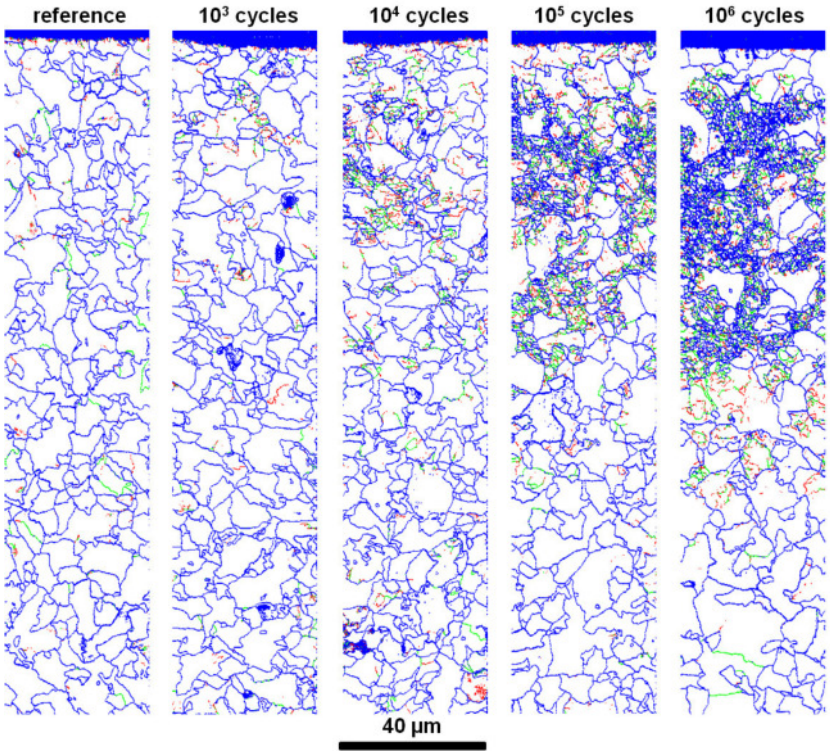

Figure 4.3: Grain boundary plots of the pristine reference state, after 10^3, 10^4, 10^5 and finally 10^6 cycles recorded by EBSD. The color coding represents the minimum and maximum threshold values for the grain misorientation (red: 2-5°, green: 5-15° and blue: >15°).

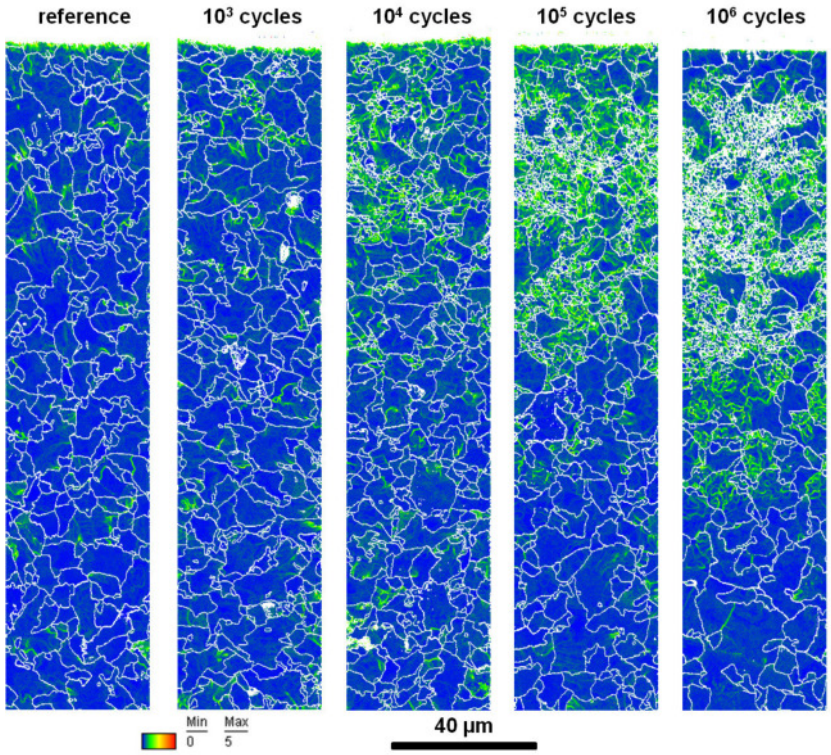

Figure 4.4: Kernel average misorientation maps of the original reference specimen, after 10^3, 10^4, 10^5 and finally 10^6 cycles determined by EBSD. The color coding corresponds to the misorientation values from 0 to 5 degree. According to equation (2.32), the rainbow scale also represents the GND density. White lines represent high-angle grain boundaries.

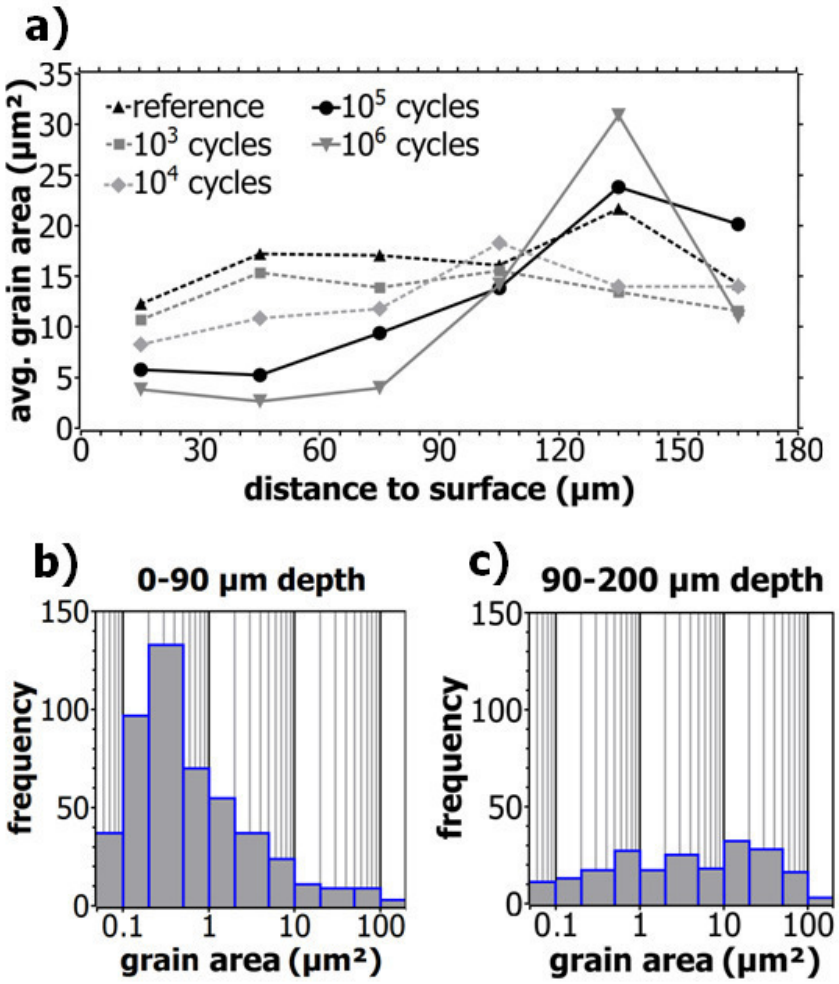

Figure 4.5: This figure shows the grain area distribution as a function of the distance to surface given by EBSD (a). In (b) and (c) the grain area distribution for the fine grained (0-90 μm) and the bulk region (90-200 μm) is plotted.

of the bulk material can be found in the tribologically affected region (see plots after 10^5 and 10^6 cycles in figures 4.3 and 4.4).

Figure 4.5a shows the grain area distribution as a function of the distance to surface given by EBSD. Due to the mentioned remaining larger grains in the near-surface region, a standard deviation of the average grain area would not be meaningful. A comparison of the grain area distribution is plotted (figures 4.5b and 4.5c) instead for 10^5 cycles. The figures allow for a quantification of the grain refinement. The average grain area in the grain-refined region drops down to values of approximately 9 μm^2 after 10^4 cycles, approximately 5 μm^2 after 10^5 cycles and approximately 3 μm^2 after 10^6 cycles (see figure 4.5a). Aside from decreased grain areas, grains after 10^5 and 10^6 cycles show an increase of the refined region compared to 10^4 cycles. Moreover, the distribution of grain areas shows an increase in grain area below 1 μm^2 in the grain-refined region (figure 4.5b) compared to the bulk-like microstructure (figure 4.5c). The density of LAGBs (2° to 15°) is plotted in figure 4.6d versus the distance to the surface. Figure 4.6 that the concentration

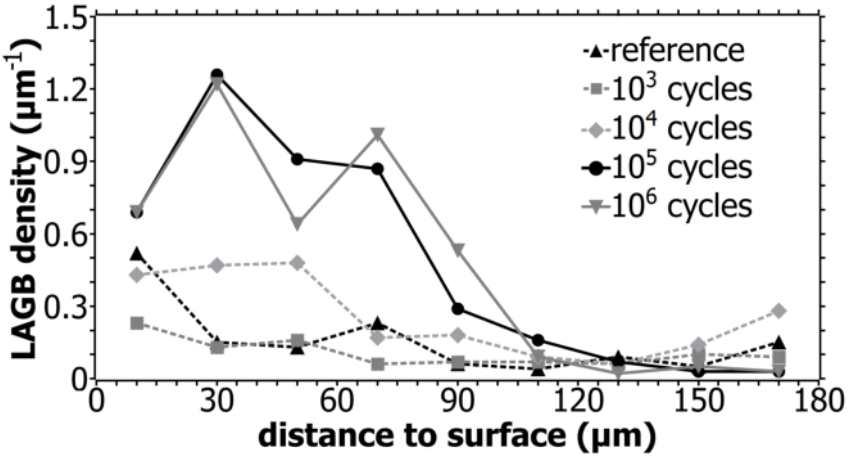

Figure 4.6: Low-angle grain boundary (LAGB) density plot as a function of distance from the surface determined by EBSD.

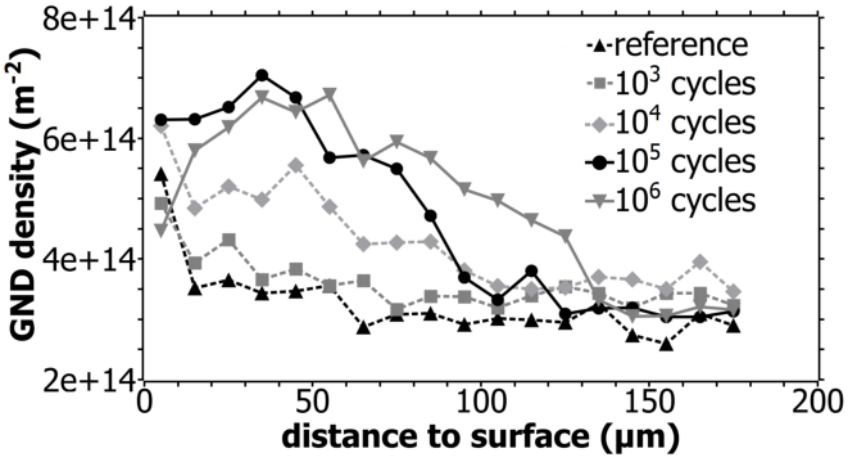

Figure 4.7: Density plot of GNDs as a function of the distance from the surface for the different sample states.

of LAGBs approximately quadruples every logarithmic interval at a depth of 30 μm from the surface, where the highest concentration of LAGBs is found. However, between 10^5 to 10^6 cycles the LAGB density remains constant. This region with increased LAGB density can also be visually identified in figure 4.3. A representative HAGB density cannot be convincingly determined, since grain defects such as pores or inclusions are misleadingly labelled as HAGBs. In any case, the information regarding HAGBs is included in the grain area distribution. KAM values were used as a measurement of plastic strain for the EBSD samples. This parameter increases in a small region close to the wear track surface at 10^3 cycles (figure 4.4), beyond which this region expands deeper into the material. The KAM values are used to calculate GND densities according to equation (2.32) and the GND density is plotted versus the distance to the sliding surface in figure 4.7. The bulk GND densities amount to $3.5 \cdot 10^{14}$ m^{-2}. All plotted curves show an increase up to values between $5.5 \cdot 10^{14}$ m^{-2} and $6.5 \cdot 10^{14}$ m^{-2} when getting closer to the sliding surface. Both, the reference and the 10^3 cycle curves show the same behavior with higher GND densities in the first 20 μm below the surface which is caused by the surface preparation before tribological testing. Additional cycles extend the strained region: 10^4 cycles produce GND densities of ca. $5 \cdot 10^{14}$ m^{-2} at 60 μm depth and 10^5 cycles as well as 10^6 cycles even exceed $6.5 \cdot 10^{14}$ m^{-2} with a drop to bulk values at a depth of approximately 80 μm.

4.1.2 Strain distribution in the constituent phases

Considering the above presented results, one mandatory question remains: the question of the mechanical response of each of the two phases and the ratio of their participation in the strain formation. Therefore, it is necessary to separate the strain information of the ferritic grains from the values for pearlitic grains. The first attempt was to achieve a separation by means of quantitative values. Since pearlite grains are formed by a lamellar structure of ferrite and cementite, they are expected to yield in a lower pattern quality (Iza-Mendia/Gutiérrez, 2013). This approach was proposed by De Meyer et al. (Meyer/Kestens/Cooman, 2001) for separating ferrite and bainite in textured steels. The confidence index is also considered since it correlates the Kikuchi pattern to a specific crystal phase and might be potentially lowered by the presence of cementite in the pearlite grains. In this case, the grain average values of pattern quality and confidence index show a monomodal distribution for 10^5 cycles. Moreover, the pattern quality is also affected by plastic deformation caused during surface preparation and tribo-testing (Calcagnotto et al., 2010). Therefore, neither the pattern quality nor the confidence index are able to show a clear separation between ferritic and pearlitic grains. Therefore, a quantitative separation by using these values was not possible.

Optical microscopy showed better segregation results by a bimodal distribution. Since the brightness of the pearlite depends on the fraction and orientation of the cementite

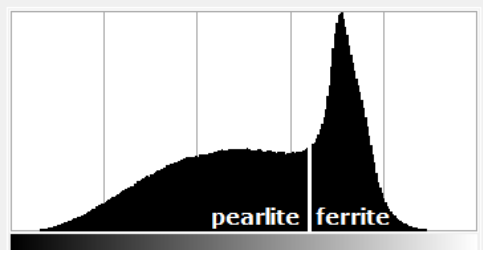

Figure 4.8: Gray level histogram of Fig. 1 showing the margin between ferrite and pearlite, which serves as basis for phase segmentation in figure 4.9 and 4.10

lamellae at the cross-section, a wider range of gray scales is observed for the pearlite phase. Ferritic grains are expected to have uniformly bright gray scale values since they should have an (optically visible) artifact-free surface. The gray-scale histogram (figure 4.8) of the cropped micrograph (background in figures 4.9 and 4.10) showed two such regions: a wide darker deviation of gray scales (identified as pearlite) and a narrow brighter region (ferrite). Based on the gray scale, masks of the optical micrographs were generated allowing for a qualitative separation of the two phases for the investigated region. The generated ferrite/pearlite mask and the original micrograph were combined with either inverse pole figures (IPF) or KAM maps of exactly the same region (figure 4.9 and 4.10). These figures are layered, from front to back, as follows: mask, EBSD plot (IPF in figure 4.9 and KAM in figure 4.10) and optical micrograph. The track is located on the top left of the image, its edge reaching approximately the middle of the EBSD plot. The information (grain boundaries, misorientation) provided by the EBSD plot is thus visible with respect to the specific phase, highlighted by the mask. The ferrite grains clearly depict a region of microstructural recrystallization (figure 4.9) and a region of higher misorientation or rather GND density (figure 4.10) underneath the wear track. However, the pearlite grains represent similar lattice domain (grain) sizes as the bulk material (figure 4.9) and a random low misorientation deviation or slightly elevated misorientation over the entire plot (figure 4.10).

4.1.3 Grain refinement and strain incompatibilities

For achieving information about the strain incompatibilities at the boundaries between ferritic and pearlitic regions, the high resolution of TEM was necessary. Moreover, this allows for a better analysis of the grain refinement since the grain dimensions reached low values. For a further validation of EBSD measurements on a higher resolution, the same regions were investigated using EBSD, TEM as well as TKD. Therefore, the cross-section lamella was extracted in a way as in the work of Lozano-Perez (Lozano-Perez, 2008). The position of the lamella was selected based on previous EBSD scans in a region of grain refinement with larger grains at the corners. The region of lamella extraction is shown in figure 4.11. A tilted lamella was prepared in the same way parallel to the cross-section

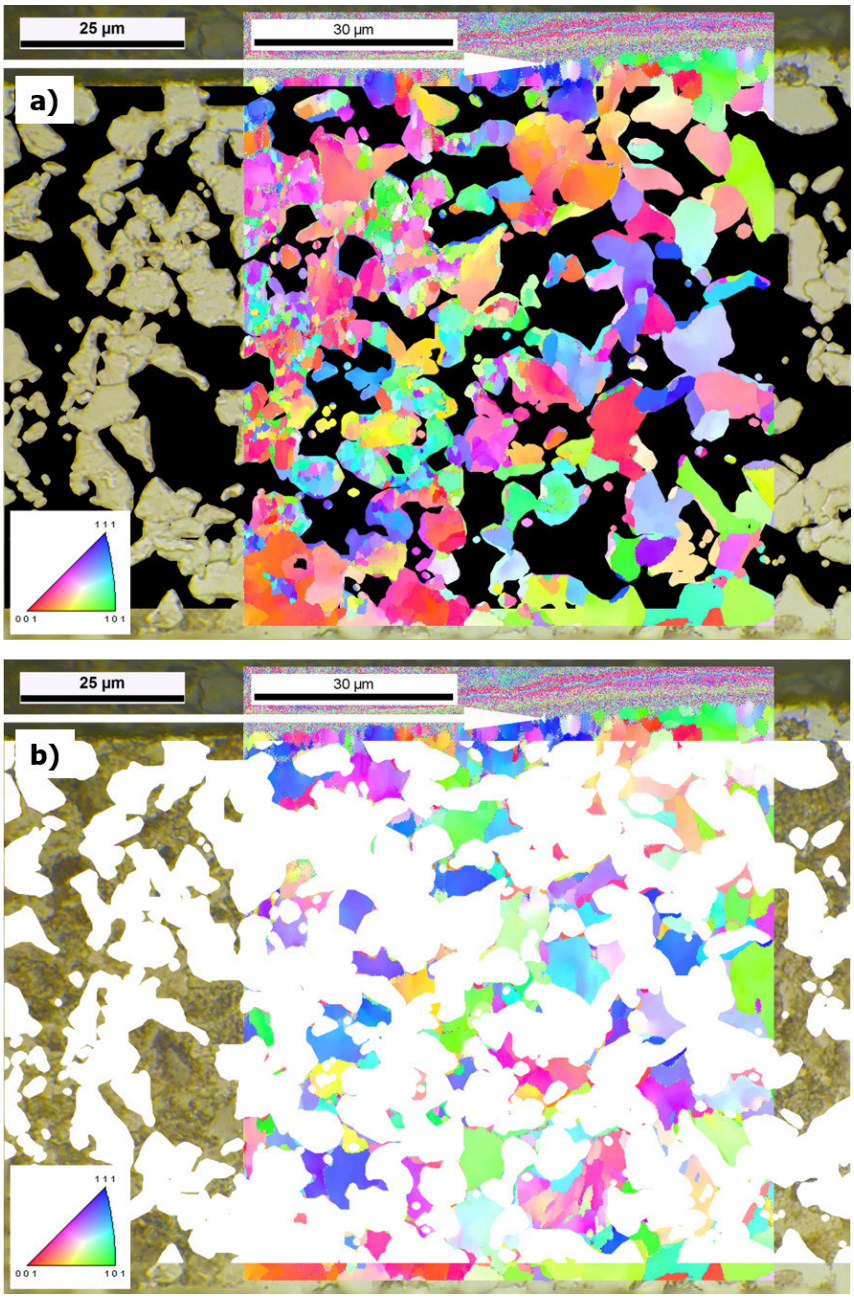

Figure 4.9: a) Segmented optical micrograph only showing the bright ferritic phase with an overlayed inverse pole figure map recorded by EBSD. The arrow denotes the direction from the top of the surface into the bulk. b) Segmented optical micrograph only showing the dark pearlitic phase with an overlayed inverse pole figure map recorded by EBSD. The arrow denotes the direction from the top of the surface into the bulk.

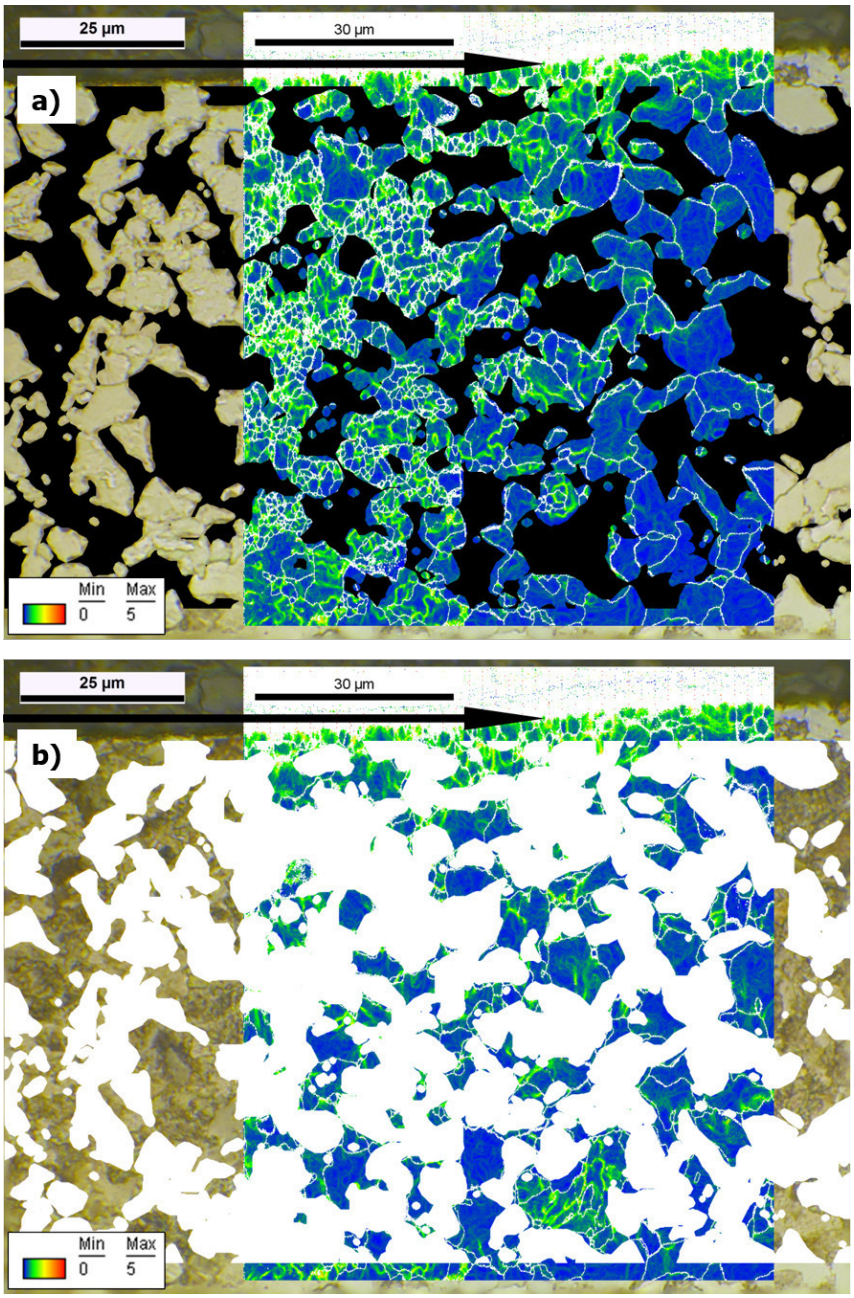

Figure 4.10: a) Segmented optical micrograph only showing the bright ferritic phase with an overlayed KAM map recorded by EBSD. The arrow denotes the direction from the top of the surface into the bulk. b) Segmented optical micrograph only showing the dark pearlitic phase with an overlayed KAM map recorded by EBSD. The arrow denotes the direction from the top of the surface into the bulk.

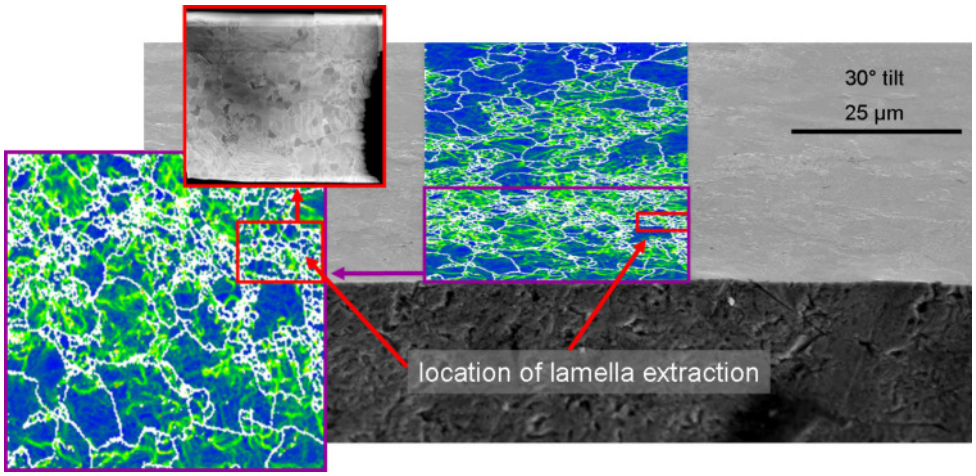

Figure 4.11: SEM micrograph showing a EBSD-KAM image at a cross-section of a sample after 10^5 cycles with the position from which the TEM lamella was extracted.

but using a cross-section with a shallow angle to the tribologically tested surface. The purpose of the latter was to characterize the shape of the refined grains in the longitudinal direction.

Figure 4.12a displays the cross-section lamella imaged by TEM showing a clear grain refinement after 10^5 cycles to grain sizes of less than 2 μm, as observed in the EBSD measurements. All microstructural plots of the refined grains appear with equiaxed grains. Even in longitudinal direction (tilted lamella), the refined grains remain equiaxed after refinement by the sliding contact. The region affected by the grain refinement is ferritic. The pearlitic regions are found as larger grains at the corner of the lamella. Additional TKD scans of these regions (figure 4.12b) highlight a grain-refined ferrite accompanied by larger pearlite grains. The TKD technique was required since it provides a better possibility to distinct between the perlite grain boundaries. Since the position of the lamellae with respect to the previous EBSD measurements is known, an overlay of the EBSD data and the TEM data can be done. In general, the results clearly state that a larger amount of grain boundaries can be identified in the TEM and TKD images when compared to the EBSD images including those explicitely showing LAGB. Even though a perfect overlay is no longer possible after the necessary polishing step for the lamella preparation (approximately 100 nm of material removal), pearlitic and ferritic regions can be unambiguously identified in the TEM figure and correctly located in the EBSD data set. By the comparison of ferritic regions neighbouring the pearlite and regions located far away from the pearlite, it can be observed that the regions of higher misorientation are not always necessarily found at ferrite regions surrounding pearlite grains (see figure 4c, also figure 3d as another example at lower magnification). Nevertheless, the edge of the pearlitic region has also undergone grain refinement. It seems as the pearlite grains refine at the edges to the ferritic regions, whereas the larger pearlite grains show less strain (figure 4.12c). Strain incompatibilities at the grain boundaries were studied

by the formation of dislocations at the interface between ferritic and pearlitic grains using high resolution TEM. Ferrite-perlite grain boundaries were studied and compared to ferrite-ferrite boundaries. Because of the very local investigation done on two TEM lamellae, only a qualitative information can be received. Figure 4.13a and 4.13b show grain boundaries between ferrite and pearlite. The figures show regions with strong contrast in the ferrite grain, especially pronounced at the interface between ferritic grains and ferritic lamellae of the pearlite. These darker regions were present when observing the grain boundary using different tilting angles. Therefore, they were attributed to the formation of dislocation pile-ups. These dislocation formations could be found at several interfaces between ferrite and pearlite grains but not on all of them. In contrast to that, these dislocation pile-ups were not found at ferrite-ferrite interfaces. Although, ferrite-ferrite interfaces showed darkened regions at the interface, a tilting of the lamellae to align the grain boundary parallel to the measurement direction revealed the lack of dislocations pile-ups (e.g. figure 4.13c and 4.13c). Due to the necessary thickness of the lamellae to prevent bending by residual stresses, a quantitative evaluation of dislocation densities is hard to perform and when done, unreliable since the information gained corresponds to very localized sub-surface regions. Concerning mechanical properties of the sub-surface layer and its constituent phases, hardness measurements were done along the sub-surface depth after 10^5 cycles (figure 4.14a) as well as at a constant 30 μm depth with varying number of cycles (figure 4.14b). The latter are shown along with the corresponding KAM plots. The figures show a clear correlation between the hardness and the GND density, in turn related to cycles and depth. At 30 μm underneath the wear track the hardness increases from a reference value of 250 $\pm$20 HV to almost 300 HV after 10^5 cycles. Moreover, at this point, the increased hardness reaches a depth of approximately 200 μm underneath the wear track. The slight difference between the reference hardness (250 $\pm$ 20 HV) at 30 μm beneath the surface (figure 4.14b) and the bulk hardness (230 $\pm$ 20 HV in figure 4.14a) is likely due to plastic strain introduced by the sample preparation (grinding and polishing) before the sliding tests. Due to the grain refinement in the ferrite phase, the mechanical properties change during sliding. Allain and Bouaziz (Allain/Bouaziz, 2008) calculated the mechanical properties of pearlitic steels for different interlamellar spacings and for pure ferritic steels as a function of their grain size. Based on their model (equation (3.1) and (3.2)), stress-strain curves of the constituent phases were calculated for the undeformed ferrite microstructure, the grain refined ferrite after deformation and the undeformed pearlite phase underneath the contact. For the pearlite, an average interlamellar spacing of 150 nm was used. The comparison of the three stress-strain curves in figure 5c shows an increase in yield strength from approximately 200 MPa to >700 MPa for the ferrite phase due to the grain refinement. The stress-strain relation for pearlite depends on the lamellar spacing (equation (3.2)). As displayed by TEM, the interlamellar spacing did not change during the tribological testing. Therefore, for pearlite only one stress-strain

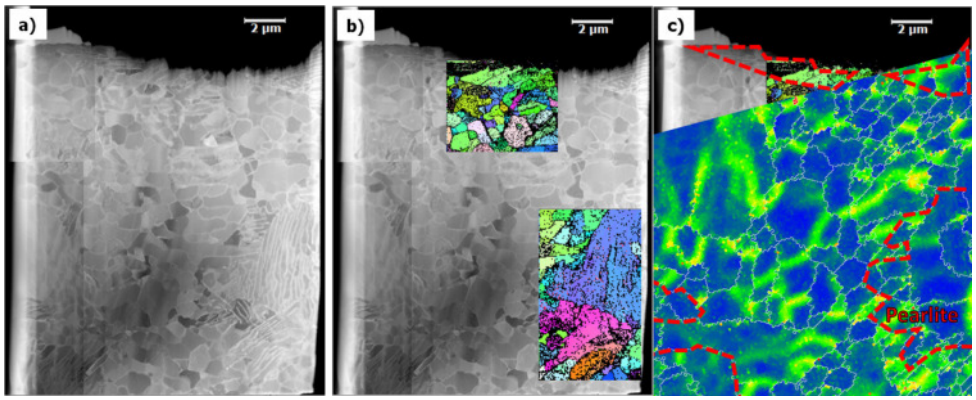

Figure 4.12: a) High-angle annular dark-field (HAADF) micrograph showing the grain refinement after 105 cycles. Here, the cementite lamellae are clearly visible and unambiguously identify the unrefined pearlitic region. In b) additional TKD results are presented and linked to the respective position on the TEM lamella. The upper inserted TKD plot is located in the ferritic region whereas the lower TKD image is in the pearlitic region. c) Overlay of EBSD information over the TEM/TKD image. The red colored region represents the pearlite region as identified by TEM (the plane of the TEM lamellar was milled down approximately 100 nm from the original cross-section where the EBSD measurement was done).

curve was calculated, which gives a yield strength of approximately 1100 MPa.

4.1.4 Influence of lubrication conditions on plastic strain

So far, only the influence of the strain development was studied regarding the number of cycles as well as the specific phases. This section focuses on the relation between the respective lubrication condition as well as the normal load and the resulting strain. For testing the influence of the lubrication condition, two different oils with a relative high and low viscosity where used as lubricants. Since the lubrication condition has an influence on the stress distribution, the strain distribution should also be different. For a better understanding, the first subsection describes the lubrication condition in detail while the second sub-section shows the resulting wear. The following two sections show the microstructural response of the material concerning the lubrication condition as well as the normal load, respectively.

Lubrication regime The lubrication regime was determined by calculating the lambda ratio (λ) according to Tallian (Tallian, 1972) as the ratio between the minimum film thickness according to Hamrock and Dowson (Hamrock/Dowson, 1977) and the combined surface roughness. The selected testing conditions yield $\lambda = 0.09$ for the FVA1 oil (F = 20 N) and $\lambda = 0.62$ and 0.52 (F = 20 N and 120 N, respectively) for the FVA4 oil. Therefore, the tests with both lubricants were performed in the boundary lubrication regime ($\lambda < 1$), independently of the applied normal load. Moreover, the lubrication

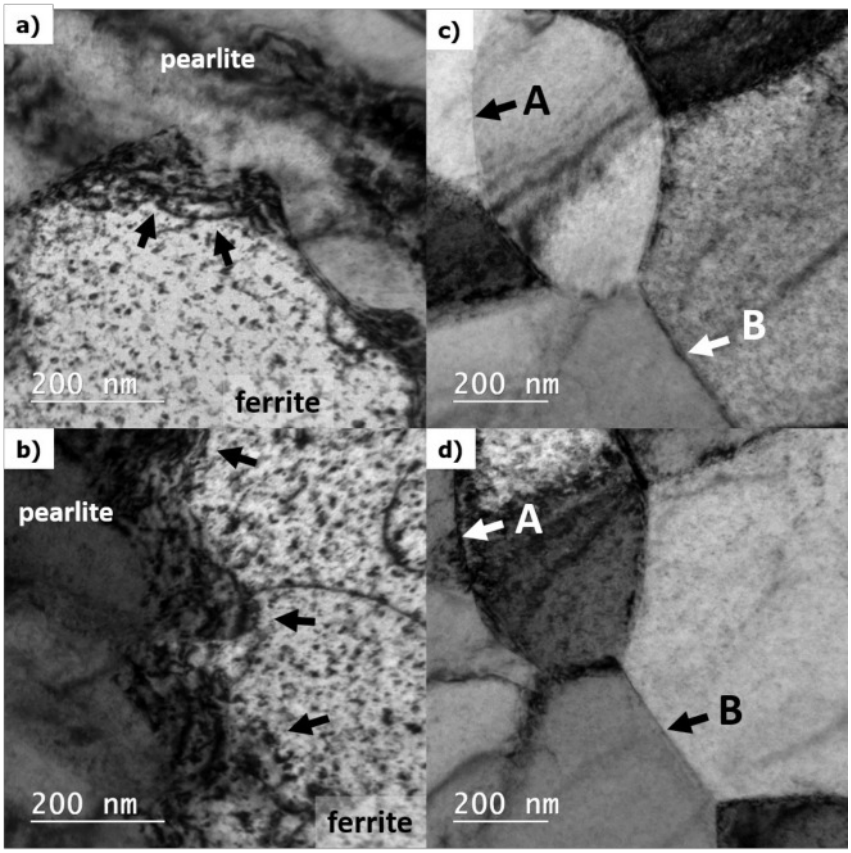

Figure 4.13: a) and b) Grain boundaries between ferrite and pearlite grains imaged by TEM. The arrows mark regions of dislocation formations in the ferrite grain, directly at the grain boundary. c) and d) TEM images of ferrite-ferrite grain boundaries are visible (c) and d) show the same region with different tilt angle) Markers A and B reference the same grain boundary in each figure.

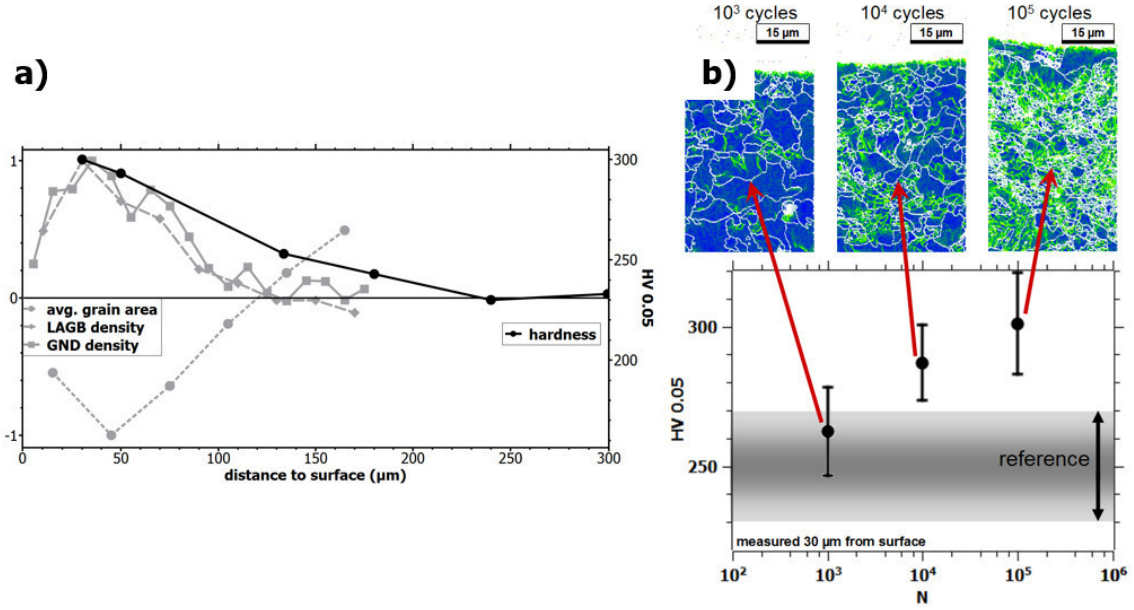

Figure 4.14: a) Vickers hardness measurement along the sub surface depth for a sample after 10^5 sliding cycles compared to normalized values of avg. grain area, LAGB and GND density for the same sample. The curves are normalized to the difference to the reference sample (representing 0) and the maximum absolute difference to the reference value (representing 1/-1). b) Vickers hardness measurements at a defined depth of 30 μm for different cycle numbers and linked with the respective KAM maps.

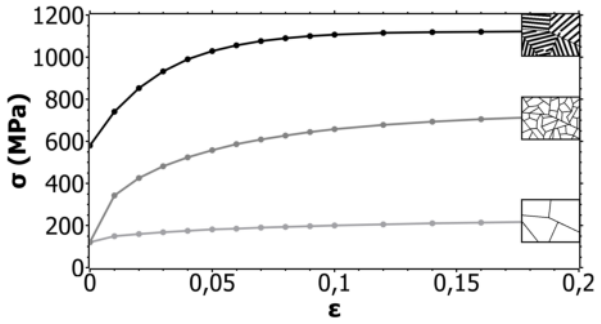

Figure 4.15: Stress-strain curves for the unrefined ferrite (light gray), grain refined ferrite after 10^5 cycles (dark gray) and pearlite phase (black) calculated according to (Allain/ Bouaziz, 2008).

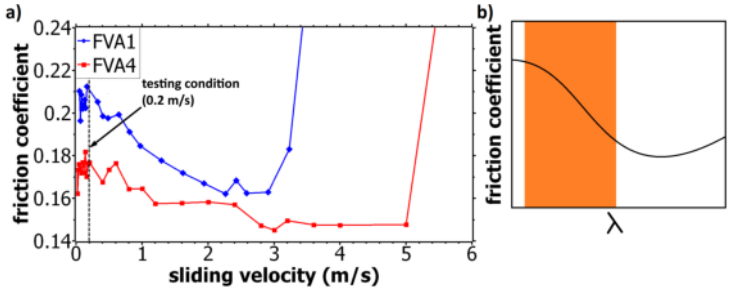

Figure 4.16: a) Stribeck curves of the two tested oils based on the sliding speed; b) scematic drawing of a Stribeck curve with the approximate region of the values represented in figure a).

regime was verified experimentally by Stribeck curves (see figure 4.16). At low speeds i.e. in boundary lubrication regime, the friction coefficient at 20 N of the FVA1 oil is slightly higher ($\mu_{FVA1} = 0.205$) than for the FVA4 oil ($\mu_{FVA4} = 0.175$), due to the differences in viscosity for both oils. The values of the friction coefficient drop for both oils at approximately 0.6 m/s, indicating the onset of hydrodynamic lubrication. This velocity is a factor 3 higher than those used for the sliding-tests (0.2 m/s). For larger velocities, rupture of the lubrication film due to starvation is observed for both oils, being the critical speed for the FVA1 oil (> 3 m/s) lower than for the FVA4 oil (> 5 m/s).

Wear as a function of normal load and viscosity Wear profiles measured from topographic cross-sections are shown in figure 4.17. The comparison of both lubricants at 20 N normal load after 10 000 and 100 000 cycles reveals that the wear scar depth is in general much lower for FVA4 lubricated samples. More remarkable is the fact that the relation between the removed wear volume and the displaced material forming side ridges due to plastic deformation is much higher in FVA4 lubricated samples compared to FVA1. When evaluating the influence of normal load on the FVA4 lubricated samples, we can observe that the volume of the side ridges becomes rather similar to the removed wear volume, especially for 120 N. In case of FVA1, the highest side ridges are observed only for the lowest number of cycles but even in this case, their total volume is smaller compared to the removed wear volume. Additionally, for the FVA1 lubricated sample, the relation between wear track depth and wear track width is much higher.

Microstructural evolution as a function of viscosity The initial microstructure of the ferritic/pearlitic steel is shown in figure 4.18. The orientation based inverse pole figure (figure 4.18a) shows the distribution of domains of similar orientation (grains). The boundary plot (figure 4.18b) shows the local orientation changes representing HAGBs (blue) as well as LAGBs (red and green). The KAM plot (figure 4.18c) shows gradients of orientations, thus representing a local misorientation of less than 5°. According to equation (2.32) the KAM value is also linearly dependent on the GND density. The

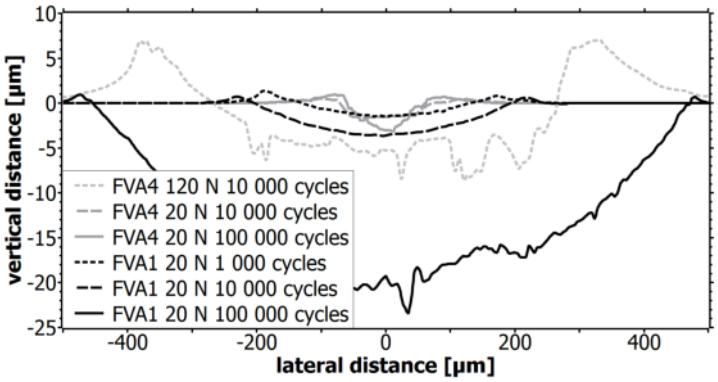

Figure 4.17: Topography of the wear tracks measured by white light interferometry and averaged over a 575 μm wear track length

EBSD plots of the reference surface show a homogeneous microstructure with low LAGB densities, and insignificant misorientation. Very close to the surface, the material shows a minor degree of plastic deformation due to the surface finishing processes (e.g. grinding and lapping).

The orientation based inverse pole figure plots in figure 4.19a show the microstructure of the two samples after 100 000 cycles tested using oils with different viscosity. The grain size distribution can be seen in more detail in the boundary plot of figure 4.19b. The results show that for the low viscosity oil (FVA1), grain-refinement occurs directly beneath the surface. The grains have a size of approximately 1 μm. The refinement fades into the sample with increasing depth up to 20 μm. Similar to the grain sizes, the LAGB as well as GND densities also show a maximum value directly at the surface. The deformed region characterized by an increase of LAGB and GND density reaches a depth of approximately 40 μm. Below 40 μm, the original undeformed microstructure is found. In contrast, the closest region to the surface is much less strained with the higher viscosity lubricant (FVA4) (see figure 4.19b). Large grains are still found practically undeformed directly at the surface and grain refinement starts approximately 10 μm below. This region is characterized by increased LAGBs and GNDs densities that lead to similar grain sizes as in the strained region of the FVA1 samples. The refined microstructure extends up to 80 μm below the surface, when the grain sizes become similar to the reference values. The surface close region (until 10 μm) also shows smaller densities of LAGBs and GNDs as a consequence of surface preparation. For a quantitative comparison of the role of lubricant viscosity on plastic deformation, values of the average grain area (figure 4.20), LAGB density (figure 4.21) as well as GND density (figure 4.22) are plotted against the distance from the surface and are compared to values of the reference samples. Each tested configuration is represented by two measurements for the sake of reproducibility. In general, these quantitative plots confirm the results gained by the qualitative analyses but show the differences in more detail. The measurements on the undeformed sample

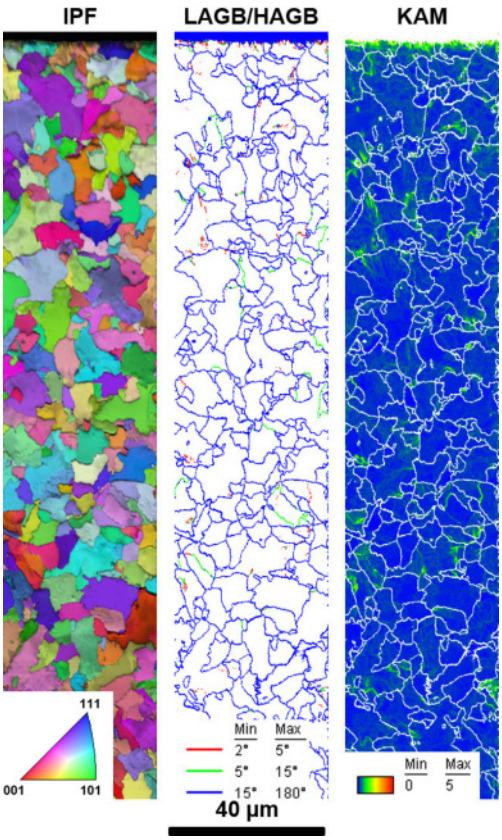

Figure 4.18: Initial microstructure plotted as measured by EBSD: a) inverse pole figure (IPF), b) low-angle grain boundaries (LAGBs: red for 2° to 5°, green for 5° to 15°) and blue: high-angle grain boundaries (HAGBs >15°), c) kernel average misorientation (KAM).

(figure 4.18) illustrates rather constant values in terms of average grain area as well as LAGB density. A slight increase of GND density is visible directly at the surface (figure 4.22), which is attributed to surface preparation prior to the tribological testing. As shown in the EBSD plots (figure 4.19), the plastic deformation in the FVA1 samples is highest directly at the surface (see figure 4.20). Thereby, the avg. grain area drops down to 4 μm^2. Similar values are measured for the samples tested with FVA4 lubricant. However, the region of grain refinement only reaches approximately 30 μm for FVA1 whereas for FVA4, the affected region extends down to approximately 60 μm. The region of larger grains at the closest surface interface of the FVA4 samples is not captured by the plot due to the resolution.

In terms of LAGB densities (figure 4.21), the reference as well as the bulk values of the tests show consistent low values of approximately 0.1 μm^{-1} to 0.2 μm^{-1}. The FVA1 samples show the highest densities (1.5 μm^{-1} to 3.25 μm^{-1}) directly at the surface with a subsequent decrease up to reference values up to approximately 40 μm from the surface. The slight difference observed between the two measurements might arise from the inhomogeneous topography due to the presence of wear grooves inside the wear track. In contrast, the highest LAGB density of the FVA4 lubricated samples can be found (approximately 1.4 μm^{-1}) at a depth of approx. 30 μm underneath the surface. Directly at the surface, the LAGB density reaches a lower value of approximately 0.8 μm^{-1}, thus less than in the region of highest Hertzian stresses. LAGB densities similar to the reference values are not found until 110 μm from the surface.

In agreement with the previous results, the GND density (figure 4.22) in the FVA1 lubricated samples is highest directly at the surface with a value of approx. $8.5 \cdot 10^{14}$ μm^{-2}, which represents an increase by a factor of two compared to the undeformed. The GND density fades to the reference values ($3.0 \cdot 10^{14}$ μm^{-2}) 50 μm below the surface. The maximum GND density values ($7.0 \cdot 10^{14}$ μm^{-2}) in FVA4 lubricated samples are found in a distance from the surface between 20 μm and 60 μm, except for the higher GND values present close to the surface due to sample preparation. The maximum GND density for the FVA4 lubricated samples is smaller than the one obtained for samples lubricated using FVA1. FVA4 lubricated samples reach reference values at a depth between 90 μm and 120 μm from the surface.

Influence of load on strain evolution For investigating the influence of load on plastic deformation, FVA4 lubricated samples were analyzed after being tested at normal loads of 20 N and 120 N during 10 000 cycles. The tests performed using a load of 120 N reveals a homogeneous grain refinement throughout the sample up a distance from the surface of approximately 150 μm. LAGB formations are found even at deeper regions than the grain refinement (see figure 4.23b). In this case, the LAGB density is higher throughout the whole measurement area (reaching 200 μm from the surface into the

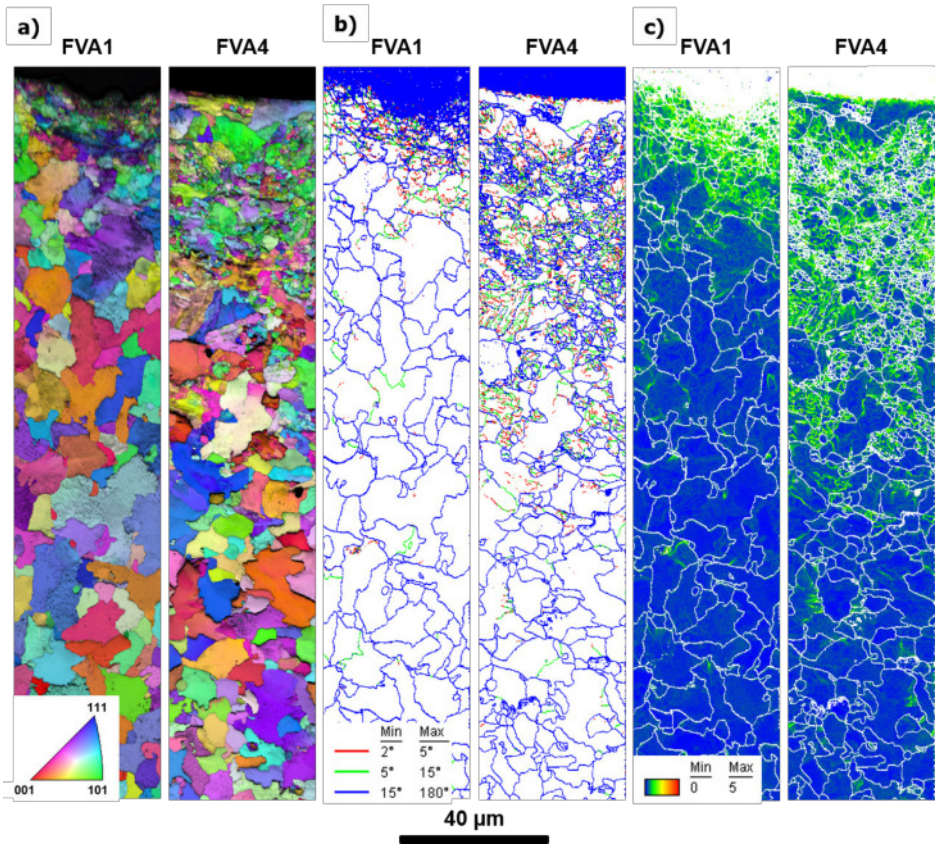

Figure 4.19: Comparison of the EBSD plots of samples tesed with FVA1 and FVA4 oils: a) IPF, b) LAGBs and HAGBs, c) KAM.

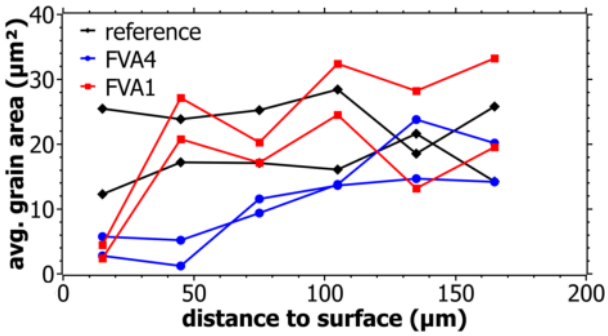

Figure 4.20: Comparison of averaged grain areas measured for FVA1, FVA4 and reference samples and averaged for 30 µm intervals.

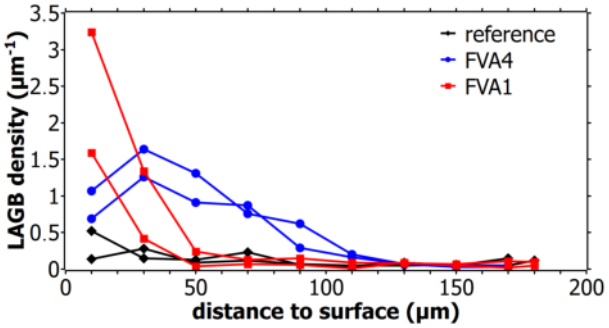

Figure 4.21: Comparison of density of LAGBs measured for FVA1, FVA4 and reference samples and averaged for 20 µm intervals.

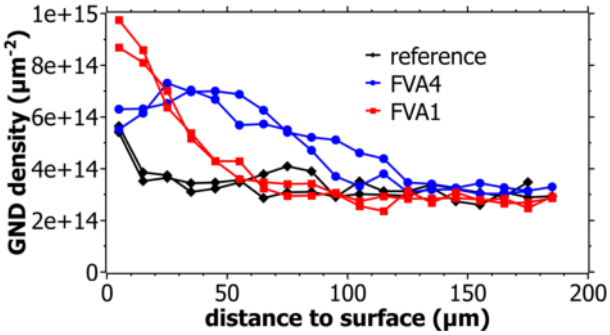

Figure 4.22: Comparison of GND density measured for FVA1, FVA4 and reference samples and averaged for 10 µm intervals.

material) but with a decrease starting approximately 150 μm beneath the surface. For 20 N, no significant refinement in the sample is observed (see figure 4.23a, b). The plastic deformation is evidenced by the formation of LAGB at approximately 20 μm to 60 μm from the surface. Consequently, the misorientation plot (figure 4.23c) indicates an increased misorientation from 20 μm to approximately 80 μm from the surface for the 20 N sample. The line at the bottom with increased misorientation is caused by a sample preparation artefact (grinding scratch). Testing was also performed with higher normal loads but the severe plastic deformation of the crystallographic structure of locations close to the surface does not allow for a quantitative analysis anymore (see figure 4.24).

The quantitative data obtained from the EBSD analyses provides a more detailed overview of the deformation process. The grain sizes (by means of average grain area in figure 4.25) of the samples tested at 20 N are similar to the reference values (12 μm^2 and 35 μm^2). Only a slight trend to grain refinement can be observed towards the surface at distances below 100 μm. A higher load (120 N) significantly refines the microstructure about an order of magnitude from the surface to approximately 150 μm, with a minimum avg. grain area of 1 μm^2.

The LAGB density (figure 4.26) for the samples tested with 20 N normal load shows a minor increase compared to the reference samples until density values of 0.4 μm^{-1}. The region of higher LAGB density values reaches a distance of approximately 50 μm from

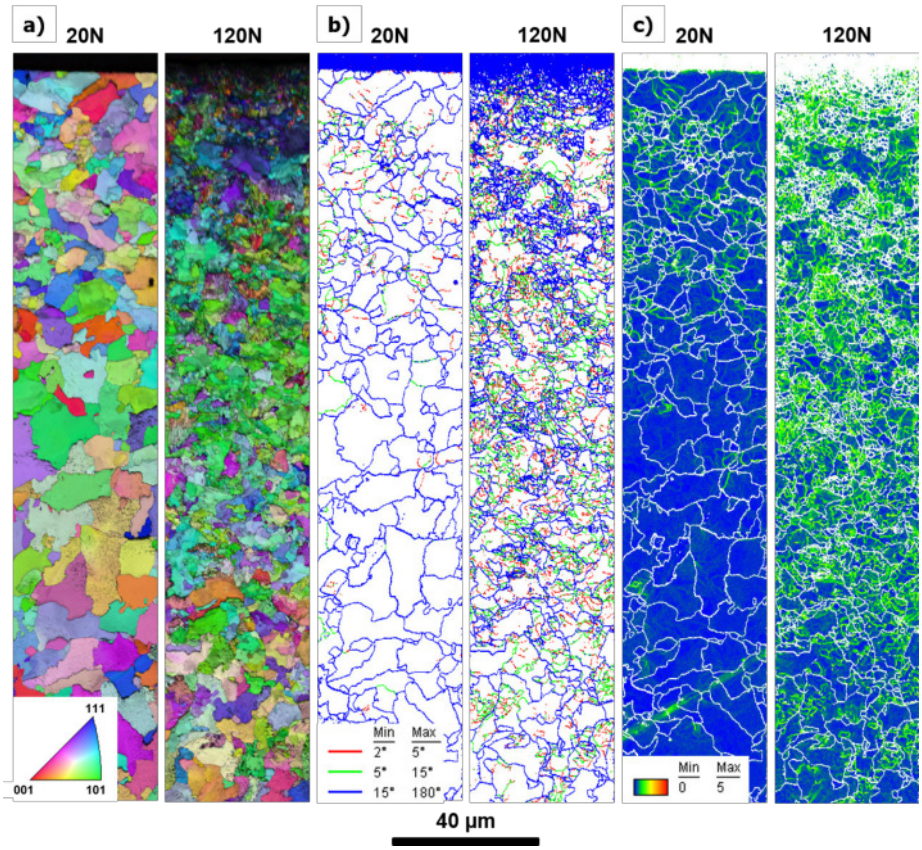

Figure 4.23: Comparison of the EBSD plots of samples tesed with 20 N and 120 N: a) IPF, b) LAGBs and HAGBs, c) KAM.

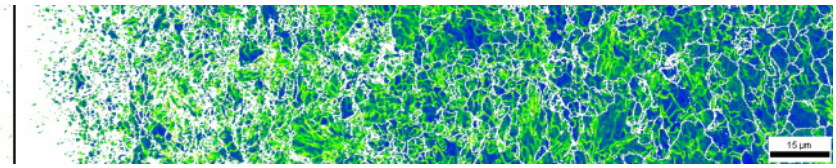

Figure 4.24: KAM image of a cross-section after tribological testing with 420 N normal load for 10^4 cycles and FVA4 lubrication. The origin surface is marked by the black line on the left side of the image (image is tilted 90° anticlockwise).

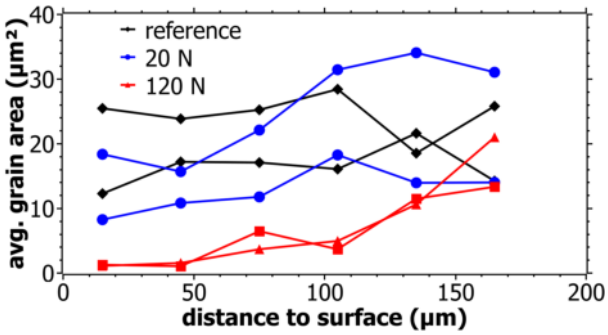

Figure 4.25: Comparison of averaged grain areas measured for 20 N, 120 N and reference samples and averaged for 30 µm intervals.

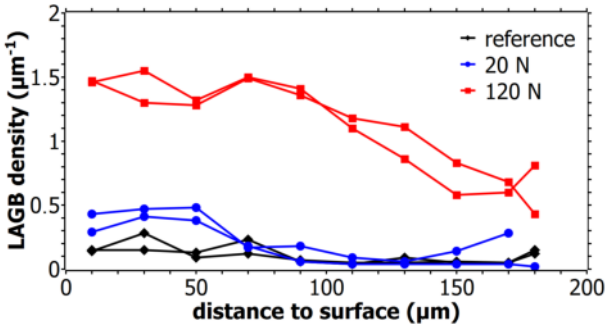

Figure 4.26: Comparison of density of LAGBs measured for 20 N, 120 N and reference samples and averaged for 20 µm intervals.

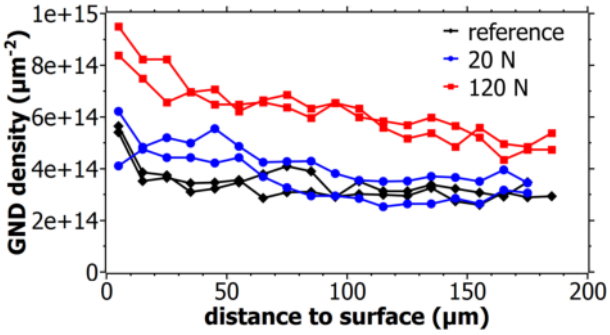

Figure 4.27: Comparison of GND density measured for 20 N, 120 N and reference samples and averaged for 10 µm intervals.

the surface. Much higher LAGB densities are found in the 120 N samples, reaching values up to 1.5 μm^{-1} in the region comprising the initial 100 μm from the surface. Here the total affected region reaches deeper than for the 20 N normal load samples, not reaching reference values until a depth below 180 μm. Therefore, plastic deformation is found in even deeper regions by means of LAGB density compared to grain refinement.

The density of GND increases by more than $1 \cdot 10^{14}$ μm^{-2} for the samples tested at 20 N normal load. The region of increased GND density reaches from the surface until approximately 60 μm. For the samples tested at 120 N, the density of GND is higher than for the reference sample in the whole measurement range. The highest densities are found directly at the surface. The highest values reach up to approximately $8 \cdot 10^{14}$ μm^{-2}. Afterwards, the density steadily decreases with increasing distance to surface until reaching a value of $5 \cdot 10^{14}$ μm^{-2} at 180 μm. It should be noted that the GND density values at the closest surface vicinity are higher in all measurements (even reference) due to prior sample preparation.

4.2 Bidirectional motion - oscillation

A reversal of the sliding or rolling direction usually results in different wear phenomena. Thereby, one important factor might be the different evolution of residual stresses by re-

versing the shear stress direction. Residual stresses and subsequently plastic deformation might thus be different for bidirectional sliding than in unidirectional sliding. Due to the minor development of plastic deformation in FVA1 tested samples, the analysis focuses on results of FVA4 lubricated samples. Thus, surface near material containing residual stresses still remain for many cycles while it might be worn off quite fast when using FVA1 as lubricant. The first sub-chapter shows a general overview of the microscopically observed conditions of the surface of the wear track. The second sub-chapter shows the actual residual stresses while, as a comparison, the third sub-chapter shows the modeled stress distribution for a single cycle.

4.2.1 Microscopical analysis

The cyclic loading results in linear wear tracks of ˜2600 µm in length and 600 µm in width. Samples with less than 10^3 cycles show no damage such as cracks or pits in the wear track. During the test, a low friction coefficient (approx. 0.1) is present, and the resulting surface is almost intact. Scratch marks originally caused by the surface grinding are still clearly visible by passing through the whole track without any significant difference between the inner and outer part of the wear track. Thus, the abrasive wear is insignificant and hence surface damage, such as cracks, is not modified by a grinding process during the test (see figure 4.28a and b). All wear tracks with 10^4 and 10^5 cycles show surface imperfections in the wear track (e.g. see figure 4.28c). Investigating the wear track with higher magnification, especially with SEM, the imperfections can be identified as cracks, which develop parallel to the sliding direction before 10^4 cycles (see figure 4.29) and then propagate up to 10^5 cycles, forming flaws and pits in the wear track (see figure 4.30a). Furthermore, bumps are visible by SEM inside the wear track (see figure 4.30b). The changing surface topography with increasing cycles leads to a rougher surface within the wear track and can be clearly observed in figure 4.28d–f. The total depth of the wear tracks was determined by confocal microcopy with a maximum measured depth of approx. 3.5 µm. An analysis of FIB milled cross-section after 10^5 cycles revealed, that the crack propagation reaches only a couple of μm into the material (see figure 4.31).

4.2.2 Residual stress measurements

Reference measurements of the tribologically untreated sample regions showed a stress component of 44±21 MPa. The reference value was determined out of ten measurement spots at different regions of the sample with two directions each spot. Exemplarily, the $\sin^2\psi$ versus $d_{\{211\}}$ characteristics of the tribologically tested sample (10 cylces) is shown in figure 4.32. Hereby, the residual stresses result in 21±9 MPa in longitudinal direction and 188±18 MPa in transversal direction, respectively. Thus, a directional development of the residual stresses tend to higher values in longitudinal direction with tensile characteristics.

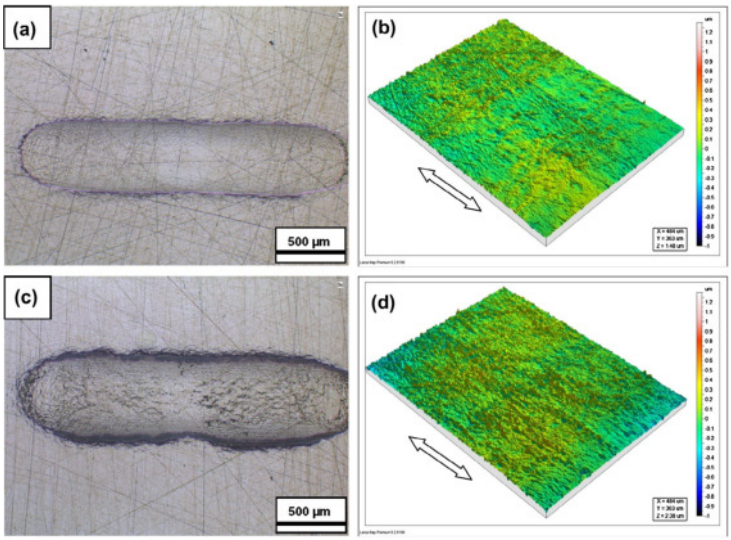

Figure 4.28: Macroscopic view of wear track (horizontal sliding direction) and 3D surface topography (360 x 480 µm) inside the wear tracks (plane fitted by polynomial fitting) for 10^3 (a and b), 10^5(c and d) cycles.

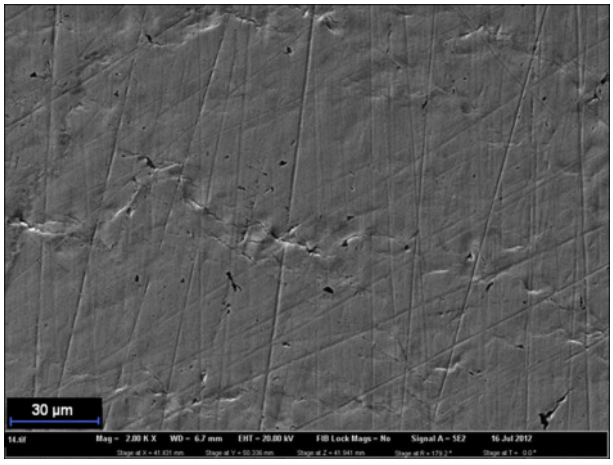

Figure 4.29: Surface inside of the wear track showing cracks propagating longitudinal to the sliding direction and scratches by surface grinding (horizontal sliding direction, 10^4 cycles).

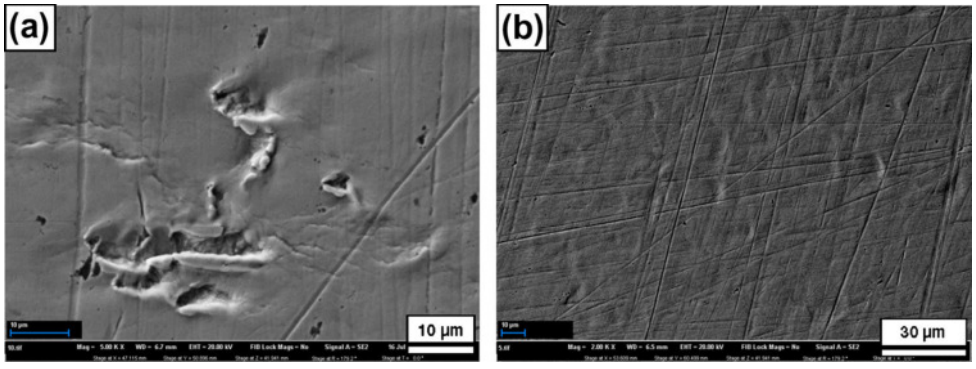

Figure 4.30: SEM of wear mechanisms: (a) Material breaking out of the surface after conjunction of cracks after 10^5 cycles and (b) Bumps formed inside of the wear track after 10 cycles (horizontal sliding direction).

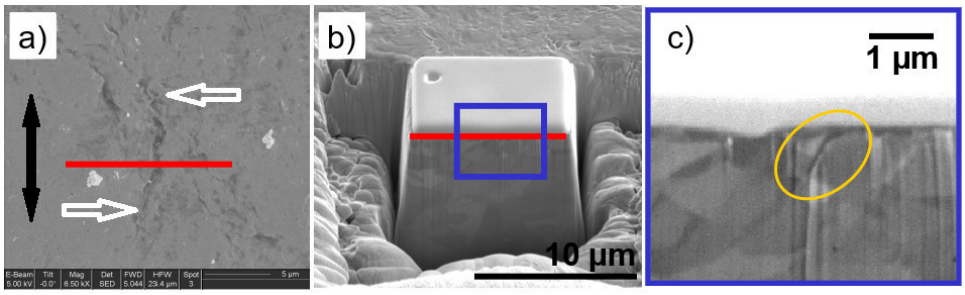

Figure 4.31: a) region of FIB-prepared cross-section. The red line marks the later cross-section surface, the black double-arrow marks the sliding direction and the white arrows mark the length of the crack. b) cross-section as prepared by FIB c) magnified region of b) imaging the crack, the vertical lines at the cross-section show curtaining-effects.

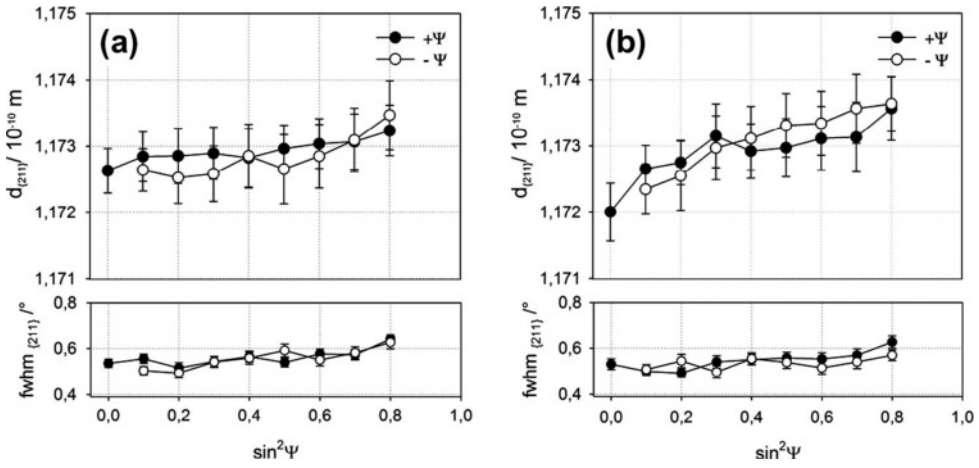

Figure 4.32: a) $\sin^2\Psi$ versus d {211} – (top) and fwhm {211} -plot (bottom) for the measurement along the grinding direction (longitudinal, S1, / = 0°) and b) $\sin^2\Psi$ versus d {211} – (top) and fwhm {211} – plot (bottom) for the measurement perpendicular the grinding direction (perpendicular, S2, / = 90°).

Moreover, neither a dependence of the tilt angle ψ for the two directions under sliding nor an orientation effect could be identified. The further evolution of the residual stresses is shown in figure 4.33 for logarithmic steps to 10^5 cycles (round symbols in figure 4.33). Even tough the absolute values between the measured residual stresses diversify between the two measurements, a similar development of the residual stresses is found for the two measurements. In longitudinal direction, the residual stress values demonstrate a slight increase till $\approx$ 100 MPa (tensile characteristic) for 10^5 cycles. Contrary to this slight increase in longitudinal direction, the residual stresses in transversal direction increase directly after 10 cycles till values around 200-300 MPa while staying nearly constant in the following state. Nevertheless, both tests show a slight reduction of the residual stresses from 10^4 to 10^5 cycles.

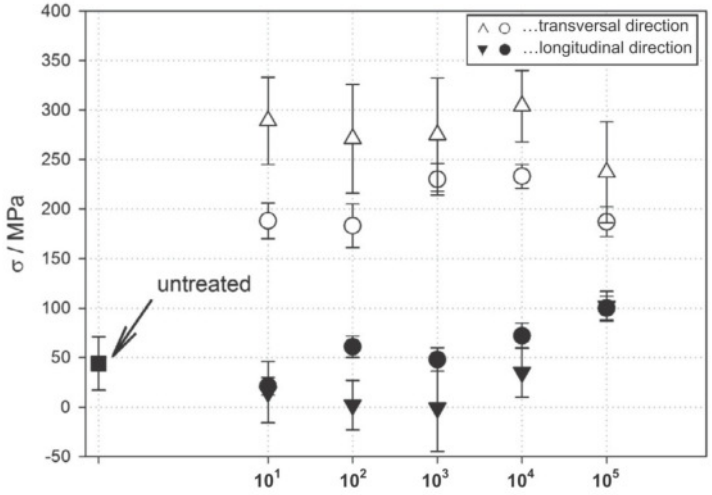

Figure 4.33: Stress development in dependence of the grinding cycles applied on the sample under investigation. Results of the analyzed stresses of two positions within the channel (mp1, mp2) are plotted. The closed and the open symbols represent the stress components analyzed for the longitudinal (S1, $\Phi = 0°$) and the transversal (S2, $\Phi = 90°$) direction in relation to the grinding direction.

4.2.3 Modelling of the elastic stress situation

For a later comparison of the plastic deformation of the material underneath the wear tracks and moreover a detailed understanding of the elastic stress situation introduced by the sliding contact, the von Mises stresses were modelled using the InstrumX (CSM instruments) modelling tool for the standard situation of a normal load of 100 N. Figure 4.34 (x/z) shows the von Mises stress situation for a hypothetical cross-section in longitudinal direction in the middle of the contact. A maximum of the von Mises stresses is found at a depth of ≈ 60 μm. Nevertheless, the yield strength of the materials (662 MPa (Lee/Uhlig, 1972)) is exceeded till a depth of approximately more than 250 μm. The distribution almost matches the expected Hertzian stresses since the frictional influence is low (friction coefficient). Figure 4.35 shows the lateral (x/y) von Mises stresses at a plane matching the surface with the horse-shoe shape distribution of the stresses in the contact region. At the surface plane, the yield strength is exceeded up to approximately the edge of the contact region. Due to the moving contact, a distribution of stresses in sliding direction can also be seen as the stress development for a discrete point by time.

4.3 Wheel-rail tests

So far, the focus of this work was rather fundamental research. However, another aspect of the investigations was to gain a set of analysis methods to deal with tribological questions emerging from applications. Additionally, the previously gained information about the strain formation in ferritic-pearlitic steel is also meant to be applied to real applications.

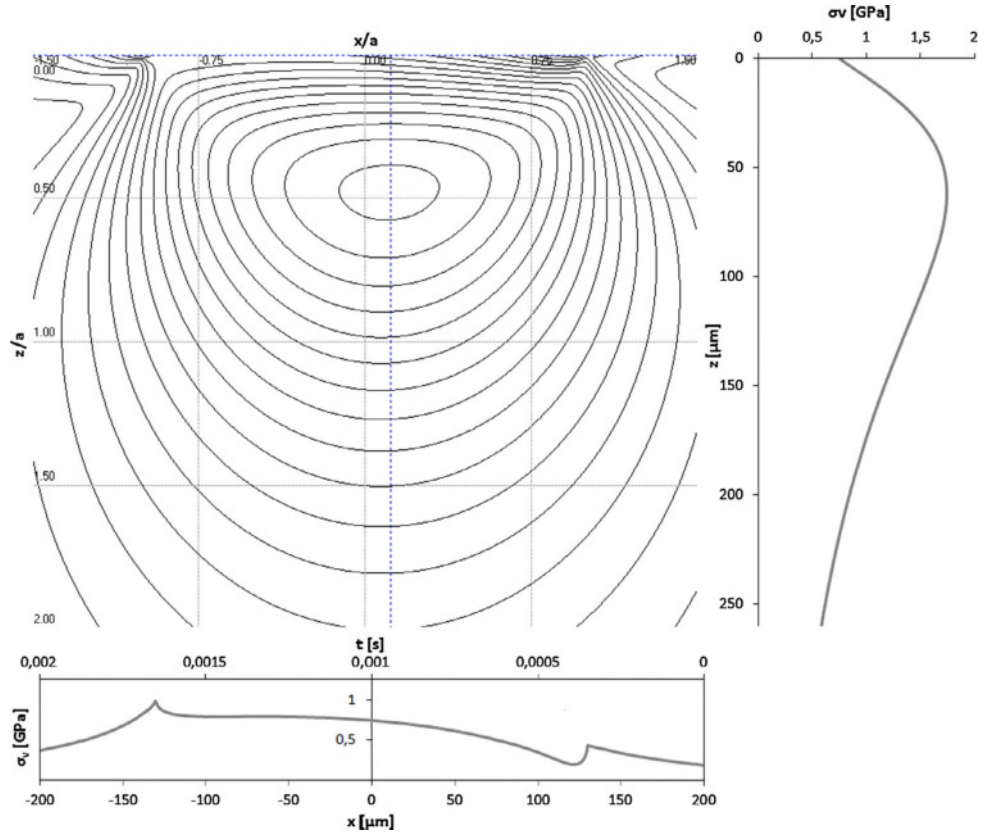

Figure 4.34: Von Mises stresses in cross section (longitudinal). The stress values for the vertical dotted line (through maximum) are plotted on the right. The stress values for the surface is plotted on the bottom and correlated with time. Contact moves from left to right.

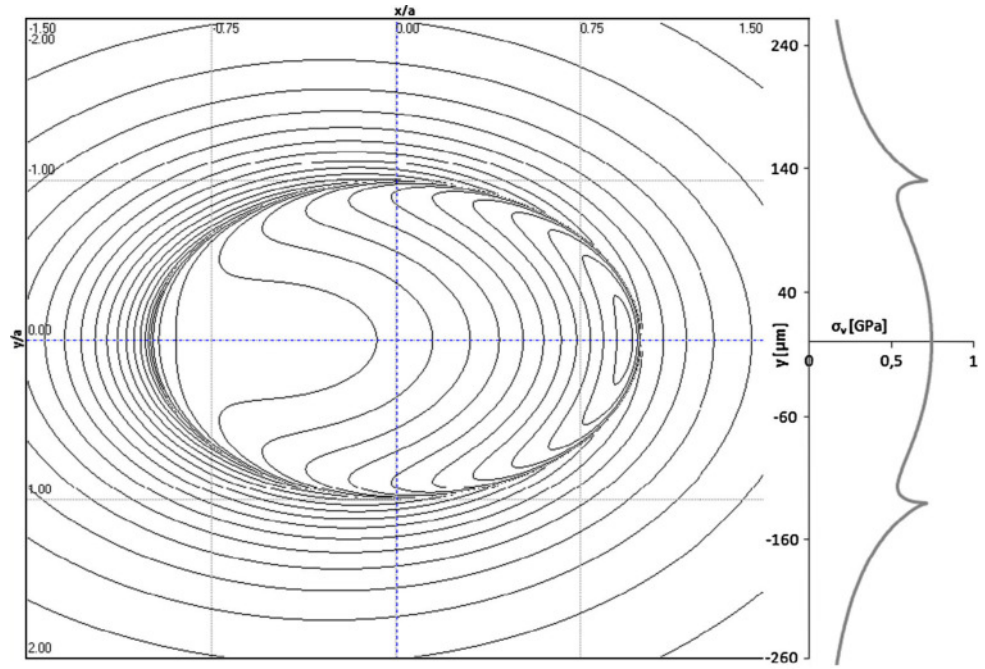

Figure 4.35: Von Mises stresses in lateral plane situation (at the surface). The stress values for the vertical dotted line are plotted on the right. Contact moves from left to right.

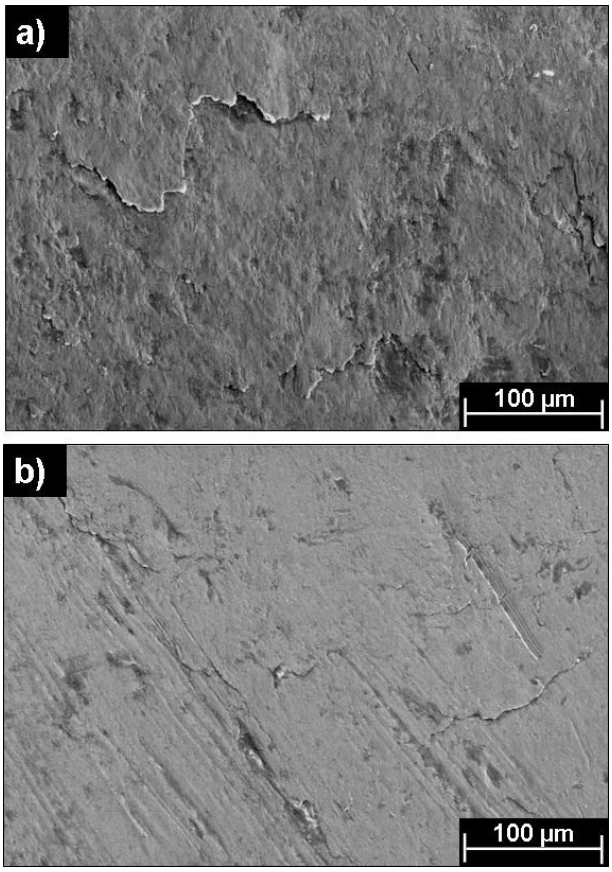

Figure 4.36: SEM image of a typical surface wear zone after 4 000 cycles: (a) as delivered R260 steel and (b) surface finished R260 steel (rolling direction from bottom to top).

Still a severely examined application is the well-established wheel-rail contact. Especially, the material responses in railways operated in train applications are of high importance. However, to get defined testing conditions the wheel-rail contact was simulated in a set-up in the laboratory. Due to the similar geometries of the rolling-contact compared to real wheel-rail applications, the here presented results represent the real application as close as possible on lab scale. The results aim at a fundamental understanding of the influence of the microstructure on the occurrence of flake-like spalling sites in wheel-rail contacts. Therefore, ferritic-pearlitic steel is compared to pure pearlite. The first subsection gives a general overview of the development of the microstructure and the hardness beneath the surface. As in the previous sections of sliding results, strain related material values are used to characterize the plastic deformation of the material.

4.3.1 Wear surface and loaded sub-surface zones

The worn surface of the as delivered R260 steel shows spalling occurring in the region close to the edge where the highest slip is expected (figure 4.36a). Surface roughness may initiate the formation of flakes in the early-damage regime. The flake opening is facing backwards to the rolling direction due to the curvature of the contact geometry.

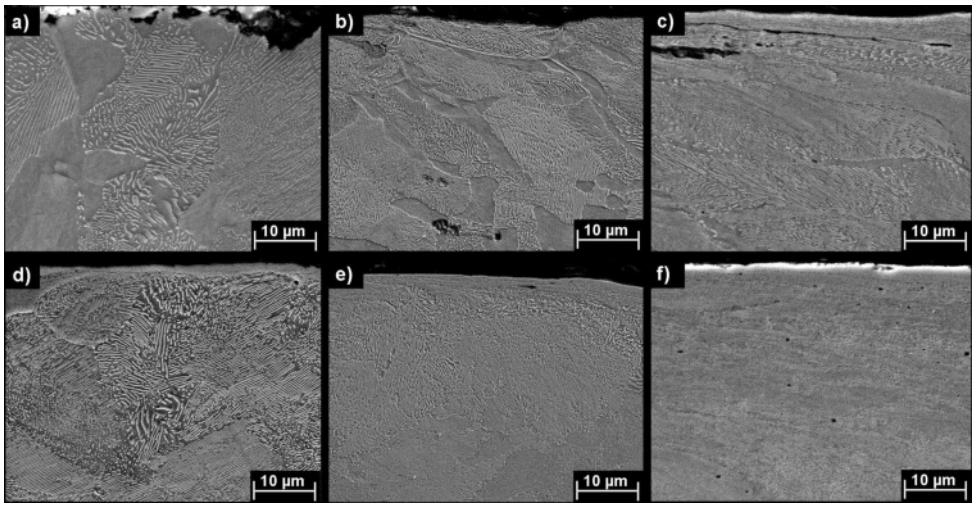

Figure 4.37: SEM of typical longitudinal sections of R260 steel: (a) reference of as delivered, (b) as delivered after 100 cycles, (c) as delivered after 4 000 cycles, (d) reference of surface finished, (e) surface finished after 100 cycles and (f) surface finished after 4 000 cycles (rolling direction from left to right).

Consequently, the slip is also pointing backwards to the position of highest stresses. The flakes appear more pronounced in the as delivered samples than in the surface finished ones (figure 4.36b). Moreover, the surface finished sample shows a smoother surface in the loaded region. The initially rolled sample preserved its uneven surface during the first thousand cycles. Nevertheless, the flake appearance is the same for both types of samples, but the flakes stick out more on the rolled unfinished surface.

The longitudinal cross-section of the as delivered, initially rolled rail reveals high ferrite content caused by decarburization (figure 4.37a). In contrast to that, the milled sample shows an almost pure pearlitic microstructure with a plastically deformed and modified layer very close to the surface in the initial condition, which originates from the surface finishing step (figure 4.37d) (Kapoor et al., 2002). With increasing number of rolling cycles, the as delivered sample develops a steady increase of plastic deformation as shown by the modification of the grain shape in figure 4.37b and 4.37c. This results in a tilting of the grain structure near the surface in slip direction (backward to the rolling direction). The maximum tilting seems to be reached by grains at the surface, which appear to be aligned parallel to the contact surface. Besides, surface flakes grow in length as the number of cycles increase. Their growth follows the layer-like structure of the tilted and smeared grains (figure 4.37c). Within the as delivered sample tilted grain boundaries can be found in relatively large depth of up to 40-50 µm, even after very low number of cycles (100). In contrast to the rough ferritic-pearlitic samples, the surface finished samples only show a morphologically modified zone very close to the surface (depth of 4 µm, 100 cycles), where the grains cannot be resolved anymore (figure 4.37e). Moreover, the degree of tilting of the grain structure appears to be less pronounced than in the as delivered

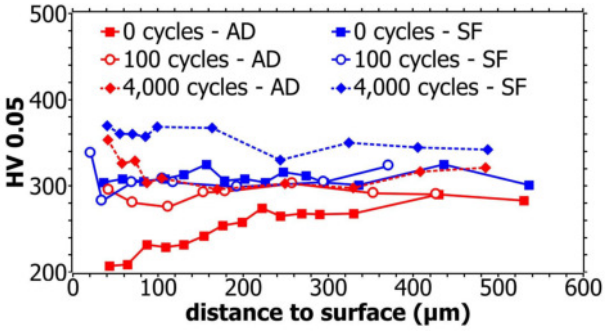

Figure 4.38: Hardness values as a function of distance from the surface for as delivered (AD) and surface finished (SF) R260 steel for different loading cycles.

samples. Nevertheless, between 100 and 4 000 cycles, the material undergoes plastic deformation in a zone with a significant increase in depth greater than >50 µm from the loaded surface at 4 000 cycles (figure 4.37). Thus, the cyclic plastic deformation response of the as delivered samples is dominated by tilting of the grain structure and following crack initiation and propagation (figure 4.37c) whereas the surface finished samples mostly show an increase in plastic deformation (figure 4.37f).

For the quantification of the plastic deformation by means of hardness, HV0.05 hardness profiles were performed from the deformed near-surface zone into the bulk of R260 steel (figure 4.38). The initial lower hardness of the as delivered reference sample is caused by the high ferrite content in the near-surface zone compared to the fully pearlitic surface finished sample. Moreover, the as delivered sample shows a significant increase in the hardness from the reference surface of ≈ 200 HV0.05 to ≈ 300 HV0.05 (after 100 cycles) to a value of ≈ 350 HV0.05 (after 4 000 cycles). The modified region was observed from the surface to a depth of ≈ 100 µm. In contrast, the surface finished sample (SF) shows almost no hardness change between the unloaded reference and the near-surface zone after 100 cycles. Both samples show hardness values of ≈ 300 HV0.05. Nevertheless, after 4 000 cycles, the hardness value exceeds 350 HV0.05 down to a depth of ≈ 200 µm beneath the loaded surface.

4.3.2 EBSD study of sub-surface deformation

In order to characterize the deformation of R260 steel, three different plots were used: (i) the inverse pole figure (IPF) for a visualisation of the structure of lattice domains (grains); (ii) a combined plot of pattern quality and grain boundaries (LAGB and high-angle grain boundaries (HAGB)); (iii) kernel average misorientation for the intergranular deformation. The EBSD plots of the as delivered reference samples are shown in figure 4.39a-c. The IPF plot (figure 4.39a) shows no significant distortion in the lattice since it represents only grains without internal orientation (colour) changes. Neither a significant formation of grain boundaries (figure 4.39b) nor a strong misorientation (figure 4.39c) is visible. This

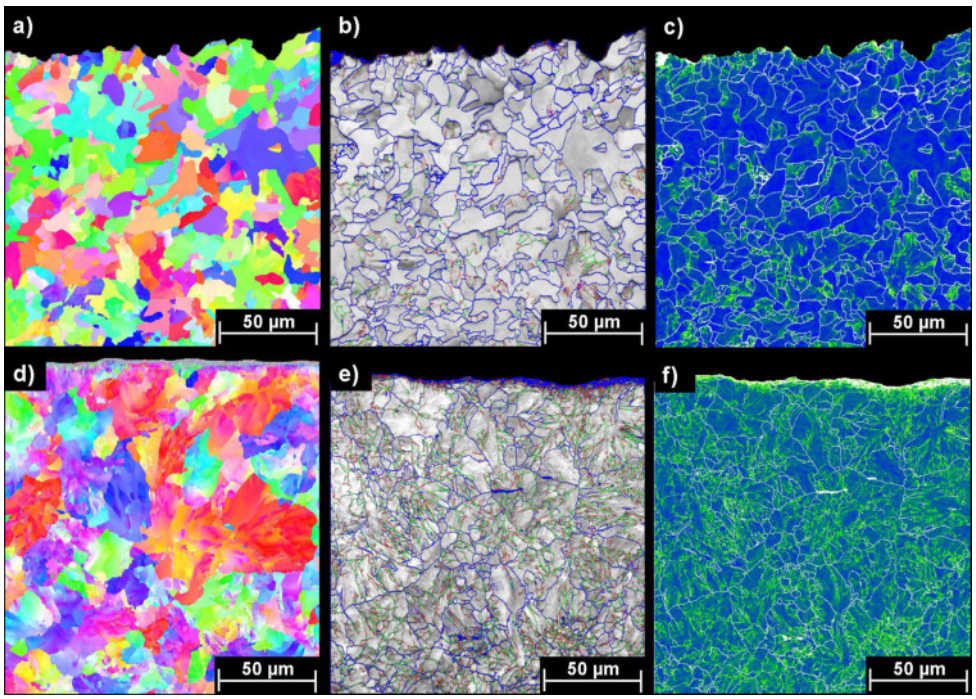

Figure 4.39: Hardness values as a function of distance from the surface for as delivered (AD) and surface finished (SF) R260 steel for different loading cycles. Sub-surface EBSD plots for unloaded R260 steel: (a) inverse pole figure (IPF) as delivered state, (b) pattern quality plot combined with grain boundaries (red lines for LAGBs of 2<5°, green lines for LAGBs of 5<15° and blue for 15° HAGBs) as delivered state, (c) kernel average misorientation (KAM 2nd neighbourhood, rainbow-scale from 0° to 5°) as delivered state, (d) IPF surface finished state, (e) pattern quality plot combined with grain boundaries surface finished state and (f) KAM surface finished state.

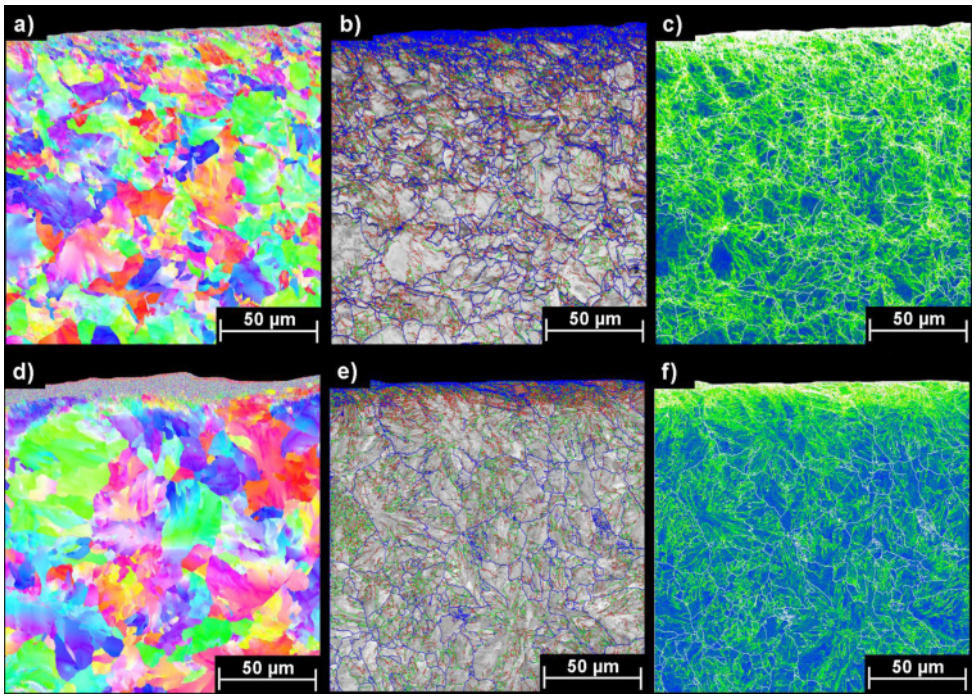

Figure 4.40: Sub-surface EBSD plots for R260 steel after 100 rolling cycles (rolling direction from left to right): (a) inverse pole figure (IPF) as delivered state, (b) pattern quality plot combined with grain boundaries (red lines for LAGBs of 2<5°, green lines for LAGBs of 5<15° and blue for 15° HAGBs) as delivered state, (c) kernel average misorientation (KAM 2nd neighbourhood, rainbow-scale from 0° to 5°) as delivered state, (d) IPF surface finished state, (e) pattern quality plot combined grain boundaries surface finished state and (f) KAM surface finished state. Note the undetectable region directly underneath the surface (varicoloured in (d), blue in (e) and white in (f)).

might result from annealing processes in the surface during multi-pass rolling. Moreover, the pattern quality distribution (figure 4.39b) shows a good sample preparation up to the edge of the sample. The IPF plot of the surface finished sample (figure 4.39d) shows a significant difference in the internal appearance of grain orientation already in the initial condition prior to tribotests. Additionally, a pronounced difference of LAGB distribution (figure 4.39e) and misorientation (figure 4.39f) can be observed with the detected EBSD scan.

The locally concentrated misorientation might be attributed to mechanical stresses introduced by the milling process of the surface finished samples. After 100 cycles, the EBSD plots of the as delivered sample (figure 4.40a-c) show that the material has undergone considerable plastic deformation. The IPF plot (figure 4.40a) shows the tilting effect of the orientation domains (grain structure) in the direction of the shear slip and backwards in regard to the rolling direction. Additionally, within the grains an internal orientation change can be observed after 100 cycles. Compared to the reference condition, the grain boundary plots and the KAM plots illustrate an increase of LAGB (figure 4.40b) as well as local misorientation (figure 4.40c). The plots of the surface finished sample (fig-

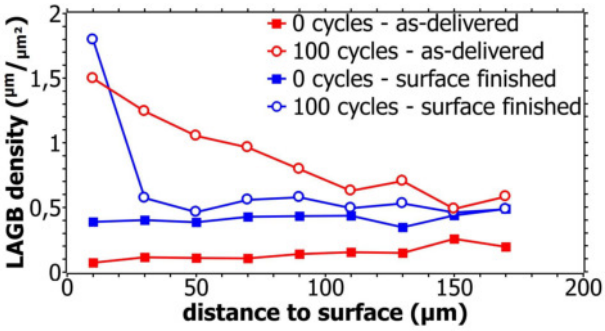

Figure 4.41: Density of LAGB (2–15°) as a function of the distance from the loaded surface for reference and after 100 cycles.

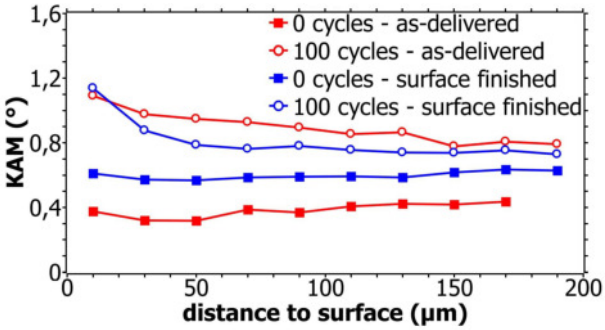

Figure 4.42: KAM for unloaded reference surface and loaded with 100 cycles as a function of the distance from the loaded surface.

ure 4.40d-f) show a thin zone at the contact surface approximately 20 μm (see figure 4.40d) that cannot be resolved by EBSD due to too high internal strains prior to the tribotest as well as after 100 cycles. Here the extremely high plastic deformation resulted in a pseudo-amorphous state for the diffracted electrons. Therefore, a correlation between the generated Kickuchi patterns to a cubic lattice is not possible in this region. Due to the rolling contact, this surface-near zone appears to increase slightly in thickness, but remains well defined with a clear borderline to the bulk microstructure beneath. The majority of the microstructure of the machined sample in the area covered by the scan revealed no significant change compared to the initial condition prior to the rolling tribotests. Neither the LAGB plot (figure 4.40e) nor the misorientation plot (figure 4.40f) shows a significant change compared to the reference state. For a quantitative characterisation, the information of the grain boundary maps as well as the KAM maps were plotted as a function of distance to the tribologically loaded surface. Figure 4.41 shows the quantitative values for LAGB density distribution in the as delivered and surface finished samples prior to rolling tests and after 100 cycles (see figure 4.39b, e and figure 4.40b, e). This plot indicates that the LAGB density increased after 100 cycles for the as delivered samples while the density was almost unchanged for the surface finished samples. This finding is confirmed by the quantitative analysis of the misorientation maps based on the 2nd KAM values (figure 4.42). The figure sharpens the visual impression of the 2D misorientation

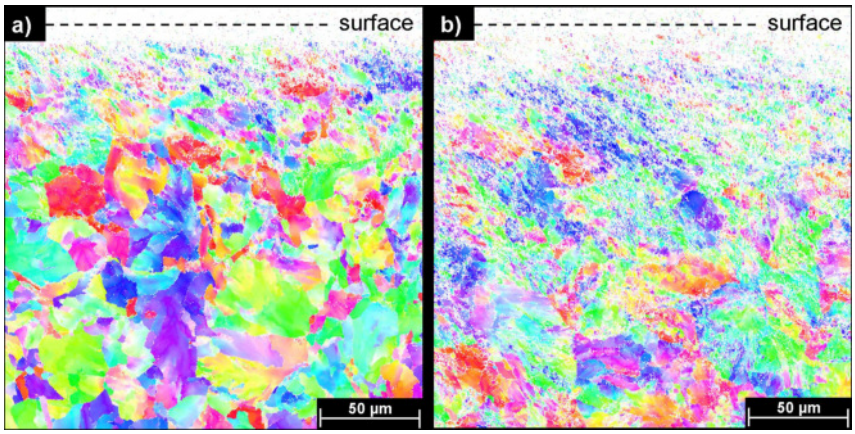

Figure 4.43: EBSD plot (inverse pole-figure) of a typical plastically deformed near-surface rail zone after 4 000 rolling cycles: (a) as delivered and (b) surface finished R260 steel (rolling direction from left to right).

maps and clarifies that an increase of the KAM values took place after 100 cycles in the as delivered sample but not in the surface finished sample, which is purely pearlitic. A qualitative comparison of the two differently pre-treated samples of R260 steel is given in figure 4.43 via the 200 x 200 μm^2 orientation plot (IPF) after 4 000 rolling cycles. The as delivered sample shows a bulk-like homogeneous grain morphology with no preferred grain orientation in a distance of 100 μm under the surface and underneath. In the region beneath the surface down to 100 μm pronounced grain deformation occurs. The surface finished sample shows a more expanded zone with strongly deformed grain structure up to 200 μm and beyond. Nevertheless, the surface finished sample showed no cracks or spalling within the studied longitudinal-section and a much lower number of spalling on the top view of the wheel-rail contact area compared to the as delivered sample surface that shows a high flake density on the top view.

Chapter 5

Discussion

Now that the outcome of the tests is known, the impact of the results needs to be discussed. The first section will explain the relation of strain formation regarding the phases as well as the change of strain initiation by increasing number of cycles. The second section will discuss the strain initiation by different viscosities. Thereby the competition between plastic deformation and wear is explained regarding the development of strain and the results are discussed regarding the lubrication conditions. Samples subjected to bidirectional sliding showed a complete different damaging at the surface. Since the effect is rather close to the surface, a strain analysis[1] did not show any explanation. The crack initiation is therefore discussed by XRD results measured with penetration depth of a couple of micrometer and thus in the range of the size of the found cracks. The last section discusses the results of the rolling tests and its impact on wheel-rail applications. Hereby, the difference between ferritic-pearlitic and pure pearlitic rails is explained regarding the possibilities of flake-like spalling which might develop as a crack initiation site.

5.1 Evolution of strain in ferritic-pearlitic steels

The analysis of the grain lattice misorientations/GND density, LAGBs density and grain refinement of the ferritic phase shows the evolution and spread of plastic deformation as a function of the number of cycles (see figure 5.1). With increasing number of cycles microstructural evolution proceeds with decreasing rate. The evolution rate of the total LAGB length and density of GND is summarized in table 5.1. The table shows the incremental increase of LAGB as well as GND density between the measured intervals. As the strain rate decreases, the plastic deformation tends to saturate.

The decrease in residual strain per cycle can be explained by an increase in the yield strength in the ferritic phase due to strain hardening as well as Hall-Petch strengthening due to grain refinement. The comparison of the LAGB and GND density between 10^5

[1] results did not show any new information and are therefore not presented in this work

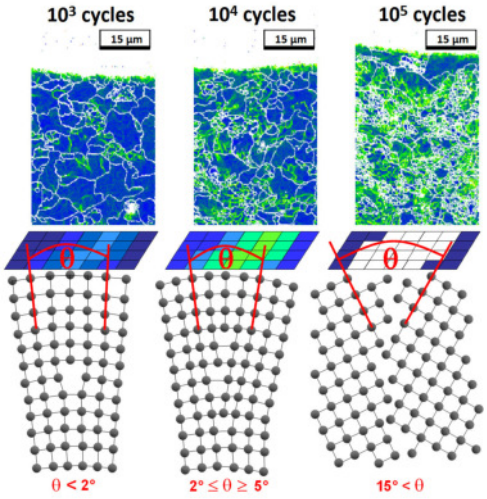

Figure 5.1: Schematic representing the sub-surface damage evolution as a function of cycle numbers correlated with the respective KAM maps.

Table 5.1: Increase in LAGB and GND densities vs. cycles.

	LAGB density (μm/μm^2)	GND density (m^{-2})
10^3 cycles	0.15	$4 \cdot 10^{14}$
Increase per cycle	$38.9 \cdot 10^{-6}$	$1.1 \cdot 10^{10}$
10^4 cycles	0.5	$5 \cdot 10^{14}$
Increase per cycle	$7.7 \cdot 10^{-6}$	$0.2 \cdot 10^{10}$
10^5 cycles	1.2	$7 \cdot 10^{14}$
Increase per cycle	0	$-3.3 \cdot 10^{7}$
10^6 cycles	1.2	$6.7 \cdot 10^{14}$

and 10^6 cycles highlights that the plastic deformation tends to saturate. This saturation is also known to occur in metallic materials deformed by severe plastic deformation such as by high-pressure torsion (HPT) or equal channel angular pressure (ECAP). Pippan et al. (Pippan et al., 2010) described this microstructural saturation as an equilibrium in the generation and the annihilation of defects: vacancies, dislocations, and high- as well as low-angle boundaries. In general, the final grain size depends on temperature, presence and density of impurities and alloying elements as described by Pippan et al. (Pippan et al., 2010) and can be further reduced in case of dual or multi phase materials (Pippan et al., 2006). Compared to the work of Pippan et al. (Pippan et al., 2006; Pippan et al., 2010), the final grain size in the presented work is of larger order of magnitude. However, even some authors have reported on the analogy between sub-surface microstructures after sliding contact and those typically found after severe plastic deformation processes (Moshkovich/Lapsker/Rapoport, 2013), the degree of deformation imparted by sliding contact within the present work is expected to be significantly lower compared to them, as highlighted by the coarser final grain size. One of the achievements of this work is the segmentation between the strain influence of pearlite and ferrite, respectively. In contrast to the work of Peranio et al. (Peranio et al., 2010), the pattern-quality-based segmentation did not work for the here presented results. Besides the presence of cementite also the crystal defects (e.g. by introduced strain) lower the pattern quality. Moreover, not even the reference material shows a clear pattern-quality-based or confidence-index based separation between ferrite and pearlite grains of similar values. For that reason, the resulting information is a combination of two effects, and segmentation is not possible in the strained samples discussed here.

However, optical microscopy segmentation on an etched cross-section of the previous EBSD measurement was more successful. The histogram (figure 3a) showed the two expected phase regions. Thus, a masking by grayscale values enabled to separate between ferrite and pearlite and to combine this masks with EBSD measurements of the same region. The masks are in good agreement with the optical micrograph as the overlay reveals (as shown in figures 3b to 3e).

As the analyzed steel is composed of two phases (ferrite and pearlite) a phase specific mechanical response under sliding contact stresses was expected. Since the segmentation by quantitative information (pattern quality and confidential index) was not suitable, the segmentation was performed by qualitative masking of each crystallographic phase. The IPF plots masked for each phase indicate that the refined grains are predominantly ferritic, while pearlite remains undeformed below the wear track. Moreover, a larger lattice misorientation is predominantly found in the ferritic phase below the wear track. Both phases, ferrite and pearlite have a BCC crystallographic structure, which is the major difference between them with cementite lamellae present in the latter thus resulting in superior mechanical properties. First of all, the microstructure composed of alternat-

ing ferrite and cementite lamellae lead to a composite structure, which renders a higher hardness and yield strength when compared to individual ferrite grains. Furthermore, dislocation motion in pearlite is confined by the interlamellar spacing; therefore, higher contact stresses would be required to promote strain. With our selected sliding contact conditions, ferrite accommodates most of the plastic strain, behaving as a sacrificial phase, until grain refinement and dislocation density saturate. The results obtained by the EBSD segmentation of grain-refinement in the ferrite and the rather stable pearlite phase are supported by the higher resolution TEM and TKD analysis. The investigated tilted lamella prepared in a shallow angle with respect to the tribologically tested surface confirmed that grain refinement was limited to the ferritic phase, resulting in refined equiaxed grains.

Grain refinement, increase in LAGB and GND density leads to a rise in hardness for larger number of sliding cycles. Moreover, the work hardened microstructure extends deeper into the material at regions further below from the surface. In a ferritic-pearlitic microstructure work hardening is expected to occur faster than in a related single phase ferritic alloy, according to Ashby (Ashby, 1970). Ashby further highlighted the appearance of deformation gradients in the softer phase due to formation of GNDs (Ashby, 1970; Ankem et al., 2006). Besides the formation of GND (Ankem et al., 2006; Gottstein, 2007), SSDs might also be expected to contribute to the rise of hardness (Alkorta/Martinez-Esnoala/Sevillano, 2006). Therefore, even SSDs were not taken into account in the present work since they are not visible by EBSD as they are expected to play a secondary role in the hardness increase(Alkorta/Martinez-Esnoala/Sevillano, 2006). Tabor (Tabor, 1970) linked the hardness directly to the yield stress by a factor of 3, allowing for the estimation of macroscopical mechanical properties using indentation measurements. However, the exact correlation between hardness and yield stress is still a matter of debate (Tabor, 1996). In contrast to calculating the overall yield stress according to Tabor, the mechanical properties were calculated for each single phase according to the work of Allain and Bouaziz (Allain/Bouaziz, 2008). This shows, that the ferrite phase undergoes a significant increase in yield stress, due to grain refinement and Hall-Petch relation. In contrast to the pearlite with its higher yield strength, the ferrite yields much earlier. However, with the development of grain refinement, the ferrite withstands the externally applied stresses more efficiently due to the increased yield stress thus leading to a saturation by means of plastic strain hardening.

Incompatibilities at the grain boundaries between the ferrite and pearlite provides a potential site for the accumulation of GNDs and the appearance of strain gradients (Ashby, 1970; Ankem et al., 2006). However, neither of the EBSD plots revealed a systematic preference for strain accumulation at the interface between pearlite and ferrite. Jeong et al. (Jeong et al., 2014) compared the strain formation in ferritic-pearlitic steels with ferritic-martensitic dual-phase steels. Contrary to dual-phase steels, they also found

no evidence for strain concentrations at ferrite-pearlite interfaces after plastic deformation by analyzing EBSD pattern quality. Though, the here presented TEM results reveal the occasional formation of dislocations pile-ups at the interface between pearlite and ferrite grains, the size of the pile-up regions due to phase incompatibilities is rather in the nanometer scale (approximately 200 nm). Despite the lack of experimental evidence for strain concentrations at the boundary between ferrite and pearlite, strain localization at ferrite-pearlite interfaces was recently described by Berisha et al. (Berisha et al., 2015) based on Crystal Plasticity Finite Element Method (CPFEM) simulations. Therefore, it seems that the gradients of deformation depend on the strength ratio of the two phases. This explains the difference between the occasional localized strain regions found for ferrite-pearlite in the present work when compared to larger regions of strain gradients identified in dual phase steels by other authors (Jeong et al., 2014). The appearance of dislocation pile-ups at the ferrite-pearlite interface might well become a potential source for crack nucleation and initiation. Narasaiah and Ray (Narasaiah/Ray, 2005) investigated the formation of voids and cracks in ferritic-pearlitic steels. They found interface cracks more likely (approximately 10 times) to appear at ferrite-pearlite interfaces than at other crack initiation sites. The relevance of such interface cracking between ferrite and pearlite is also known on larger length scales from railway steels (Eden/Garnham/Davis, 2005). Microstructure evolution and crack propagation in ferritic-pearlitic steels in the context of rail tracks has been a subject of extensive research (Ringsberg/Loo-Morrey, 2000; Eden/Garnham/Davis, 2005). However, the appearance of near-surface cracks called "head checks" as a consequence of mixed rolling-sliding contact fatigue is not fully understood yet. The present work provides new aspects that could contribute to enlight the origins of near-surface cracks in ferritic-pearlitic materials under sliding contact conditions.

5.2 Competition between plastic deformation and wear under boundary condition

The present work highlights the competition between plastic deformation and wear in sliding contacts operating in boundary lubrication. The investigations were performed using two normal loads and lubricants, both of them having an order of magnitude difference in their values. The difference in load and viscosity changes the Sommerfeld number and, consequently, shifts the tribosystem along the x axis of the Stribeck curve. Despite these changes, it was assured that the tribosystem operates under boundary lubrication for all combinations of load and viscosity evaluated.

The use of different viscosities in boundary lubrication conditions leads to different surface degradation mechanisms. The use of a higher viscosity leads to a higher sur-

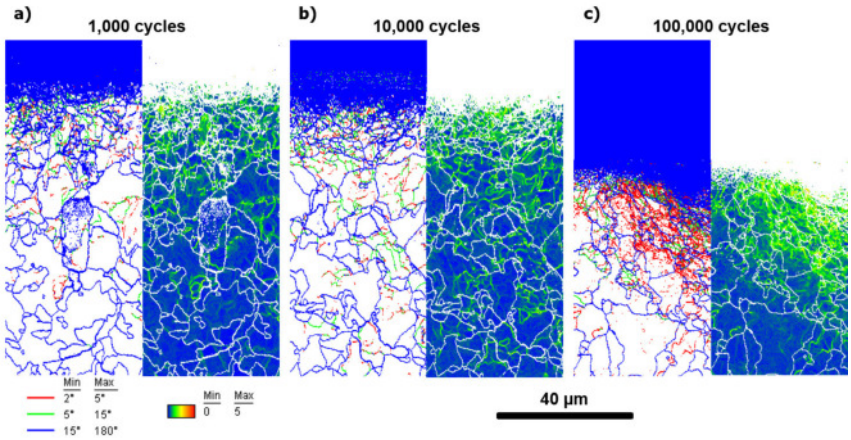

Figure 5.2: Evolution of surface near strain of FVA1 lubricated samples. The vertical position of the plot are in relation to the initial surface before the tribological testing.

face protection and reduces the removed wear volume, as can be expected. A higher viscosity results in a lower friction coefficient than a higher viscosity, while keeping all other parameters constant. Additionally, the volume of the side ridges after sliding contact is comparable to the removed wear volume. This leads to the conclusion that most of the degradation occurs by ploughing as a consequence of plastic deformation, where detachment of wear debris by abrasive wear plays a minor role. The EBSD measurements support this assumption by revealing a higher dislocation activity. The highest microstructural activity is found in a distance from the surface where the maximum Hertzian stresses are expected. Moreover, the material at the surface interface is almost unaffected by plastic strain, resulting in an insignificant amount of abrasive wear. This surface degradation behavior is the mechanism previously assumed to occur rather under mixed, elasto-hydrodynamic or hydrodynamic lubrication.

The use of a lower viscosity under boundary lubrication yields to a steady material removal by abrasive wear with minimum formation of side ridges. Only during the initial sliding cycles - up to 1000 - side ridge formation can be observed. The missing ridges indicate that ploughing by plastic deformation plays a minor role. In this case, the EBSD analysis shows that plastic deformation is concentrated very close to the surface interface.

Subsurface cracks as a process previous to wear particle generation were not observed in any of the examined samples. Nevertheless, such cracks are not essential for the formation of wear particles (Korres/Feser/Dienwiebel, 2012). For low viscosity, plastic strain was found to be very localized at the surface indicating that surface degradation, i.e. plastic deformation and wear, is dominated by shear stresses. Under these conditions, wear can occur by steadily deforming and abrading the near-surface- material, as observed for copper by Korres et al. (Korres/Feser/Dienwiebel, 2012). Due to this steady process of surface degradation, a similar plastic deformation depth was expected for the samples with lower viscosity independently of the numbers of cycles. This is confirmed

by the comparison of EBSD measurements after different numbers of cycles as shown in figure 5.2. The figure highlights very similar strain depth for different numbers of cycles. Hereby, the shear stresses close to the surface plastically deform the near-surface region with a following weakening and subsequent abrasive detachment of material by wear debris generation, thus leading to a steady process. The results found for samples tested using low viscosity lubricant are in agreement with the results obtained for copper by Moshkovich et al. (Moshkovich et al., 2010) where the plastic deformation concentrates at the surface and the strain related values (grain refinement, LAGB and GND density) are higher for lower λ ratios. For the here tested steel samples, also higher strain related values (LAGB and GND densities) were measured for lower λ ratios but for the higher λ ratios the region of straining is larger.

The EBSD results showed the evolution of plastic strain as a function of the distance to the surface, which was found to progress according to the following sequence: (i) generation of GNDs (ii) pile-up of GNDs and formation of LAGBs (iii) evolution of LAGBs to HAGBs and thereby grain refinement of the microstructure. In the presented work, final grain sizes of approximately 1 μm were achieved. In literature, higher degrees of microstructural refinement have been reported in boundary lubrication. For instance, Meshi et al (Meshi et al., 2011) investigated the damage and strength evolution of copper for different lubrication regimes. In case of boundary lubrication, they found grain sizes ranging from 20 to 100 nm, whereas for elastro-hydrodynamic conditions the final grain size was 1 to 2 μm, with friction coefficients of 0.23 and 0.01, respectively. The difference compared to this work might arise due to higher shear stresses as a consequence of higher friction under boundary lubrication as well as due to the softer face-centered cubic copper grains. Additionally, the deformation of the individual grains is not homogeneous in the present work, since the softer ferrite grains carry most of the plastic deformation whereas pearlitic grains remain mostly undeformed.

The hardness of materials undergoing sliding contact is known to saturate after certain numbers of cycles. According to (Meshi et al., 2011), the saturation value for copper is close to the hardness of nanocrystalline copper produced by different severe plastic deformation processes. Since the rise in hardness is directly correlated with sub-surface strain hardening, the strain related magnitudes measured by EBSD should also undergo a saturation. In our case the saturation process was observed to depend on the lambda ratio: (i) for low viscosity lubrication, the microstructure saturates close to the surface due to shear stresses after a relatively low number of cycles while is constantly worn out. Thus, a steady process of plastic deformation, saturation and material removal wear is characteristic for this lambda region; (ii) In case of high viscosity lubrication, plastic strain has a higher activity in the region of largest Hertzian contact stresses and thus not directly at the surface. Due to the extremely low wear, the saturation process is only determined by the material microstructure and develops with a much higher number of

cycles $>10^5$ cycles. However, in none of the measured cases the saturation required the formation of nanocrystalline grains.

Grain refinement in sliding contacts is an important factor because it does not only determine sub-surface hardness, but also according to the work of Moshkovich et al. (Moshkovich et al., 2010), influences the transition between boundary to mixed lubrication. Thus, lower grain sizes lead to lower Sommerfeld numbers for the transition between boundary and mixed lubrication as well as lower wear rates. This effect can have an influence in the present work, since the tests performed at higher lambda values were closer to the onset of mixed lubrication. Therefore, the grain refinement caused in-situ during the sliding process can contribute to shift the boundary/mixed lubrication transition to lower sliding speeds resulting in a lubrication regime of lower abrasive wear.

Finally it should be noted that significantly different microstructures can arise even under similar lambda ratios (λ=0.62 for 20 N and λ=0.52 for 120 N both with FVA4). In the latter case a higher strain is found in a region ranging deeper into the material, when compared to the 20 N loaded samples. A similar observation was presented by Rainforth (Rainforth, 2000) for aluminum under dry contact conditions, where an increase of the load by a factor of 6.7 extends the region of grain refinement by a factor of three in terms of distance to the surface.

5.3 Evolution of surface damage in bidirectional sliding

The surface found after performed tribo-testing appears without abrasive wear. Thus, the introduced damage is not ground off from the wear track. Between 10^3 and 10^4 cycles, cracks are initiated and propagate in sliding direction. The further joining leads to a disruption of the crack regions. The found effects suggests that the crack propagation is not reaching in depth greater than 10 μm as determined by a focused ion beam milled cross-section where the crack depth was approximately 1 µm (figure 4.31). The crack propagation in sliding direction combined with the information of the residual tensile stress development transversal to the sliding direction shows that the crack initiation is caused by mode I (see figure 2.5) cracking of the surface. Thus, the outer few micrometer of sample material undergo fatigue during the cyclic stressing. Therefore, it is located approximately as deep as the penetration depth of the copper based X-ray radiation. Hence, the measurement should be sensitive for the region of fatigue damage. Since the main direction of residual stress development is found transversal to the sliding direction, the plastic deformation should be developed by the elastic pushing of the indenter ball to the outer sides of the wear track, similar to a plough pushing material to the sides. The fact that no significant residual stresses in longitudinal direction are found suggests, that the

effect of stress initiation is reversed with the reversal of the indenter in opposite direction. The difference between the two measurements might be caused by the dependency of the positioning on the sample. Thus, regions with different starting residual stress might have been hit by the two different measurement series. The decreased residual stress value at the end of both measurement series could be caused by the relaxation of the sample material by the crack opening. The undulating is expected to be an artefact, developed by plastic deformation due to shear stresses at the surface, due to the locally different mechanical properties of the alternating ferrite and pearlite microstructures. The lateral size of the region is also in the range of the grain structure of the microstructure. Through its minor importance, the undulating topography will not be further discussed in this work.

5.4 Rolling contact

Rolling contact fatigue (RCF) caused by cyclic plastic deformation is well-known to be the prior mechanism of material modification in rails that leads to crack nucleation, crack propagation and wear by break-outs. The present results show different plastic response of two sets of samples of experimentally simulated wheel-rail rolling contact. The samples represent the same nominal chemical composition and production route, but exhibited different surface roughness and phase contents in the surface near region.

The deformation of grains below the aligned layer was interpreted as a tracer/indicator for the amount of shear strain that acts in particular depths below the surface. The softer decarburized mainly ferritic microstructure can take up a larger strain increment with only a small increase of the internal stress. For the harder pearlitic phase the cementite represents an obstacle for dislocation movement and thus a larger stress increment is needed to take up the same externally imposed strain increment as the ferrite. This leads to a higher hardening in the pearlite (Movahed et al., 2009; Allain/Bouaziz, 2008), but the volume increment needed to take up the externally imposed strain is smaller resulting in concentrated microstructure deformation or increase in elastic strain, which is monitored by EBSD.

Despite the similar appearance of the aligned layers in the two sample conditions, they are expected to respond differently to the externally applied stresses. Mechanical strengthening in the pearlite grains is described by Scheriau and Pippan (Scheriau/Pippan, 2008) to be dominated by the reduction of lamellae spacing, increase of the dislocation density as well as the solution of carbon atoms from the cementite lamellae in the ferrite matrix (Languillaume/Kapelski/Baudelet, 1997; Danoix et al., 1998). Due to the high stress needed for such modifications, the cementite works as a barrier for dislocation movement in a lower stress regime. In the early stages, dislocations are described to pile-up at the lamellae interfaces until the cementite lamellae breaks and the fragments align in the

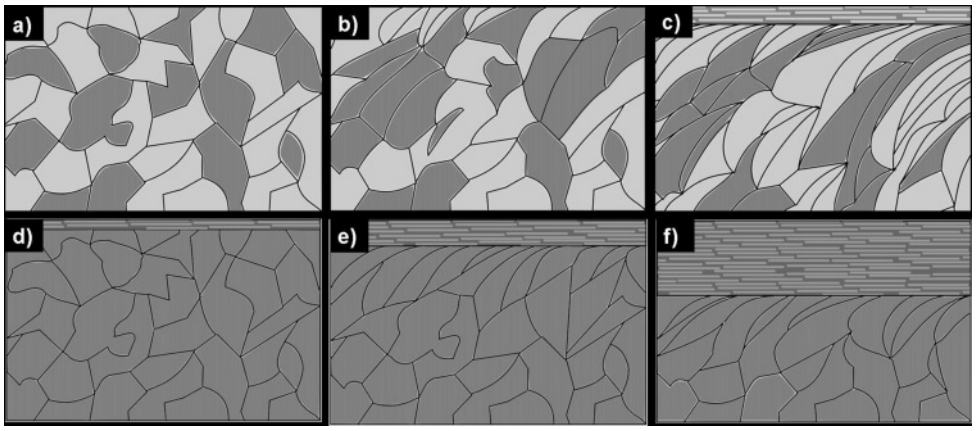

Figure 5.3: Schematic illustration of grain deformation and formation of layer-like structures in the near-surface zones for different numbers of loading cycles: (a) as delivered ferritic/pearlitic R260 steel (ferrite in light grey, pearlite in dark grey), (b) ferritic/pearlitic microstructure in very-early damage stage (100 cycles), (c) ferritic/pearlitic microstructure in early damaging stage (4 000 cycles), (d) pearlitic structure surface finished, (e) pearlite structure in very early-damaging stage (100 cycles) and (f) pearlite structure in early-damaging stage (4 000 cycles).

stress-favoured direction (Scheriau/Pippan, 2008). Thus, a high content of ferrite in the as delivered sample reduces the potential for strengthening due to the lack of cementite (Lee et al., 2010). Despite the reduced strengthening effect, the ferrite phase contains a high amount of plastic strain and consequently these highly strained ferrite bands in between the pearlite grains can act as a crack propagation path (Eden/Garnham/Davis, 2005; Garnham/Davis, 2011). This leads to a different appearance of the plastically deformed grain structure within the pearlitic microstructure and one that additionally contains ferritic grains. In a very early damage stage our model of the microstructural response is described by a schematic illustration in figure 5.3.

The plastic deformation in the as delivered sample is first visible in the morphology due the tilting of the grains. This leads to deformation of the grain shapes and the pearlite colonies inbetween follow the bending of the ferritic grains. The formation of a lamellar structure of highly deformed material, with an orientation parallel to the surface, is delayed by the proceeding transformation of the friction energy into a tilting of the grain boundaries (figure 5.3a-c). In contrast, the pure pearlitic structure of the surface finished sample cannot take up the energy in the same amount by dislocation build up and tilting of grain orientations and thus provides much inferior plasticity. Hereby, the cementite prevents the lamella structure within the pearlite grains from being bent during the early damaging regime. Depending on the orientation of the cementite, the cementite lamellae have to break in later stages in order to enable the plastic strains imposed by the external loading stresses. The fragmented parts of the lamellae can be easily aligned parallel to the loaded surface and finally form a well-defined growing layer that is perfectly parallel to the contact plane (figure 5.3d-f). Beneath this layer further bending

of the pearlite grains can be observed when performing higher numbers of cycles (Carroll/ Beynon, 2006; Kapoor et al., 2005) [25,36].

The plastic deformation in the as delivered sample can be driven by the slip of dislocations in the ferritic lattice structure while the cementite in the pearlite grains limits the mobility of dislocations and thus, decreases the plasticity. As the ferrite grains appear also in higher depths below the surface in the as delivered sample, high amounts of plastic strains can be taken up by its deformation mechanism up to depths where ferrite grains come along with pearlite colonies. As a consequence, the ferrite grains in the as delivered sample enable a larger volume of the material to respond to the external stresses down to much higher depths than in the fully pearlitic sample. Tilting of the microstructure occurs already after 100 cycles in the as delivered sample. Apparently, the decarburized region in the as delivered sample with its increased content of ferrite grains is acting as a sacrificial phase. An aligned layer of broken cementite lamellae and remains of ferritic lamellae was already found in the surface finished reference sample and was attributed to stresses exerted by the milling process. The fact that these aligned layers are always very localised close to the surface and show a clear boundary line to the underlying microstructure can most likely be explained by a steep stress gradient of the main shear component from the surface to the bulk. This layer seems to take up a very high levels of friction energy by a relatively small material volume. Consequently, very small shear strains are imposed on deeper regions and the microstructure beneath the aligned layer does not need to respond by changes of the grain morphology. With increasing number of cycles, the aligned layer in the surface finished sample is growing deeper into the material, but the grain morphology beneath is hardly or less affected independent of the layer thickness. The as delivered samples develop only a thin aligned layer and the tribological energy is rather transformed into higher grain-tilt angles as well as creation of new surfaces forming cracks eventually resulting in spalling, as seen in the SEM micrographs in figure 4.36.

A further origin for the formation of the described aligned layer is related to surface roughness, as investigated by Kapoor et al. (Kapoor et al., 2002). Kapoor et al. successfully related the evolution of the layer to micro-contacts and their shallow stress influence at the contact surface. In the current work, it is likely that the generation of the layer is influenced by the mechanisms described by Kapoor et al. since the appearance and thickness of the aligned layer are almost identical after 100 cycles for the surface finished sample as well after 4 000 cycles for the as delivered sample. As the layer thickness is further increasing (e.g. after 4 000 cycles at the surface finished sample in figure 4.37f), the influence of the roughness is expected to decrease for regimes with higher wear.

In order to quantify the degree of plastic deformation due to the tribological loading, an analysis of the LAGB density and KAM values as a function of distance from the surface was performed. The surface finished sample shows an accumulated plastic deformation in the very near-surface zone even for the reference sample. The origin of this accumulation

by sub-grain effects is caused by the initial work-hardening during the machining process. The as delivered sample experienced a distinct increase of LAGB as well as KAM values over a larger depth. The initial state of the as delivered sample shows almost no LAGBs or misorientation, respectively, but after only 100 cycles, the density of LAGBs as well as the misorientation is increased to much higher values. This increase is hardly detectable for the surface finished sample (reference and after 100 cycles). The slightly lower KAM values in the surface finished sample after 100 cycles with regard to the reference might have derived from local fluctuations in the surface machining as well as in the preparation of the investigated longitudinal-sections.

The difference in the material response to a tribological rolling contact of a fully pearlitic and a ferritic/pearlitic microstructure is even more distinct when comparing EBSD plots (figure 4.43) after 4 000 cycles. The fully pearlitic surface finished sample shows a layer-like grain refinement beyond a depth of 100 μm and the ferritic / pearlitic as delivered sample shows grain refinement only within the first 50 μm below the surface. Thus, the layer-like structure develops deeper into the material without a pronounced grain tilting in the surface finished samples. Additionally, a following deformation of this layer-like structure into a nano-crystalline material as described by Wang et al. (Wang et al., 2003a) is possible.

The as delivered samples show the development of cracks by spalling which is more pronounced than in the surface finished samples. The cracks, separating flakes from the surface, grow along the lamellar structure of the deformed grains in the same orientation as the grain boundaries. Thus, it is expected that cracks grow along the grain interfaces. Besides a fatigue related crack initiation at the surface, the cracks might also originate from severe plastic deformation of surface asperities. Thereby, the asperities are severely sheared on the surface and build cavities (including oxide/wear debris).

Chapter 6

Conclusion

Strain accumulation in a ferritic/pearlitic steel was studied for unidirectional and bidirectional sliding under boundary lubrication as well as unlubricated rolling, simulating a whee-rail contact. Apart from hardness measurements, electron backscatter diffraction was used for quantitative description of strain formation by means of misorientation, low-angle boundary density as well as grain refinement. The study of strain involved the dependency on the number of cycles, lubrication conditions as well as normal load. In case of rolling, the study of strain formation was used to compare the strain formation in a ferritic/pearlitic steel versus a pure pearlite. The EBSD results allowed the development of a model describing the plastic deformation of the two different steels and furthermore an understanding of its influence on flake-like spalling which might result as crack initiation sites. Since a comparison of the resulting strain did not show a significant difference between unidirectional and bidirectional sliding, a further study of strain formation in bidirectional sliding was not performed for this work. In contrast to unidirectional sliding, longitudinal crack initiation occurred in bidirectional sliding which was investigated by XRD residual stress measurements.

The work was performed in order to find answers to a set of specific questions emerging from the field of tribology. This chapter summarizes the discussed results in order to answer the questions mentioned in the introduction:

- How does the strain in the material evolve with increasing numbers of cycles, especially for the case of low material loss due to wear?

For specific distances underneath the wear track surface, GND densities are calculated based on orientation gradients (kernel average misorientation) for different cycle numbers (10^3, 10^4, 10^5 and 10^6 cycles). The strain formation per cycle shows higher incremental formation of strain earlier during the testing, while the density of GNDs, low-angle grain boundaries and grain refinement saturated between 10^5 and 10^6 cycles. The determined strain correlates well with measured hardness values. Thereby, the hardness increases from 250 HV for to 300 HV after 10^5 sliding cycles. Due to the saturation of strain

formation and the higher hardness combined with a widening of the contact width, the influence of the sliding contact on the material becomes more and more insignificant.

- How do the to phases of the ferrite-pearlite steel participate in the strain evolution?

One major achievement of this work is the successful correlation of different microscopical techniques. Thus, it allowed the combination of a segmentation between pearlite and ferrite by optical microscopy on an etched cross-section with qualitative strain information by EBSD imaging. Combined overlays of EBSD, TEM and TKD were used in a similar way for a segmentation for higher resolution imaging. While the pearlite phase only shows a minor response concerning the evolution of strain, increased GND and LAGB densities as well as grain refinement are mostly found in ferritic grains. Therefore, most of the plastic deformation was carried by the ferritic phase. A model by Alain and Bouaziz was used to calculate stress-strain curves (also including yield strength) for ferrite in the origin state as well as grain refined and the pearlite phase separately. The calculations clearly proved the statement that most of the plastic deformation was carried by the ferritic phase while the yield strength of the ferrite phase increased from 200 to 700 MPa. Thus approaching mechanical properties of the pearlite phase.

- How will the inhomogeneous material properties between the phases influence each other?

Random formation of dislocation pile-ups were found at the interface between pearlite and ferrite grains. It appears that the formation of dislocation pile-ups is predominantly found at the interface between the two phases. Due to the limited sample region available for investigation by TEM, the results might not be meaningful by themselves. However, the results obtained in this work are in agreement with simulated results by other authors and similar to strain formations described for dual phase steels.

- What is the difference between tribological contacts lubricated with higher as well as lower viscosity oil concerning the strain evolution? Furthermore, can the macroscopic wear effects be correlated and explained with the strain evolution?

The competition between plastic deformation and wear during surface degradation was investigated for different boundary lubrication conditions. It turns out that smaller lambda ratios lead to surface near strain concentrations due to shear stresses. Thereby, the surface material is weakened followed by wear. The relation between wear and strain formation stays constant resulting in a constant size of the plastic deformed zone underneath the surface with increasing number of sliding cycles. For higher lambda ratios the plastic deformation is dominated by the Hertzian stresses. Therefore, the strain is concentrated at a depth from the surface where the highest Hertzian stresses are expected.

- Bidirectional sliding contacts are known to show different wear mechanisms than unidirectional sliding contacts. How can the wear effects in bidirectional sliding be explained?

Surface investigations for bidirectional sliding show no significant abrasive wear in the wear track. However, cracks develop at 10^4 cycles. Tensile residual stresses transversal to the sliding direction develop in the wear track even during the first 10 cycles explaining the crack formation longitudinal to the sliding direction.

- Can the methods be applied to an actual application? Such as: how does the microstructure influence the strain evolution of a railway track and how does it influence its wear during operation?

The characterization of two rail steel conditions shows a substantially different plastic response during early-stage damaging of a rolling contact. Compared to real rail applications, the highest stress is expected to reach deeper into the rail material than for the experimental setup. Therefore, these results do not fully represent an experimental simulation of rail wear mechanism, but provide an understanding of damage mechanisms in early rolling contact for industrially used material conditions.

The plastic response of the as delivered decarburized pearlitic R260 steel is dominated by tilting the grain structure after only 100 cycles due to the presence of softer ferrite grains. The pearlitic, surface finished (machined) R260 steel shows no pronounced tilting of the grain boundaries. The microstructure mainly deforms by the formation of a lamellar layer increasing in thickness as the loading cycles increase. Based on the presented findings, a schematic model was set-up describing deformation and surface-layer formation of a pearlitic and a ferritic/pearlitic microstructure in a tribological rolling contact.

With the proven feasibility of the combination of EBSD with other imaging techniques one has to be cautious about the limits of the respective techniques. As shown in the here presented work, especially quantitative characterizations by EBSD are limited by the amount of plastic deformation as e.g. shown for the performed sliding tests with 420 N as well as wheel-rail tests with 4 000 cycles.

Chapter 7

Outlook

With the completion of the here presented work, some ideas are still open for a further continuation of this work, which are given in this section.

A comparison between the ferritic/pearlitic strain formation and mechanical properties with pure ferritic as well as pure pearlitic steel is only performed by calculated values based on an established model. Nevertheless, an experimental comparison might also turn out fruitful for a further understanding of the plastic deformation of the two phases during sliding. Pure pearlite might be particularly interesting in this context. Without a sacrificial softer phase, the deformation must take place in the pearlitic phase, only. As the model by (Allain/Bouaziz, 2008) uses the intelamellar spacing for calculating the mechanical properties, the heat treatment of the pearlitic steel should have a major influence on the mechanical response of the material against sliding introduced stresses. A further study of mechanisms like lamellae breaking by high-resolution techniques could be mandatory for such studies.

As mentioned before, strain measurements by means of EBSD did not show significant differences for bidirectional sliding in contrast to unidirectional sliding. Therefore, the EBSD strain measurements for bidirectional sliding are not included in this work. However, a larger set of measurements focusing at the surface near region might show important differences. Since the unidirectional worn surface shows a very different appearance compared to the bidirectional stressed wear track surface. In addition, a comparison of residual stresses might also explain the different wear mechanisms.

The here presented work characterizes the introduced strain for GND as well as LAGB density and grain refinement separately. A further improvement could be achieved by merging these strain related material values into a single value: the stored energy. E.g. the distribution of grain boundary misorientations can be plotted as a histogram of the cumulated angle (Grimmer, 1980; Morawiec, 1995). For grains with a diameter D and the boundary energy γ, the energy stored in the material can be calculated by (Humphreys, 2001)

$$E = \frac{K_1 \cdot \gamma}{D} \tag{7.1}$$

Where K_1 is a geometric constant of ≈ 3. As an alternative, the stored energy can be calculated independently of the consideration of the grain boundaries by calculating the misorientation of each pixel according to the neighbouring pixels. Similar calculations can be performed for GND densities. However, for the sake of accuracy the density of SSDs should also be included. Especially for samples of applications involving higher temperatures and a related heat treatment of the material, such calculations can give a better comparison between strains in materials.

Concerning the rolling contact, the thesis concentrates on the initiation of strain and flake-like spalling, which might serve as a later crack initiation site. Furthermore, the here presented results should be compared with damaging phenomena such as plastic deformation and crack initiation and propagation for wheel-rail contacts at a higher number of cycles.

Bibliography

Adams, Brent L.: Orientation imaging microscopy: Emerging and future applications. Ultramicroscopy, 67 jun 1997, Nr. 1-4, 11–17 ⟨URL: http://linkinghub.elsevier.com/retrieve/pii/S0304399196001039⟩, ISSN 03043991

Akagak, T./Rigney, D.A.: Sliding friction and wear of metals in vacuum. Wear, 149 sep 1991, Nr. 1-2, 353–374 ⟨URL: http://dx.doi.org/10.1016/0043-1648(91)90385-8⟩, ISSN 00431648

Alfredsson, B: An experimental and numerical study on Contact Fatigue Initiation. Ph. D thesis, Royal Institute of Technology, Department of Solid Mechanics, Stockholm, Sweden, 1998

Alkorta, J/Martinez-Esnoala, J M/Sevillano, J Gil: Detailed assessment of indentation size-effect in recrystallized and highly deformed niobium. Acta Materialia, 54 2006, 3445–3452

Allain, S./Bouaziz, O.: Microstructure based modeling for the mechanical behavior of ferrite-pearlite steels suitable to capture isotropic and kinematic hardening. Materials Science and Engineering A, 496 2008, Nr. 1-2, 329–336, ISSN 09215093

Alpas, A.T./Hu, H./Zhang, J.: Plastic deformation and damage accumulation below the worn surfaces. Wear, 162-164 apr 1993, 188–195 ⟨URL: http://dx.doi.org/10.1016/0043-1648(93)90500-L⟩, ISSN 00431648

Ankem, S et al.: Mechanical properties of alloys consisting of two ductile phases. Progress in Materials Science, 51 jul 2006, Nr. 5, 632–709 ⟨URL: http://www.sciencedirect.com/science/article/pii/S0079642505000538http://linkinghub.elsevier.com/retrieve/pii/S0079642505000538⟩, ISSN 00796425

Archard, J F: Contact and rubbing of flat surfaces. Journal of Applied Physics, 24 1953, 981–988

Ashby, M. F.: The deformation of plastically non-homogeneous materials. Philosophical Magazine, 21 feb 1970, Nr. 170, 399–424 ⟨URL: http://www.tandfonline.com/doi/abs/10.1080/14786437008238426⟩, ISSN 0031–8086

Baba-Kishi, K. Z./Dingley, D. J.: Backscatter Kikuchi diffraction in the SEM for identification of crystallographic point groups. Scanning, 11 aug 1989, Nr. 6, 305–312 ⟨URL: http://doi.wiley.com/10.1002/sca.4950110605⟩, ISSN 01610457

Bachmann, Florian/Hielscher, Ralf/Schaeben, Helmut: Grain detection from 2d and 3d EBSD data–specification of the MTEX algorithm. Ultramicroscopy, 111 dec 2011, Nr. 12, 1720–33 ⟨URL: http://www.ncbi.nlm.nih.gov/pubmed/22094374⟩, ISSN 1879–2723

Bargel, Hans-Jurgen/Schulze, Günter: Werkstoffkunde. 8th edition. Berlin Heidelberg: Springer, 2008, ISBN 978–3540792963

Barton, Nathan R/Dawson, Paul R: A Methodology for Determining Average Lattice Orientation Substructure. METALLURGICAL AND MATERIALS TRANSACTIONS A, 32 2001, Nr. August, 1967–1975

Bayer, Raymond G: Mechanical wear fundamentals and testing. 2nd edition. New York: Marcel Dekker, 2004 ⟨URL: http://books.google.com/books?hl=en&lr=&id=Q64Kq2HlyucC&oi=fnd&pg=PR5&dq=Mechanical+Wear+Fundamentals+and+Testing&ots=nDSISwsAdV&sig=SELTdWz-LnyzkE-NGd9rJZ3lTZchttp://books.google.com/books?hl=en&lr=&id=Q64Kq2HlyucC&oi=fnd&pg=PR5&dq=Mechanical+wear+funda⟩, ISBN 0824746201

Beausir, Benoît/Fressengeas, Claude: Disclination densities from EBSD orientation mapping. International Journal of Solids and Structures, 50 jan 2013, Nr. 1, 137–146 ⟨URL: http://linkinghub.elsevier.com/retrieve/pii/S002076831200399X⟩, ISSN 00207683

Bergmann, Wolfgang: Werkstofftechnik 1. Volume 6, Carl Hanser Verlag München, 2008, 111–113

Berisha, Bekim et al.: Multiscale modeling of failure initiation in a ferritic-pearlitic steel. Acta Materialia, 100 2015, 191–201 ⟨URL: http://www.sciencedirect.com/science/article/pii/S1359645415006126⟩, ISSN 13596454

Beynon, H/Garnham, JE/Sawley, KJ: Rolling contact fatigue of three pearlitic rail steels. Wear, 192 1996, 94–111

Black, M P/Higginson, R L: An investigation into the use of electron back scattered diffraction to measure recrystallised fraction. Scripta Materialia, 41 jun

1999, Nr. 2, 125–129 ⟨URL: http://linkinghub.elsevier.com/retrieve/pii/S1359646299000512⟩, ISSN 13596462

Bouaziz, Olivier/Le Corre, C.: Flow Stress and Microstructure Modelling of Ferrite-Pearlite Steels during Cold Rolling. Materials Science Forum, 426-432 2003, 1399–1404, ISSN 02555476

Brewer, L N et al.: Misorientation mapping for visualization of plastic deformation via electron back-scattered diffraction. Microscopy and Microanalysis, 12 2006, 85–91

Brewer, Luke N/Field, David P/Merriman, Colin C: Mapping and assessing plastic deformation using EBSD. In **Schwartz, Adam J. et al., editors:** Electron Backscatter Diffraction in Materials Science. 2nd edition. New York: Springer, 2009 ⟨URL: http://www.amazon.com/Electron-Backscatter-Diffraction-Materials-Science/dp/0387881352⟩, ISBN 0387881352. – chapter 18, 251–262

Cai, W./Bellon, P.: Microstructural self-organization triggered by twin boundaries during dry sliding wear. Acta Materialia, 60 nov 2012, Nr. 19, 6673–6684 ⟨URL: http://linkinghub.elsevier.com/retrieve/pii/S1359645412005769⟩, ISSN 13596454

Calcagnotto, Marion et al.: Orientation gradients and geometrically necessary dislocations in ultrafine grained dual-phase steels studied by 2D and 3D EBSD. Materials Science and Engineering: A, 527 apr 2010, Nr. 10-11, 2738–2746 ⟨URL: http://linkinghub.elsevier.com/retrieve/pii/S0921509310000195⟩, ISSN 09215093

Carroll, R. I./Beynon, J. H.: Decarburisation and rolling contact fatigue of a rail steel. Wear, 260 2006, Nr. 4-5, 523–537, ISSN 00431648

Cayron, C./Artaud, B./Briottet, L.: Reconstruction of parent grains from EBSD data. Materials Characterization, 57 dec 2006, Nr. 4-5, 386–401 ⟨URL: http://linkinghub.elsevier.com/retrieve/pii/S1044580306000830⟩, ISSN 10445803

Chandrasekaran, Dilip/Nygårds, Mikael: A study of the surface deformation behaviour at grain boundaries in an ultra-low-carbon steel. Acta Materialia, 51 oct 2003, Nr. 18, 5375–5384 ⟨URL: http://linkinghub.elsevier.com/retrieve/pii/S135964540300394X⟩, ISSN 13596454

Chaudhri, M M: Subsurface strain distribution around vickers hardness indentations in annealed polycrystalline copper. Acta Materialia, 46 1998, Nr. 9, 3047–3056

Chen, C.-L./Thomson, R.C.: The combined use of EBSD and EDX analyses for the identification of complex intermetallic phases in multicomponent Al-Si piston alloys.

Journal of Alloys and Compounds, 490 feb 2010, Nr. 1-2, 293–300 ⟨URL: http://linkinghub.elsevier.com/retrieve/pii/S0925838809019495⟩, ISSN 09258388

Christ, H.-J.: Cyclic stress-strain response and microstructure. ASM 19 1997

Cyril, Nisha/Fatemi, Ali/Cryderman, Bob: Effects of Sulfur Level and Anisotropy of Sulfide Inclusions on Tensile , Impact , and Fatigue Properties of SAE 4140 Steel. SAE International Journal of Materials and Manufacturing, 1 2009, Nr. 1, 218–227

Czichos, Horst/Habig, Karl-Heinz: Tribologie-Handbuch. 2nd edition. Friedr. Vieweg and Sohn Verlag, oct 2003

Dang Van, K/Maitournam, MH H H/Van, KD D: Steady-state flow in classical elastoplasticity: applications to repeated rolling and sliding contact. Journal of the Mechanics and Physics of Solids, 41 1993, Nr. 11, 1691–1710 ⟨URL: http://www.sciencedirect.com/science/article/pii/002250969390027D⟩

Danoix, F et al.: Direct evidence of cementite dissolution in drawn pearlitic steels observed by tomographic atom probe. Materials Science and Engineering: A, 250 1998, Nr. 1, 8–13, ISSN 09215093

Demir, Eralp et al.: Investigation of the indentation size effect through the measurement of the geometrically necessary dislocations beneath small indents of different depths using EBSD tomography. Acta Materialia, 57 jan 2009, Nr. 2, 559–569 ⟨URL: http://linkinghub.elsevier.com/retrieve/pii/S1359645408007003⟩, ISSN 13596454

Deutsche Edelstahlwerke GmbH: Cr-Mo-legierter Vergütungsstahl - 1.7225/ 1.7227, 42CrMo4/42CrMoS4. 2011

Dingley, D: Progressive steps in the development of electron backscatter diffraction and orientation imaging microscopy. Journal of microscopy, 213 2004, Nr. September 2003, 214–224 ⟨URL: http://onlinelibrary.wiley.com/doi/10.1111/j.0022-2720.2004.01321.x/full⟩

Dingley, D.J.: On-line determination of crystal orientation and texture determination in an SEM. Proceedings - Royal Microscopical Society, 19 1984, 74–75

Dingley, D.J.: On-line analysis of electron backscatter diffraction patterns, texture analysis of polysilicon. Scanning Electron Microscopy, 1 1987, 451–456

Dingley, DJ J J/Randle, V: Microtexture determination by electron back-scatter diffraction. Journal of Materials Science, 27 1992, Nr. 17, 4545–4566 ⟨URL: http://link.springer.com/article/10.1007/BF01165988⟩

Donzella, G. et al.: The competitive role of wear and RCF in a rail steel. Engineering Fracture Mechanics, 72 jan 2005, Nr. 2, 287–308 ⟨URL: http://linkinghub.elsevier.com/retrieve/pii/S0013794404001304⟩, ISSN 00137944

Dufrane, K.F./Glaeser, W.A.: Rolling-contact deformation of MgO single crystals. Wear, 37 apr 1976, Nr. 1, 21–32 ⟨URL: http://dx.doi.org/10.1016/0043-1648(76)90176-9⟩, ISSN 00431648

Durst, Karsten et al.: Indentation size effect in metallic materials: Modeling strength from pop-in to macroscopic hardness using geometrically necessary dislocations. Acta Materialia, 54 may 2006, Nr. 9, 2547–2555 ⟨URL: http://linkinghub.elsevier.com/retrieve/pii/S1359645406001194⟩, ISSN 13596454

Dwyer-Joyce, RS: The life cycle of a debris particle. In Tribology and Interface Engineering Series. Volume 48, Elsevier, 2005, 681–690

Eden, H. C./Garnham, J. E./Davis, C. L.: Influential microstructural changes on rolling contact fatigue crack initiation in pearlitic rail steels. Materials Science and Technology, 21 jun 2005, Nr. 6, 623–629 ⟨URL: http://www.maneyonline.com/doi/abs/10.1179/174328405X43207⟩, ISSN 0267–0836

El-Dasher, B.S/Adams, B.L/Rollett: Viewpoint: experimental recovery of geometrically necessary dislocation density in polycrystals. Scripta Materialia, 48 jan 2003, Nr. 2, 141–145 ⟨URL: http://linkinghub.elsevier.com/retrieve/pii/S1359646202003408⟩, ISSN 13596462

Farhat, Zoheir N.: Contribution of crystallographic texturing to the sliding friction behaviour of fcc and hcp metals. Wear, 250 oct 2001, Nr. 1-12, 401–408 ⟨URL: http://linkinghub.elsevier.com/retrieve/pii/S0043164801006044⟩, ISSN 00431648

Fleming, J.R./Suh, N.P.: Mechanics of crack propagation in delamination wear. Wear, 44 aug 1977, Nr. 1, 39–56 ⟨URL: http://dx.doi.org/10.1016/0043-1648(77)90083-7⟩, ISSN 00431648

Gachot, C et al.: A critical assessment of surface texturing for friction and wear improvement. Wear, 372 2017, 21–41

Ganapathi, S. K. et al.: A Comparative Study of the Nanocrystalline Material Produced by Sliding Wear and Inert Gas Condensation. MRS Proceedings, 206 feb 1990, 593–598 ⟨URL: http://journals.cambridge.org/abstract_S1946427400580269⟩, ISSN 1946–4274

Ganapathi, S.K. K/Rigney, D.A. A: An HREM study of the nanocrystalline material produced by sliding wear processes. Scripta Materialia, 24 sep 1990, Nr. 9, 1675–1678 ⟨URL: http://dx.doi.org/10.1016/0956-716X(90)90526-M⟩, ISSN 0956716X

Gao, Jianping et al.: Frictional Forces and Amontons' Law:â From the Molecular to the Macroscopic Scale. The Journal of Physical Chemistry B, 108 2004, Nr. 11, 3410–3425 ⟨URL: https://doi.org/10.1021/jp036362l⟩

Garnham, J. E./Davis, C. L.: Very early stage rolling contact fatigue crack growth in pearlitic rail steels. Wear, 271 2011, Nr. 1-2, 100–112 ⟨URL: http://dx.doi.org/10.1016/j.wear.2010.10.004⟩, ISSN 00431648

Gee, Mark/Mingard, Ken/Roebuck, Bryan: Application of EBSD to the evaluation of plastic deformation in the mechanical testing of WC/Co hardmetal. International Journal of Refractory Metals and Hard Materials, 27 mar 2009, Nr. 2, 300–312 ⟨URL: http://linkinghub.elsevier.com/retrieve/pii/S0263436808001017⟩, ISSN 02634368

Giannuzzi, L.a./Stevie, F.a.: A review of focused ion beam milling techniques for TEM specimen preparation. Micron, 30 jun 1999, Nr. 3, 197–204 ⟨URL: http://linkinghub.elsevier.com/retrieve/pii/S0968432899000050⟩, ISSN 09684328

Godet, Maurice: The third-body approach: A mechanical view of wear. Wear, 100 dec 1984, Nr. 1-3, 437–452 ⟨URL: http://dx.doi.org/10.1016/0043-1648(84)90025-5⟩, ISSN 00431648

Godet, Maurice: Third-bodies in tribology. Wear, 136 feb 1990, Nr. 1, 29–45 ⟨URL: http://dx.doi.org/10.1016/0043-1648(90)90070-Q⟩, ISSN 00431648

Gottstein, Günter: Physikalische Grundlagen der Materialkunde (Springer-Lehrbuch) (German Edition). Springer, 2007, 520, ISBN 354071104X

Grimmer, H.: A unique description of the relative orientation of neighbouring grains. Acta Crystallographica Section A, 36 may 1980, Nr. 3, 382–389 ⟨URL: http://scripts.iucr.org/cgi-bin/paper?S0567739480000861⟩, ISSN 0567–7394

Gross, T S/Lampman, S: Micromechanisms of monotonic and cyclic crack growth. ASM Handbook Fatigue and Fracture 19 1997

Grum, Janez: A review of the influence of grinding conditions on resulting residual stresses after induction surface hardening and grinding. Journal of Materials Processing Technology, 114 2001, 212–226

Hamrock, B. J./Dowson, D.: Isothermal elastohydrodynamic lubrication of point contacts. III - Fully flooded results. Journal of Tribology, 99 1977, Nr. 2, 264–275, ISSN 04021215

Hamrock, B. J./Dowson, D.: Ball bearing lubrication: the elastohydrodynamics of elliptical contacts. John Wiley and Sons, 1981

Harvey, S. et al.: Microscopy and microindentation mechanics of single crystal Fe-3 wt. % Si: Part I. Atomic force microscopy of a small indentation. Journal of Materials Research, 8 jan 1993, Nr. 06, 1291–1299, ISSN 0884–2914

Hauk, Viktor: Structural and residual stress analysis by nondestructive methods: Evaluation-Application-Assessment. Elsevier, 1997

Heilmann, P. et al.: Orientationdetermination of subsurface cells generated by sliding. Acta Metallurgica, 31 aug 1983, Nr. 8, 1293–1305 ⟨URL: http://dx.doi.org/10.1016/0001-6160(83)90191-8⟩, ISSN 00016160

Heilmann, P et al.: Computerized method to determine crystal orientations from kikuchi patterns. Ultramicroscopy, 9 1982, 365–372 ⟨URL: http://www.sciencedirect.com/science/article/pii/0304399182900973⟩

Heilmann, P. et al.: Sliding wear and transfer. Wear, 91 nov 1983, Nr. 2, 171–190 ⟨URL: http://dx.doi.org/10.1016/0043-1648(83)90252-1⟩, ISSN 00431648

Heimendahl, Manfred von/Heimendahl, Manfred von: Electron microscopy of materials: An introduction. Academic Press (New York, N.Y.), 1980 ⟨URL: http://books.google.de/books?id=sD1RAAAAMAAJ&q=Electron+microscopy+of+materials:+an+introduction&dq=Electron+microscopy+of+materials:+an+introduction&hl=de&sa=X&ei=wbFuUdD-JpGL4gSikoCwCA&redir_esc=y⟩

Hertz, H: Über die Berührung fester elastischer Körper. Journal für die reine und angewandte Mathematik, 92 1881, 156–171

Hintermann, H.E.: Adhesion, friction and wear of thin hard coatings. Wear, 100 dec 1984, Nr. 1-3, 381–397 ⟨URL: http://dx.doi.org/10.1016/0043-1648(84)90023-1⟩, ISSN 00431648

Hirth, J.P./Rigney, D.A.: Crystal plasticity and the delamination theory of wear. Wear, 39 aug 1976, Nr. 1, 133–141 ⟨URL: http://www.sciencedirect.com/science/article/pii/0043164876902295⟩, ISSN 00431648

Hoeppner, D: Industrial significance of fatigue problems. ASM Handbook Fatigue and Fracture 19 1997

Hokkirigawa, K./Kato, K.: An experimental and theoretical investigation of ploughing, cutting and wedge formation during abrasive wear. Tribology International, 21 feb 1988, Nr. 1, 51–57 ⟨URL: http://linkinghub.elsevier.com/retrieve/pii/0301679X88901284⟩, ISSN 0301679X

Holm, R: Electric Contacts. Almqvist & Wiksells Akademiska Handböcker, 1946 ⟨URL: http://books.google.de/books?id=GvdOAAAAMAAJ&dq=electriccontactsholm&hl=de&source=gbs_book_other_versions⟩, 398

Holzapfel, C et al.: Interaction of cracks with precipitates and grain boundaries: Understanding crack growth mechanisms through focused ion beam tomography. Scripta Materialia, 56 2007, 697–700

Hornbogen, Erhard: Werkstoffe: Aufbau und Eigenschaften von Keramik- Metall- Polymer- und Verbundwerkstoffen. 10th edition. Springer, 2012, 63

Hsu, K.-L./Ahn, T.M./Rigney, D.A.: Friction, wear and microstructure of unlubricated austenitic stainless steels. Wear, 60 apr 1980, Nr. 1, 13–37 ⟨URL: http://dx.doi.org/10.1016/0043-1648(80)90247-1⟩, ISSN 00431648

Humphreys, F J: Quantitative metallography by electron backscattered diffraction. Journal of microscopy, 195 sep 1999, Nr. 3, 170–185 ⟨URL: http://www.ncbi.nlm.nih.gov/pubmed/10460682http://doi.wiley.com/10.1046/j.1365-2818.1999.00578.x⟩, ISSN 1365–2818

Humphreys, F J: Review - Grain and subgrain characterisation by electron backscatter diffraction. Journal of Materials Science, 36 2001, 3833–3854

Humphreys, F J/Bate, P S/Hurley, P J: Orientation averaging of electron backscattered diffraction data. Journal of microscopy, 201 jan 2001, Nr. Pt 1, 50–8 ⟨URL: http://www.ncbi.nlm.nih.gov/pubmed/11136439⟩, ISSN 0022–2720

Humphreys, F J/Brough, I: High resolution electron backscatter diffraction with a field emission gun scanning electron microscope. Journal of Microscopy, 195 1999, Nr. 1, 6–9

Humphreys, F.J: Characterisation of fine-scale microstructures by electron backscatter diffraction (EBSD). Scripta Materialia, 51 oct 2004, Nr. 8, 771–776 ⟨URL: http://linkinghub.elsevier.com/retrieve/pii/S1359646204002854⟩, ISSN 13596462

Humphreys, F.J./Bate, P.S.: Measuring the alignment of low-angle boundaries formed during deformation. Acta Materialia, 54 feb 2006, Nr. 3, 817–829 ⟨URL: http://linkinghub.elsevier.com/retrieve/pii/S1359645405006075⟩, ISSN 13596454

Humphreys, F.J./Bate, P.S.: The microstructures of polycrystalline Al-0.1Mg after hot plane strain compression. Acta Materialia, 55 sep 2007, Nr. 16, 5630–5645 ⟨URL: http://linkinghub.elsevier.com/retrieve/pii/S1359645407004272⟩, ISSN 13596454

Humphreys, FJ et al.: Electron backscatter diffraction of grain and subgrain structures - resolution considerations. Journal of Micros, 195 sep 1999, Nr. 3, 212–216 ⟨URL: http://www.ncbi.nlm.nih.gov/pubmed/10460686⟩, ISSN 1365–2818

Hutchinson, WB et al.: On the description of misorientations and interpretation of recrystallization textures. Scripta materialia, 35 1996, Nr. 5, 579–582 ⟨URL: http://www.osti.gov/energycitations/product.biblio.jsp?osti_id=367257⟩

Iza-Mendia, A./Gutiérrez, I.: Generalization of the existing relations between microstructure and yield stress from ferrite-pearlite to high strength steels. Materials Science and Engineering A, 561 2013, 40–51, ISBN 09215093 (ISSN)

Jeong, Bong-Yong et al.: A study on the surface characteristics of dual phase steel by electron backscatter diffraction (EBSD) technique. Transactions on Electrical and Electronic Materials, 15 2014, Nr. 1, 20–23 ⟨URL: http://koreascience.or.kr/journal/view.jsp?kj=E1TEAO&py=2014&vnc=v15n1&sp=20⟩, ISSN 1229–7607

Johnson, K L: Contact mechanics. Volume Reprint, Cambridge University Press, 1987

Johnson, K L: Contact mechanics and the wear of metals. Wear, 190 1995, 162–170

Jost, H Peter: Lubrication: Tribology; Education and Research; Report on the Present Position and Industry's Needs (submitted to the Department of Education and Science by the Lubrication Engineering and Research) Working Group. HM Stationery Office, 1966

Kalin, Mitjan: Influence of flash temperatures on the tribological behaviour in low-speed sliding: a review. Materials Science and Engineering A, 374 2004, 390–397

Kalin, Mitjan/Velkavrh, Igor/Vizintin, Joze: The Stribeck curve and lubrication design for non-fully wetted surfaces. Wear, 267 2009, Nr. 5-8, 1232–1240

Kamaya, Masayuki: Characterization of microstructural damage due to low-cycle fatigue by EBSD observation. Materials Characterization, 60 dec 2009, Nr. 12, 1454–1462 ⟨URL: http://linkinghub.elsevier.com/retrieve/pii/S1044580309002502⟩, ISSN 10445803

Kamaya, Masayuki: Measurement of local plastic strain distribution of stainless steel by electron backscatter diffraction. Materials Characterization, 60 feb

2009, Nr. 2, 125–132 ⟨URL: http://linkinghub.elsevier.com/retrieve/pii/S104458030800212X⟩, ISSN 10445803

Kamaya, Masayuki: A Smoothing Filter for Misorientation Mapping Obtained by EBSD. Materials Transactions, 51 2010, Nr. 9, 1516–1520 ⟨URL: http://joi.jlc.jst.go.jp/JST.JSTAGE/matertrans/MAW201005?from=CrossRef⟩, ISSN 1347–5320

Kamaya, Masayuki: Assessment of local deformation using EBSD: quantification of accuracy of measurement and definition of local gradient. Ultramicroscopy, 111 jul 2011, Nr. 8, 1189–99 ⟨URL: http://www.ncbi.nlm.nih.gov/pubmed/21763236⟩, ISSN 1879–2723

Kamaya, Masayuki/Kuroda, Masatoshi: Fatigue Damage Evaluation Using Electron Backscatter Diffraction. Materials Transactions, 52 2011, Nr. 6, 1168–1176 ⟨URL: http://joi.jlc.jst.go.jp/JST.JSTAGE/matertrans/M2011014?from=CrossRef⟩, ISSN 1347–5320

Kamaya, Masayuki/Wilkinson, Angus J./Titchmarsh, John M.: Measurement of plastic strain of polycrystalline material by electron backscatter diffraction. Nuclear Engineering and Design, 235 mar 2005, Nr. 6, 713–725 ⟨URL: http://linkinghub.elsevier.com/retrieve/pii/S0029549304003796⟩, ISSN 00295493

Kamaya, Masayuki/Wilkinson, Angus J./Titchmarsh, John M.: Quantification of plastic strain of stainless steel and nickel alloy by electron backscatter diffraction. Acta Materialia, 54 jan 2006, Nr. 2, 539–548 ⟨URL: http://linkinghub.elsevier.com/retrieve/pii/S1359645405005665⟩, ISSN 13596454

Kapoor, A et al.: Computer simulation of strain accumulation and hardening for pearlitic rail steel undergoing repeated contact. The Journal of Strain Analysis for Engineering Design, 39 2005, Nr. 4, 383–396, ISBN 0309324041

Kapoor, a. et al.: Surface roughness and plastic flow in rail wheel contact. Wear, 253 2002, Nr. 1-2, 257–264, ISBN 00431648 (ISSN)

Klimek, Leszek/Pietrzyk, Bożena: Electron backscatter diffraction as a useful method for alloys microstructure characterization. Journal of Alloys and Compounds, 382 November 2004, Nr. 1-2, 17–23 ⟨URL: http://linkinghub.elsevier.com/retrieve/pii/S0925838804007613⟩, ISSN 09258388

Konijnenberg, P.J./Zaefferer, S./Raabe, D.: Assessment of geometrically necessary dislocation levels derived by 3D EBSD. Acta Materialia, 99 2015, 402–414 ⟨URL: http://www.sciencedirect.com/science/article/pii/S1359645415004474⟩, ISSN 13596454

Konrad, J./Zaefferer, S./Raabe, D.: Investigation of orientation gradients around a hard Laves particle in a warm-rolled Fe3Al-based alloy using a 3D EBSD-FIB technique. Acta Materialia, 54 mar 2006, Nr. 5, 1369–1380 ⟨URL: http://linkinghub.elsevier.com/retrieve/pii/S1359645405006828⟩, ISSN 13596454

Korres, Spyridon/Feser, Tim/Dienwiebel, Martin: In situ observation of wear particle formation on lubricated sliding surfaces. Acta Materialia, 60 jan 2012, Nr. 1, 420–429 ⟨URL: http://linkinghub.elsevier.com/retrieve/pii/S1359645411006938⟩, ISSN 13596454

Krieger Lassen, N C: Automatic high-precision measurements of the location and width of Kikuchi bands in electron backscatter diffraction patterns. Journal of Microscopy, 190 1998, Nr. June, 375–391

Kubin, L.P/Mortensen, a: Geometrically necessary dislocations and strain-gradient plasticity: a few critical issues. Scripta Materialia, 48 jan 2003, Nr. 2, 119–125 ⟨URL: http://linkinghub.elsevier.com/retrieve/pii/S1359646202003354⟩, ISSN 13596462

Kuhlmann-Wilsdorf, D.: Flash temperatures due to friction and Joule heat at asperity contacts. Wear, 105 oct 1985, Nr. 3, 187–198 ⟨URL: http://dx.doi.org/10.1016/0043-1648(85)90067-5⟩, ISSN 00431648

Kuhlmann-Wilsdorf, Doris: Demystifying flash temperatures I. Analytical expressions based on a simple model. Materials Science and Engineering, 93 sep 1987, Nr. null, 107–118 ⟨URL: http://dx.doi.org/10.1016/0025-5416(87)90417-4⟩, ISSN 00255416

Kumar, Anish/Pollock, Tresa M.: Mapping of femtosecond laser-induced collateral damage by electron backscatter diffraction. Journal of Applied Physics, 110 2011, Nr. 8, 083114 ⟨URL: http://link.aip.org/link/JAPIAU/v110/i8/p083114/s1&Agg=doi⟩, ISSN 00218979

Kumar, Sharvan/Curtin, William A: Crack interaction with microstructures. materialstoday, 10 2007, Nr. 9, 34–44

Kuo, HK/Cohen, JB: Changes in residual stress, domain size and microstrain during the fatigue of AISI 1008 steel. Materials Science and Engineering, 61 1983, 127–136 ⟨URL: http://www.sciencedirect.com/science/article/pii/0025541683901957⟩

Lai, W T/Cheng, H S/Cheng H S: Temperature Analysis in Lubricated Simple Sliding Rough Contacts. ASLE Transactions, 28 1985, Nr. 3, 303–312, ISBN 0569819850898

Languillaume, J./Kapelski, G./Baudelet, B.: Cementite dissolution in heavily cold drawn pearlitic steel wires. Acta Materialia, 45 1997, Nr. 3, 1201–1212, ISSN 13596454

Lansdown, A R/L, Price A: Materials to resist wear: a guide to their selection and use. Pergamon, Oxford, 1986

Lee, H H/Uhlig, H H: Corrosion Fatigue of Type 4140 High Strength Steel. Metallurgical Transactions, 3 1972, Nr. November, 2949–2957

Lee, Ki Myung/Polycarpou, Andreas a.: Wear of conventional pearlitic and improved bainitic rail steels. Wear, 259 July 2005, Nr. 1-6, 391–399 ⟨URL: `http://linkinghub.elsevier.com/retrieve/pii/S0043164805001651`⟩, ISSN 00431648

Lee, S.-B./Rollett, A D/Rohrer, G S: Three-Dimensional Microstructure Reconstruction Using FIB-OIM. Materials Science Forum, 558-559 2007, 915–920

Lee, W. B. et al.: The effect of the cementite phase on the surface hardening of carbon steels by shot peening. Materials Science and Engineering A, 527 2010, Nr. 21-22, 5852–5857 ⟨URL: `http://dx.doi.org/10.1016/j.msea.2010.05.083`⟩, ISBN 0921–5093

Lehockey, EM/Lin, Y/Lepik, OE: Mapping residual plastic strain in materials using electron backscatter diffraction. In **Schwartz, AJ/Kumar, M/Adams, BL, editors:** Electron backscatter diffraction in materials science. New York: Kluwer Academic, 2000. – chapter 20, 247–265

Liedtke, Dieter: Merkblatt 450: Wärmebehandlung von Stahl - Härten, Anlassen, Vergüten, Bainitisieren. 2005

Linz, M et al.: EBSD study of early-damaging phenomena in wheel-rail model test. Wear, 342-343 2015, 13–21 ⟨URL: `http://dx.doi.org/10.1016/j.wear.2015.08.004http://linkinghub.elsevier.com/retrieve/pii/S0043164815003750`⟩, ISSN 00431648

Linz, M et al.: Plastic Strain Evlolution and Distribution in ferritic / pearlitic Microstructures by tribological sliding. In Materials Science and Engineering. Darmstadt, 2014, 40

Linz, M et al.: On the competition between plastic deformation and material detachment in ferritic/pearlitic steel under boundary lubrication. Wear, 376 2017, 813–821

Linz, Mathias et al.: Heterogeneous Strain Distribution and Saturation of Geometrically Necessary Dislocations in a Ferritic–Pearlitic Steel during Lubricated Sliding. Advanced Engineering Materials 2018

Linz, Mathias et al.: Surface crack propagation and morphology in cutting tools. Industrial Lubrication and Tribology, 68 2016, Nr. 1, 141–148

Linz, Mathias Peter: Contact Fatigue Testing of Camring Steel. Ph. D thesis, Luleå Tekniska Universitet, 2010,, 48

Liu, Shuangbiao/Wang, Qian: Studying Contact Stress Fields Caused by Surface Tractions With a Discrete Convolution and Fast Fourier Transform Algorithm. Journal of Tribology, 124 2002, Nr. 1, 36 ⟨URL: `http://tribology.asmedigitalcollection.asme.org/article.aspx?articleid=1466572`⟩, ISSN 07424787

Lozano-Perez, Sergio: A guide on FIB preparation of samples containing stress corrosion crack tips for TEM and atom-probe analysis. Micron, 39 2008, 320–328

Lundberg, G/Palmgren, A: Dynamic capacity of roller bearings. Acta polytechnica Scandinavica. Mechanical engineering series. 1 1947, Nr. 3

Macherauch, Eckard/Zoch, Hans-Werner: Praktikum in Werkstoffkunde. Volume 11, Vieweg +Teubner Verlag Wiesbaden, 2011

Mackenzie, JK: Second paper on statistics associated with the random disorientation of cubes. Biometrika, 1958, 229–240 ⟨URL: `http://biomet.oxfordjournals.org/content/45/1-2/229.short`⟩

Maharaj, Dave/Bhushan, Bharat: Nanomanipulation , nanotribology and nanomechanics of Au nanorods in dry and liquid environments using an AFM and depth sensing nanoindenter. Nanoscale, 6 2014, 5838–5852

Mahato, Anirban et al.: Severe wear of a near eutectic aluminium-silicon alloy. Acta Materialia, 59 sep 2011, Nr. 15, 6069–6082 ⟨URL: `http://linkinghub.elsevier.com/retrieve/pii/S1359645411004307`⟩, ISBN 8023600648

Man, J et al.: Application of FIB technique to study of early fatigue damage in polycrystals. Journal of Physics: Conference Series, 240 jul 2010, 1–4 ⟨URL: `http://stacks.iop.org/1742-6596/240/i=1/a=012058?key=crossref.030d03705ea80635e2d87f9bfe29f765`⟩, ISSN 1742–6596

Merkel, Manfred/Thomas, Karl-Heinz: Taschenbuch der Werkstoffe. Volume 7, Carl Hanser Verlag München, 2008

Meshi, Louisa et al.: Dislocation structure and hardness of surface layers under friction of copper in different lubricant conditions. Acta Materialia, 59 jan 2011, Nr. 1, 342–348 ⟨URL: `http://linkinghub.elsevier.com/retrieve/pii/S1359645410006154`⟩, ISSN 13596454

Meyer, MD/Kestens, L/Cooman, BC: Texture development in cold rolled and annealed C - Mn - Si and C - Mn - Al - Si TRIP steels. Materials Science and Technology, 17 2001, Nr. November, 1353–1359

Mingard, K.P./Gee, M.G.: EBSD examination of worn WC/Co hardmetal surfaces. Wear, 263 sep 2007, Nr. 1-6, 643–652 ⟨URL: `http://linkinghub.elsevier.com/retrieve/pii/S0043164807003973`⟩, ISSN 00431648

Mingard, K.P. et al.: Comparison of EBSD and conventional methods of grain size measurement of hardmetals. International Journal of Refractory Metals and Hard Materials, 27 mar 2009, Nr. 2, 213–223 ⟨URL: `http://linkinghub.elsevier.com/retrieve/pii/S0263436808000760`⟩, ISSN 02634368

Miyoshi, Kazuhisa/Buckley, Donald H: Friction and Wear Behavior of Single-Crystal Silicon Carbide in Sliding Contact with Various Metals. A S L E Transactions, 22 1979, Nr. 3, 245–256

Morawiec, a.: Misorientation-Angle Distribution of Randomly Oriented Symmetric Objects. Journal of Applied Crystallography, 28 jun 1995, Nr. 3, 289–293 ⟨URL: `http://scripts.iucr.org/cgi-bin/paper?S0021889894011088`⟩, ISSN 0021–8898

Mori, Shigeyuki/Wilfredo, Morales: Tribological reactions of perfluoroalkyl polyether oils with stainless steel under ultrahigh vacuum conditions at room temperature. Wear, 132 1989, Nr. 1, 111–121

Morris, E/Chung, F/Chung, Y-W: Fatigue failure in metals. AS 19 1997

Moshkovich, A. et al.: The Effect of Grain Size on Stribeck Curve and Microstructure of Copper Under Friction in the Steady Friction State. Tribology Letters, 42 2011, Nr. 1, 89–98 ⟨URL: `http://link.springer.com/10.1007/s11249-011-9752-3`⟩, ISSN 1023–8883

Moshkovich, Alexey/Lapsker, Igor/Rapoport, Lev: Correlation between strengthening and damage of Cu refined by different SPD processing and friction in different lubricant regions. Wear, 305 2013, Nr. 1-2, 45–50 ⟨URL: `http://dx.doi.org/10.1016/j.wear.2013.05.013`⟩, ISBN 00431648 (ISSN)

Moshkovich, Alexey et al.: Structural evolution in copper layers during sliding under different lubricant conditions. Acta Materialia, 58 aug 2010, Nr. 14, 4685–4692 ⟨URL: `http://linkinghub.elsevier.com/retrieve/pii/S1359645410002752`⟩, ISSN 13596454

Movahed, P. et al.: The effect of intercritical heat treatment temperature on the tensile properties and work hardening behavior of ferrite-martensite dual phase steel sheets. Materials Science and Engineering A, 518 2009, Nr. 1-2, 1–6, ISBN 09215093 (ISSN)

Munroe, P.R. R: The application of focused ion beam microscopy in the material sciences. Materials Characterization, 60 jan 2009, Nr. 1, 2–13 ⟨URL: `http://linkinghub.elsevier.com/retrieve/pii/S1044580308003306`⟩, ISSN 10445803

Narasaiah, N./Ray, K. K.: Small crack formation in a low carbon steel with banded ferrite-pearlite structure. Materials Science and Engineering A, 392 2005, Nr. 1-2, 269–277, ISSN 09215093

Nino, Akihiro et al.: Indentation Size Effect for the Hardness of Refractory Carbides. Materials Transactions, 51 2010, Nr. 9, 1621–1626 ⟨URL: `http://joi.jlc.jst.go.jp/JST.JSTAGE/matertrans/M2010110?from=CrossRef`⟩, ISSN 1347–5320

Nye, J.F: Some geometrical relations in dislocated crystals. Acta Metallurgica, 1 mar 1953, Nr. 2, 153–162 ⟨URL: `http://dx.doi.org/10.1016/0001-6160(53)90054-6`⟩, ISSN 00016160

Nygårds, Mikael/Gudmundson, Peter: Micromechanical modeling of ferritic/pearlitic steels. Materials Science and Engineering A, 325 2002, 435–443

Ohr, SM M M: An electron microscope study of crack tip deformation and its impact on the dislocation theory of fracture. Materials Science and Engineering, 72 1985, 1–35 ⟨URL: `http://www.sciencedirect.com/science/article/pii/0025541685900643`⟩

Palaci, Ismaël: Atomic force microscopy studies of nanotribology and nanomechanics. Ph. D thesis, École Polytechnique Fédérale de Lausanne, 2007

Pan, Ning/Sheppard, Sheri D: Stress intensity factors in spot welds. Engineering Fracture Mechanics, 70 2003, 671–684

Pantleon, W.: Resolving the geometrically necessary dislocation content by conventional electron backscattering diffraction. Scripta Materialia, 58 jun 2008, Nr. 11, 994–997 ⟨URL: `http://linkinghub.elsevier.com/retrieve/pii/S1359646208000912`⟩, ISSN 13596462

Peng, X./Fan, J./Zeng, J.: Microstructure-based description for the mechanical behavior of single pearlitic colony. International Journal of Solids and Structures, 39 2001, Nr. 2, 435–448 ⟨URL: `http://www.sciencedirect.com/science/article/pii/S0020768301002220`⟩, ISSN 00207683

Peranio, N. et al.: Microstructure and texture evolution in dual-phase steels: Competition between recovery, recrystallization, and phase transformation. Materials Science and Engineering: A, 527 jun 2010, Nr. 16-17, 4161–4168 ⟨URL: http://linkinghub.elsevier.com/retrieve/pii/S0921509310003023⟩, ISSN 09215093

Perret, J. et al.: EBSD, SEM and FIB characterisation of subsurface deformation during tribocorrosion of stainless steel in sulphuric acid. Wear, 269 jul 2010, Nr. 5-6, 383–393 ⟨URL: http://linkinghub.elsevier.com/retrieve/pii/S0043164810001821⟩, ISSN 00431648

Petch, N J: The cleavage strength of polycrystals. Journal of the Iron and Steel Institute, 174 1953, 25–26

Petrov, Roumen et al.: Microstructure and texture of a lightly deformed TRIP-assisted steel characterized by means of the EBSD technique. Materials Science and Engineering: A, 447 feb 2007, Nr. 1-2, 285–297 ⟨URL: http://linkinghub.elsevier.com/retrieve/pii/S0921509306021277⟩, ISSN 09215093

Phaneuf, M.W: Applications of focused ion beam microscopy to materials science specimens. Micron, 30 jun 1999, Nr. 3, 277–288 ⟨URL: http://linkinghub.elsevier.com/retrieve/pii/S0968432899000128⟩, ISSN 09684328

Pippan, R et al.: Saturation of fragmentation during severe plastic deformation. Annual Review of Materials Research, 40 2010, Nr. 1, 319–343, ISBN 0709091044

Pippan, R. et al.: The limits of refinement by severe plastic deformation. Advanced Engineering Materials, 8 2006, Nr. 11, 1046–1056 ⟨URL: http://doi.wiley.com/10.1002/adem.200600133⟩, ISSN 14381656

Pombo, João et al.: A Railway wheel wear prediction Tool based on a multibody Software. Journal of theoretical and applied Mechanics, 48 2010, Nr. 3, 751–770

Pombo, João et al.: Development of a wear prediction tool for steel railway wheels using three alternative wear functions. Wear, 271 may 2011, Nr. 1-2, 238–245 ⟨URL: http://linkinghub.elsevier.com/retrieve/pii/S0043164811000731⟩, ISSN 00431648

Popov, Valentin L.: Kontaktmechanik und Reibung: Ein Lehr- und Anwendungsbuch von der Nanotribologie bis zur numerischen Simulation (German Edition). Springer, 2009 ⟨URL: http://www.amazon.com/Kontaktmechanik-Reibung-Anwendungsbuch-Nanotribologie-numerischen/dp/3540888365⟩, 328, ISBN 3540888365

Prasad, Somuri V. et al.: Modeling of Friction-Induced Deformation and Microstructures. Albuquerque (New Mexiko) and Livermore (California), 2006 , 9–92 pages

Prasad, S.V/Michael, J.R/Christenson, T.R: EBSD studies on wear-induced subsurface regions in LIGA nickel. Scripta Materialia, 48 feb 2003, Nr. 3, 255–260 ⟨URL: http://linkinghub.elsevier.com/retrieve/pii/S1359646202003767⟩, ISSN 13596462

Prior, DJ et al.: The application of electron backscatter diffraction and orientation contrast imaging in the SEM to textural problems in rocks. American Mineralogist, 84 1999, 1741–1759 ⟨URL: http://minsocam.org/MSA/AmMin/TOC/Articles_Free/1999/Prior_p1741-1759_99.pdf⟩

Raabe, D et al.: Theory of orientation gradients in plastically strained crystals. Acta Materialia, 50 jan 2002, Nr. 2, 421–440 ⟨URL: http://linkinghub.elsevier.com/retrieve/pii/S1359645401003238⟩, ISBN 4921167923

Rainforth, W. M.: Microstructural evolution at the worn surface: A comparison of metals and ceramics. Wear, 245 2000, Nr. 1-2, 162–177, ISBN 0043–1648

Randle, Valerie: Recent Developments in Electron Backscatter Diffraction. Advances in Imaging and Electron Physics, 151 2008, 363–416 ⟨URL: http://dx.doi.org/10.1016/S1076-5670(07)00405-3⟩

Randle, Valerie: Electron backscatter diffraction: Strategies for reliable data acquisition and processing. Materials Characterization, 60 sep 2009, Nr. 9, 913–922 ⟨URL: http://linkinghub.elsevier.com/retrieve/pii/S1044580309001879⟩, ISSN 10445803

Rao, DV Sridhara/Muraleedharan, K/Humphreys, CJ: TEM specimen preparation techniques. Microscopy: science, technology, applications and education, 2010, 1232–1244

Reza Bateni, M. et al.: The Effect of Grain Orientation on Micro Frictional of Medium Carbon Steel. Materials Science Forum, 495-497 2005, 203–206 ⟨URL: http://www.scientific.net/MSF.495-497.203⟩, ISSN 1662–9752

Rice, Stephen L/Wayne, Steven F/Nowotny, Hans: Specimen material reversal in pin-on-disc tribotesting. Wear, 88 1983, 85–92

Rigney, D A: Sliding wear of metals. Annual Review of Materials Science, 18 aug 1988, Nr. 1, 141–163 ⟨URL: http://www.annualreviews.org/doi/abs/10.1146/annurev.ms.18.080188.001041⟩, ISSN 0084–6600

Rigney, D A: Comments on the sliding wear of metals. Tribology International, 30 may 1997, Nr. 5, 361–367 ⟨URL: http://dx.doi.org/10.1016/S0301-679X(96)00065-5⟩, ISSN 0301679X

Rigney, D A: Large strains associated with sliding contact of metals. Material Research Innovations, 1 1998, 231–234

Rigney, D A/Divakar, R/Kuo, S M: Deformation substructures associated with very large plastic strains. Scripta Materialia, 27 1992, 975–980

Rigney, D.A.: Fundamentals of friction and wear of materials: papers presented at the 1980 ASM Materials Science Seminar. Pittsburgh, Pennsylvania: American Society for Metals, 1981

Rigney, D.A.: The roles of hardness in the sliding behavior of materials. Wear, 175 jun 1994, Nr. 1-2, 63–69 ⟨URL: http://dx.doi.org/10.1016/0043-1648(94)90169-4⟩, ISSN 00431648

Rigney, D.a: Transfer, mixing and associated chemical and mechanical processes during the sliding of ductile materials. Wear, 245 oct 2000, Nr. 1-2, 1–9 ⟨URL: http://linkinghub.elsevier.com/retrieve/pii/S0043164800004609⟩, ISSN 00431648

Rigney, D.A. et al.: Wear processes in sliding systems. Wear, 100 dec 1984, Nr. 1-3, 195–219 ⟨URL: http://dx.doi.org/10.1016/0043-1648(84)90013-9⟩, ISSN 00431648

Rigney, D.A. et al.: Examples of structural evolution during sliding and shear of ductile materials. Scripta Materialia, 49 nov 2003, Nr. 10, 977–983 ⟨URL: http://linkinghub.elsevier.com/retrieve/pii/S135964620300472X⟩, ISSN 13596462

Rigney, D.A. A et al.: Low energy dislocation structures caused by sliding and by particle impact. Materials Science and Engineering, 81 1986, 409–425 ⟨URL: http://www.sciencedirect.com/science/article/pii/002554168690279X⟩

Ringsberg, J: Rolling contact fatigue of railway rails with emphasis on crack initiation. Ph. D thesis, Chalmers University of Technology, Institut för Hållfasthetslära, Göteborg, Sweden, 2000

Ringsberg, JW/Loo-Morrey, M: Prediction of fatigue crack initiation for rolling contact fatigue. International Journal of Fatigue, 22 2000, 205–215 ⟨URL: http://www.sciencedirect.com/science/article/pii/S0142112399001255⟩

Roberts, G et al.: Use of misorientation values to further understand deformation in rail steels. Ironmaking and Steelmaking, 40 feb 2013, Nr. 2, 92–97 ⟨URL: http://openurl.ingenta.com/content/xref?genre=article&issn=0301-9233&volume=40&issue=2&spage=92⟩, ISSN 03019233

Robles Hernández, Francisco C. et al.: Mechanical properties and wear performance of premium rail steels. Wear, 263 sep 2007, Nr. 1-6, 766–772 ⟨URL: http://linkinghub.elsevier.com/retrieve/pii/S0043164807002980⟩, ISSN 00431648

Roesler, Joachim/Harders, Harald/Martin, Baeker: Mechanical Behaviour of Engineering Materials. Springer, 2007

Roos, Eberhard/Maile, Karl: Werkstoffkunde für Ingenieure. Volume 4, Springer Heidelberg, 2011

Rupert, Timothy J./Schuh, Christopher a.: Sliding wear of nanocrystalline Ni-W: Structural evolution and the apparent breakdown of Archard scaling. Acta Materialia, 58 jul 2010, Nr. 12, 4137–4148 ⟨URL: http://linkinghub.elsevier.com/retrieve/pii/S1359645410002119⟩, ISSN 13596454

Saarstahl: Werkstoff-Datenblatt Saarstahl - 42CrMo4 - 42CrMoS4.

Sawada, Hidetaka et al.: Resolving 45-pm-separated Si–Si atomic columns with an aberration-corrected STEM. Microscopy, 64 2015, Nr. 3, 213–217

Scheriau, S./Pippan, R.: Severe Plastic Deformation of Steels. BHM Berg- und Hüttenmännische Monatshefte, 153 2008, Nr. 7, 242–246 ⟨URL: http://link.springer.com/10.1007/s00501-008-0388-z⟩, ISSN 0005–8912

Schijve, J: Fatigue of Structures and Materials. Kluwer Academic Publishers, 2004

Senthilkumar, D et al.: Influence of shallow and deep cryogenic treatment on the residual state of stress of 4140 steel. Journal of Materials Processing Technology, 211 mar 2011, Nr. 3, 396–401 ⟨URL: http://linkinghub.elsevier.com/retrieve/pii/S0924013610003274⟩, ISSN 09240136

Sexton, M.D./Fischer, T.E.: The mild wear of 52100 steel. Wear, 96 jun 1984, Nr. 1, 17–30 ⟨URL: http://dx.doi.org/10.1016/0043-1648(84)90101-7⟩, ISSN 00431648

Shigesato, G./Rauch, E.F.: Dislocation structure misorientations measured with an automated electron diffraction pattern indexing tool. Materials Science and Engineering: A, 462 jul 2007, Nr. 1-2, 402–406 ⟨URL: http://linkinghub.elsevier.com/retrieve/pii/S0921509306018508⟩, ISSN 09215093

Singer, I. L.: Mechanics and Chemistry of Solids in Sliding Contact. Langmuir, 12 jan 1996, Nr. 19, 4486–4491 ⟨URL: http://pubs.acs.org/doi/abs/10.1021/la951056n⟩, ISSN 0743–7463

Spieß, Lothar et al.: Moderne Röntgenbeugung. Volume 2, Vieweg + Teubner — GWV Fachverlage GmbH, Wiesbaden, 2009

Stachowiak, Gwidon/Batchelor, Andrew W.: Engineering tribology. Butterworth-Heinemann, 2013, 312

Stock, R./Pippan, R.: RCF and wear in theory and practice-The influence of rail grade on wear and RCF. Wear, 271 may 2011, Nr. 1-2, 125–133 ⟨URL: http://linkinghub.elsevier.com/retrieve/pii/S0043164810003492⟩, ISSN 00431648

Struers: Präparation von Eisenwerkstoffen für die EBSD-Analyse. Copenhagen, Denmark, 2009

Suh, Nam P.: An overview of the delamination theory of wear. Wear, 44 1977, Nr. 1, 1–16

Suresh, Subra: Fatigue of materials. 2nd edition. Cambridge University Press, 1998

Swalla, Dana R./Neu, Richard W.: Fretting damage assessment of titanium alloys using orientation imaging microscopy. Tribology International, 39 oct 2006, Nr. 10, 1016–1027 ⟨URL: http://linkinghub.elsevier.com/retrieve/pii/S0301679X06000466⟩, ISSN 0301679X

Swalla, Dana R./Neu, Richard W./McDowell, David L.: Microstructural Characterization of Ti-6Al-4V Subjected to Fretting. Journal of Tribology, 126 2004, Nr. 4, 809 ⟨URL: http://tribology.asmedigitalcollection.asme.org/article.aspx?articleid=1467213⟩, ISSN 07424787

Tabor, D.: The hardness of solids. Review of Physics in Technology, 1 1970, Nr. 3, 145–179

Tabor, D.: Indentation hardness: Fifty years on a personal view. Philosophical Magazine A, 74 nov 1996, Nr. 5, 1207–1212 ⟨URL: http://www.tandfonline.com/doi/abs/10.1080/01418619608239720⟩, ISSN 0141–8610

Takahashi, Tetsuya/Ponge, Dirk/Raabe, Dierk: Investigation of orientation gradients in pearlite in hypoeutectoid steel by use of orientation imaging microscopy. Steel research international, 78 2007, Nr. 1, 38–44

Tallian, T.E.: The theory of partial elastohydrodynamic contacts. Wear, 21 aug 1972, Nr. 1, 49–101 ⟨URL: http://www.sciencedirect.com/science/article/pii/0043164872902499⟩, ISSN 00431648

Tarasov, S. Yu./Lychagin, D.V./Chumaevskii, A.V.: Orientation dependence of subsurface deformation in dry sliding wear of Cu single crystals. Applied Surface Science, 274 February 2013, 22–26 ⟨URL: http://linkinghub.elsevier.com/retrieve/pii/S0169433213003115⟩, ISSN 01694332

Terada, Kenjiro et al.: Numerical re-examination of the micro-scale mechanism of the Bauschinger effect in carbon steels. Computational Materials Science, 31 sep 2004, Nr. 1-2, 67–83 ⟨URL: http://www.sciencedirect.com/science/article/pii/S0927025604000539⟩, ISSN 09270256

Totten, G/Inoue, T/Howes, M: Handbook of Residual Stress and Deformation of Steel. ASM International, aug 2011, 192

Trausmuth, A et al.: Influence of Heat Treatment and Surface Condition on Early-Damaging of Rail Materials. Proceedings of the Second International Conference on Railway Technology: Research, Development and Maintenance 2014, Nr. 188

Trimby, Patrick W: Orientation mapping of nanostructured materials using transmission Kikuchi diffraction in the scanning electron microscope. Ultramicroscopy, 120 sep 2012, 16–24 ⟨URL: http://www.ncbi.nlm.nih.gov/pubmed/22796555⟩, ISSN 1879–2723

Trimby, Patrick W. et al.: Characterizing deformed ultrafine-grained and nanocrystalline materials using transmission Kikuchi diffraction in a scanning electron microscope. Acta Materialia, 62 jan 2014, 69–80 ⟨URL: http://linkinghub.elsevier.com/retrieve/pii/S1359645413007118⟩, ISSN 13596454

Tyfour, W R/Beynon, J H/Kapoor, A: The steady state wear behaviour of pearlitic rail steel under dry rolling-sliding contact conditions. Wear, 180 1995, 79–89

Vuorinen, Esa: Standing contact fatigue en litteraturstudie. Luleå Tekniska Universitet, Avdelningen för Materialteknik, 2008 – Technical report

Walzhofer, F et al.: Characterization of frictional stressed white wtching layers out of cutting tools by means of transmission electron microscopy (TEM). Practical Metallography, 43 2014, Nr. 7, 485–498

Wang, L et al.: Microstructure features on rolling surfaces of railway rails subjected to heavy loading. Materials Science and Engineering: A, 359 oct 2003, Nr. 1-2, 31–43

⟨URL: http://linkinghub.elsevier.com/retrieve/pii/S0921509303003277⟩, ISSN 09215093

Wang, Y.M. et al.: Microsample tensile testing of nanocrystalline copper. Scripta Materialia, 48 jun 2003, Nr. 12, 1581–1586 ⟨URL: http://linkinghub.elsevier.com/retrieve/pii/S1359646203001593⟩, ISSN 13596462

Wheeler, D.R./Buckley, D.H.: Texturing in metals as a result of sliding. Wear, 33 jun 1975, Nr. 1, 65–74 ⟨URL: http://dx.doi.org/10.1016/0043-1648(75)90224-0⟩, ISSN 00431648

Wiese, Steffen: Verformung und Schädigung von Werkstoffen der Aufbaun- und Verbindungstechnik. Springer Heidelberg, 2010

Wilkinson, A.J./Dingley, D.J.: Quantitative deformation studies using electron back scatter patterns. Acta Metallurgica et Materialia, 39 dec 1991, Nr. 12, 3047–3055 ⟨URL: http://dx.doi.org/10.1016/0956-7151(91)90037-2⟩, ISSN 09567151

Wilkinson, Angus J: A new method for determining small misorientations from electron back scatter diffraction patterns. Scripta Materialia, 44 may 2001, Nr. 10, 2379–2385 ⟨URL: http://linkinghub.elsevier.com/retrieve/pii/S1359646201009435⟩, ISSN 13596462

Williams, J. A./Dyson, I. N./Kapoor, A.: Repeated loading, residual stresses, shakedown, and tribology. Journal of Materials Research, 14 2005, Nr. 04, 1548–1559 ⟨URL: http://journals.cambridge.org/abstract_S0884291400049104http://journals.cambridge.org/action/displayAbstract;jsessionid=19EED2FB96491227D74E75A9E909B47A.journals?fromPage=online&aid=7989522http://journals.cambridge.org/production/action/cjoGetFulltext?f⟩, ISSN 2044–5326

Williams, John A: The influence of repeated loading, residual stresses and shakedown on the behaviour of tribological contacts. Tribology International, 38 2005, 786–797

Williams, John A: Wear and wear particles - some fundamentals. Tribology International, 38 2005, 863–870

Wilson, AW/Madison, JD/Spanos, G: Determining phase volume fraction in steels by electron backscattered diffraction. Scripta materialia, 45 2001, 1335–1340 ⟨URL: http://www.sciencedirect.com/science/article/pii/S135964620101137X⟩

Wright, S I/Adams, B L: Automated Lattice Orientation Determination from Electron Backscatter Kikuchi Diffraction Patterns. Textures and Microstructures, 14-18 1991, 273–278

Wright, Stuart I/Adams, Brent L: Automatic Analysis of Electron Backscatter Diffraction Patterns. Metallurgical Transactions A, 23 1992, Nr. March, 759–767

Wright, Stuart I./Nowell, Matthew M./Field, David P: A review of strain analysis using electron backscatter diffraction. Microscopy and Microanalysis, 17 2011, 316–329

Wrights, Stuart I/Zhao, Jun-wu/Adamsf, Brent L: Automated determination of lattice orientation from electron backscattered kikuchi diffraction patterns. Textures and Microstructures, 13 1991, 123–131

Xu, W. et al.: Techniques for generating 3-D EBSD microstructures by FIB tomography. Materials Characterization, 58 oct 2007, Nr. 10, 961–967 ⟨URL: `http://linkinghub.elsevier.com/retrieve/pii/S1044580306002786`⟩, ISSN 10445803

Yin, F/A, Fatemi: Monotonic and Cyclic Deformations of Case-Hardened Steels Including Residual Stress Effects. Strain 47 2011

Zaafarani, N. et al.: Three-dimensional investigation of the texture and microstructure below a nanoindent in a Cu single crystal using 3D EBSD and crystal plasticity finite element simulations. Acta Materialia, 54 apr 2006, Nr. 7, 1863–1876 ⟨URL: `http://linkinghub.elsevier.com/retrieve/pii/S1359645406000292`⟩, ISSN 13596454

Zaefferer, S/Romano, P/Friedel, F: EBSD as a tool to identify and quantify bainite and ferrite in low-alloyed Al-TRIP steels. Journal of microscopy, 230 jun 2008, Nr. Pt 3, 499–508 ⟨URL: `http://www.ncbi.nlm.nih.gov/pubmed/18503676`⟩, ISSN 1365–2818

Zerbst, Uwe/Mädler, Katrin/Hintze, Hartmut: Fracture mechanics in railway applications-an overview. Engineering Fracture Mechanics, 72 jan 2005, Nr. 2, 163–194 ⟨URL: `http://linkinghub.elsevier.com/retrieve/pii/S0013794404001262`⟩, ISSN 00137944

Zhengyi, Liu/Jian, Fu/Yuzhi, Zhuang: Friction martensite and its tempering characteristics. Acta Metallurgica Sinica, 3 1990, 35–39

Figure References

Figure 2.1:
Liu, S., & Wang, Q. (2002). Studying contact stress fields caused by surface tractions with a discrete convolution and fast Fourier transform algorithm. *Journal of tribology*, *124*(1), 36-45.

Figure 2.2:
Kalin, M., Velkavrh, I., & Vižintin, J. (2009). The Stribeck curve and lubrication design for non-fully wetted surfaces. *Wear*, *267*(5-8), 1232-1240.

Figure 2.3:
Hokkirigawa, K., & Kato, K. (1988). An experimental and theoretical investigation of ploughing, cutting and wedge formation during abrasive wear. *Tribology international*, *21*(1), 51-57.

Figure 2.4:
Bergmann, Wolfgang: Werkstofgtechnik 1. Volume 6, Carl Hanser Verlag München, 2008, 111–113

Figure 2.5:
Pan, N., & Sheppard, S. D. (2002). Stress intensity factors in spot welds. *Engineering Fracture Mechanics*, *70*(5), 671-684.

Figure 2.6:
Heilmann, P., Clark, W. A. T., & Rigney, D. A. (1982). Computerized method to determine crystal orientations from Kikuchi patterns. *Ultramicroscopy*, *9*(4), 365-371.

Figure 2.7:
Kamaya, M. (2009). Measurement of local plastic strain distribution of stainless steel by electron backscatter diffraction. *Materials Characterization*, *60*(2), 125-132.

Figure 2.8:
Brewer, Luke N/Field, David P/Merriman, Colin C: Mapping and assessing plastic deformation using EBSD. In Schwartz, Adam J. etal., editors: Electron Backscatter Difgraction in Materials Science. 2nd edition. New York: Springer, 2009, ISBN 0387881352.– chapter 18, 251–262

Figure 3.3, 3.8, 4.29, 4.30, 4.31, 4.32, 4.33, 4.34, 4.35, 4.36:
Linz, M., Winkelmann, H., Hradil, K., Badisch, E., & Mücklich, F. (2013). Directional development of residual stress and surface fatigue during sliding contact. Engineering Failure Analysis, 35, 678-685.

Figure 3.2, 4.37, 4.38, 4.39, 4.40, 4.41, 4.42, 4.43, 4.44, 5.3:
Linz, M., Cihak-Bayr, U., Trausmuth, A., Scheriau, S., Künstner, D., & Badisch, E. (2015). EBSD study of early-damaging phenomena in wheel–rail model test. Wear, 342, 13-21.

Figure 3.4, 4.16, 4.17, 4.18, 4.19, 4.20, 4.21, 4.22, 4.23, 4.24, 4.25, 4.26, 4.27, 4.28, 5.2:
Linz, M., Ripoll, M. R., Gachot, C., Pauly, C., Franek, F., & Mücklich, F. (2017). On the competition between plastic deformation and material detachment in ferritic/pearlitic steel under boundary lubrication. Wear, 376, 813-821.

Figure 3.1, 3.6, 3.7, 4.2, 4.3, 4.4, 4.5, 4.6, 4.7, 4.8, 4.9, 4.10, 4.11, 4.12, 4.13, 4.14, 4.15, 5.1:
Linz, M., Rodríguez Ripoll, M., Pauly, C., Bernardi, J., Steiger Thirsfeld, A., Franek, F., ... - & Gachot, C. (2018). Heterogeneous Strain Distribution and Saturation of Geometrically Necessary Dislocations in a Ferritic–Pearlitic Steel during Lubricated Sliding. Advanced Engineering Materials.